LBNL-42621

ERNEST ORLANDO LAWRENCE BERKELEY NATIONAL LABORATORY

Exciton-Exciton Correlations in Semiconductors in High Magnetic Fields

Peter A. Kner

Materials Sciences Division

December 1998

Ph.D. Thesis

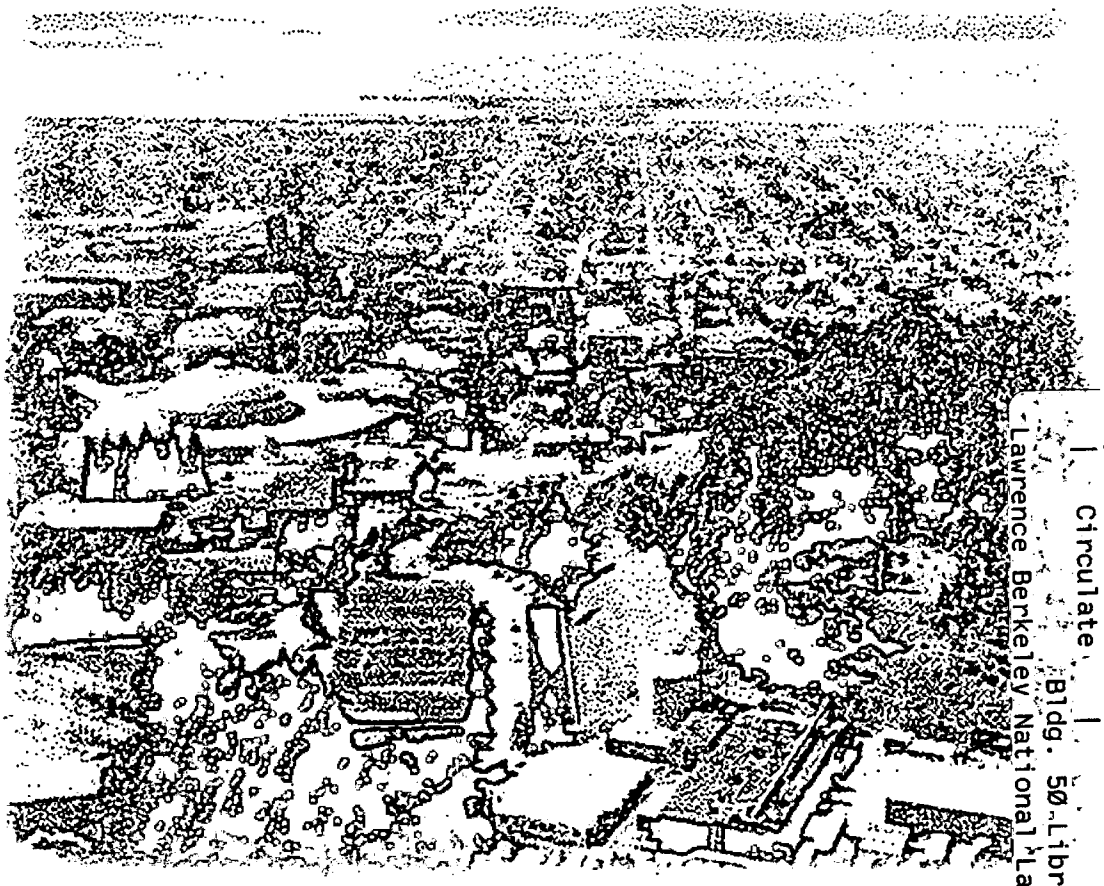

REFERENCE COPY
Does Not
Circulate
Bldg. 50 Library - Ref.
Lawrence Berkeley National Laboratory
Copy 1
LBNL-42621

DISCLAIMER

This document was prepared as an account of work sponsored by the United States Government. While this document is believed to contain correct information, neither the United States Government nor any agency thereof, nor the Regents of the University of California, nor any of their employees, makes any warranty, express or implied, or assumes any legal responsibility for the accuracy, completeness, or usefulness of any information, apparatus, product, or process disclosed, or represents that its use would not infringe privately owned rights. Reference herein to any specific commercial product, process, or service by its trade name, trademark, manufacturer, or otherwise, does not necessarily constitute or imply its endorsement, recommendation, or favoring by the United States Government or any agency thereof, or the Regents of the University of California. The views and opinions of authors expressed herein do not necessarily state or reflect those of the United States Government or any agency thereof or the Regents of the University of California.

LBNL-42621

Exciton-Exciton Correlations in Semiconductors in High Magnetic Fields

Peter Alexander Kner

Department of Physics
University of California, Berkeley

and

Materials Sciences Division
Ernest Orlando Lawrence Berkeley National Laboratory
University of California
Berkeley, California 94720

December 1998

This work was supported by the Director, Office of Energy Research, Office of Basic Energy Sciences, Materials Sciences Division, of the U.S. Department of Energy under Contract No. DE-AC03-76SF00098.

Exciton-Exciton Correlations in Semiconductors in High Magnetic Fields

by

Peter Alexander Kner

B.S. (Massachusetts Institute of Technology) 1991
B.S. (Massachusetts Institute of Technology) 1991
M.A. (University of California at Berkeley) 1995

A dissertation submitted in partial satisfaction of the
requirements for the degree of
Doctor of Philosophy

in

Physics

in the

GRADUATE DIVISION
of the
UNIVERSITY of CALIFORNIA at BERKELEY

Committee in charge:

Daniel S. Chemla, Chair
Joseph W. Orenstein
Constance J. Chang-Hasnain

Fall 1998

Exciton-Exciton Correlations in Semiconductors in High Magnetic Fields

Copyright © 1998

by

Peter Alexander Kner

The U.S. Department of Energy has the right to use this document
for any purpose whatsoever including the right to reproduce
all or any part thereof.

Abstract

Exciton-Exciton Correlations in Semiconductors in High Magnetic Fields

by

Peter Alexander Kner

Doctor of Philosophy in Physics

University of California at Berkeley

Daniel S. Chemla, Chair

Mean-field, Hartree-Fock theory has been successful in explaining many nonlinear optical experiments in semiconductors. But recently experiments have shown important cases where the mean-field theory (the Semiconductor Bloch Equations) fails. One such case is bulk GaAs in a strong magnetic field. Here, the exciton-exciton interaction can be tuned by varying the magnetic field, providing an excellent method for studying the transition from a regime where mean-field theory is valid to a regime where exciton-exciton correlations must be taken into account.

We perform ultrafast time-resolved four-wave mixing on bulk GaAs in a magnetic field and compare our experimental results with theoretical calculations which go beyond Hartree-Fock theory. We find excellent qualitative agreement. Furthermore, because of the strong correlations that are present, GaAs in a magnetic field presents an excellent opportunity to study the exciton-exciton correlations themselves. We find, surprisingly, that the exciton-exciton correlations persist at densities where the excitons are $\sim$ 10 Bohr radii

apart. As the density is increased, we see the transition to a regime where the mean-field theory is valid at high densities. We also investigate the coherence of the exciton-exciton correlations as the temperature and free carrier density are varied and find a surprising sensitivity of the exciton-exciton correlation coherence to these parameters.

To my family

Contents

List of Figures vi

List of Tables viii

1 Introduction 1
- 1.1 Overview . . . 1
- 1.2 Motivation for this work . . . 3
- 1.3 Previous work on semiconductors in magnetic fields . . . 4
- 1.4 Outline of this work . . . 5

2 Theoretical Background 7
- 2.1 Introduction . . . 7
- 2.2 GaAs band structure . . . 7
- 2.3 The magnetic field . . . 9
- 2.4 Four-wave mixing . . . 11
- 2.5 Maxwell-Liouville equations . . . 13
- 2.6 Multilevel systems . . . 14
- 2.7 The Semiconductor Bloch Equations . . . 19
- 2.8 Failures of the SBE . . . 25
- 2.9 SBE calculation of GaAs in a magnetic field . . . 27
- 2.10 Conclusion . . . 28

3 Experimental Setup 29
- 3.1 Introduction . . . 29
- 3.2 The laser system . . . 30
- 3.3 Optical setup . . . 33
- 3.4 Four-wave mixing detection and measurement . . . 34
- 3.5 Finding the signal . . . 36
- 3.6 The magnet . . . 37
- 3.7 Samples . . . 40
- 3.8 Linear absorption measurements . . . 41
- 3.9 Spot size measurements . . . 42
- 3.10 Density calculations . . . 43

3.11 Data collection software 45

4 Linear Measurements **47**
4.1 Introduction 47
4.2 Absorption spectra 47
4.3 Time-domain measurements 52
4.4 Conclusion 52

5 Experimental Results **55**
5.1 Introduction 55
5.2 Time-integrated four-wave mixing 56
5.3 Four-wave mixing power spectra 61
5.4 Time-resolved four-wave mixing 63
5.5 Conclusion 66

6 Theory **69**
6.1 Introduction 69
6.2 The Dynamics Controlled Truncation Scheme 70
6.3 The $\chi^{(3)}$ Truncation Scheme 73
6.4 Results for GaAs in a magnetic field 74
6.5 The average polarization model 79
6.6 Effect of the magnetic field 83
6.7 Propagation/Polariton effects 84
6.8 Conclusion 84
6.9 Appendix 85

7 Properties of 4-particle Correlations **87**
7.1 Introduction 87
7.2 Density dependence 88
7.3 Coherence 91
7.4 Conclusion 99

8 Further Experiments **100**
8.1 Introduction 100
8.2 High intensity experiments 101
8.3 Long pulse measurements 103
8.4 FWM measurements on the 1 micron sample 109
8.5 Conclusion 114

9 Conclusion **115**

Bibliography **119**

A A new formulation of the theory **129**
A.1 Matrix elements 136

List of Figures

2.1 Band Structure of GaAs 8
2.2 Allowed interband transitions, exciting with σ^- light. 10
2.3 FWM Configuration 12
2.4 Results for a two-level system with $\Delta = 1.5$eV and $T_2 = 3$ps. 16
2.5 Multilevel Systems 17
2.6 TI-FWM for a four-level and three-level system 18
2.7 PB and BCI nonlinearities 24
2.8 SBE Calculation of TI-FWM for bulk GaAs in a magnetic field 26

3.1 The FWM Configuration. 30
3.2 typical laser spectrum and autocorrelation 31
3.3 Results of a FROG measurement on the laser. 32
3.4 Layout of the Optical Table 33
3.5 Magnet cross-section 38
3.6 Sample structure. 40

4.1 Light bulb absorption spectra 48
4.2 Parameters of the lh-X and hh-X 49
4.3 Laser absorption spectra 50
4.4 Parameters of the lh-X and hh-X 51
4.5 Time-resolved transmission 53

5.1 Laser and absorption spectra at 0 Tesla. 56
5.2 TI-FWM vs. B for the Sandia sample. 57
5.3 Rise and decay times of the TI-FWM shown in Fig. 5.2. 58
5.4 TI-FWM vs. B for the Bell Labs sample. $N \approx 10^{16}\text{cm}^{-3}$. 59
5.5 Rise and decay times for the TI-FWM of Fig. 5.4 60
5.6 Exciton and free carrier density vs. B for the Sandia sample. 61
5.7 FWM-PS at $\Delta t = 0$ vs. B. 62
5.8 FWM-PS vs. Δt 64
5.9 FWM-PS at different delays. 65
5.10 TR-FWM for a few Δt. 67
5.11 Time of maximum of TR-FWM vs. Δt. 68

5.12 Contour plot of TR-FWM. 68

6.1 TI-FWM in a magnetic field calculated from the $\chi^{(3)}$ truncation scheme. . . 76
6.2 hh-X (solid) and lh-X (dashed) contributions to the FWM. 77
6.3 TR-FWM and FWM-PS calculated from the $\chi^{(3)}$ truncation scheme. 78
6.4 TI-FWM calculated for a few different magnetic field strengths from the $\chi^{(3)}$ truncation scheme. 79
6.5 TI-FWM calculated from eqns. 6.22 and 6.23. 81
6.6 TI-FWM and TR-FWM calculated from eqns. 6.24 - 6.28. 82

7.1 TI-FWM vs. Density at B=10T 89
7.2 τ_r and τ_d vs. density. $N0 = 10^{17}\text{cm}^{-3}$. 90
7.3 Peak FWM Intensity vs. carrier density 91
7.4 TI-FWM on the Sandia sample for different temperatures. 92
7.5 TI-FWM on the Bell Labs sample for different temperatures. 93
7.6 τ_r and τ_d vs. temperature 94
7.7 $\chi^{(3)}$ Truncation Scheme calculation with $\gamma_B = 2\gamma_P$. 95
7.8 TI-FWM for different detunings 97
7.9 τ_r and τ_d vs. free carrier density 98

8.1 TI-FWM vs. B at high intensity. 102
8.2 τ_d vs. B at high intensity. 103
8.3 Normalized FWM-PS vs. B at $N \approx 3 \times 10^{17}\text{cm}^{-3}$. 104
8.4 TI-FWM at B=0T for different detunings for excitation with $\sim$ 600fs pulses. 105
8.5 TI-FWM at B=10T for different detunings. 107
8.6 FWM-PS at B=10T. 108
8.7 TI-FWM vs. B on the 1 micron sample. $I_{k_2} \approx 4I_{k_1}$. 110
8.8 TI-FWM vs. density at B=6T on the 1 micron sample. $I_{k_2} \approx 4I_{k_1}$. 111
8.9 FWM-PS at $\Delta t = 0$ for different thickness samples. 112
8.10 FWM-PS vs. Δt for the 1 micron sample at B=10T. 113

A.1 TI-FWM calculated taking the $q_{||}$ into account 136

List of Tables

2.1 Important parameters for GaAs. 27

8.1 e-h pair densities and τ_r and τ_d for the curves in Fig. 8.4. Ec is the center frequency of the laser, and fc stands for free carriers. 106

8.2 e-h pair densities and τ_r and τ_d for the curves in Figs. 8.5 and 8.6. 106

Acknowledgements

First and foremost, my thanks go to the people who taught me how to do scientific research, my advisor, Daniel Chemla, and Shimshon Barad. In addition to teaching me about the physics of semiconductors, Daniel has shown me, by example, the creativity and imagination that are necessary to be a physicist. Shimshon taught me everything I know about performing a four-wave mixing experiment and being a careful experimentalist and was a great companion for afternoon coffee.

In addition to Shimshon, I have had the benefit of working with many other intelligent and hard-working people in the magnet lab. In particular, Maria Valéria Marquezini helped me take most of the data in Chapter 5 and was always a cheerful presence in lab. I am happy that Neil Fromer decided to do his thesis in the magnet lab, and I hope that he managed to learn something from working with me. I am also indebted to Wilfried Schäfer who provided the elegant theory to explain our surprising results.

Jen Glass and the other members of the Chemla group have been good resources and good companions. In particular, lunch would not have been as enjoyable without Jen, Gino Segrè, Rich Mallozzi, Dave Klein, Andreas Schumacher, John Corson, and all the others who contributed to the free-ranging conversation. I am also happy to have had good friends outside of work during my time at Berkeley. In particular I enjoyed having fun and discussing physics with Glenn Cooper, Alan Chin and Jim Morehead. It is also nice to have friends outside of physics, and I was lucky to have so many friends from TEP in the area. Jocelyn has made the last months of graduate school much more enjoyable for which I am very grateful. Lastly, I would like to thank my family for all their support and for having shown me such a healthy perspective on work and life.

Chapter 1

Introduction

1.1 Overview

An optically excited semiconductor provides a perfect laboratory for studying many important questions in many-body physics. A laser can create electron-hole pairs at an arbitrary density and the dynamics of these pairs can be studied on ultra-short time scales. (Lasers can currently provide a time resolution of $\sim$ 10fs.) Many interesting problems in many-body physics have been studied optically in semiconductors including electron-hole liquids [33], the Mott transition [22], carrier relaxation [10, 39], and the AC Stark effect [65, 66]. Currently there is interest in experiments that explore the whole range of electron-hole pair densities from those using very high intensity ultrafast lasers that excite a density of electron-hole pairs $\sim 10^{22}\text{cm}^{-3}$, capable of melting the semiconductor, to experiments in which only $\sim 10^{13}\text{cm}^{-3}$ electron-hole pairs are excited, designed to explore the extent of exciton-exciton interactions.

Fairly simple treatments of the many-body effects have successfully explained some

important experiments in semiconductors. For example, the biexciton resonance, which is a bound state of two electrons and two holes, has been explained using a simple multilevel system model in which the biexciton is represented by an energy level at twice the exciton energy less the biexciton binding energy. Experiments which have explored the coherence properties of the excitons in semiconductors have used the optical Bloch equations, which describe the optical response of a two-level system, to analyze the results.

A more sophisticated treatment which includes the Coulomb interaction between the electrons and holes in the semiconductor is provided by the Semiconductor Bloch Equations (SBE) which treat the Coulomb interaction in the time-dependent Hartree-Fock approximation. This results in a mean-field theory for the e-h pairs [65, 49, 26]. The SBE have successfully explained many experiments and effects including the AC Stark effect. But, because of the mean-field approximation, the SBE are unable to explain effects which involve correlations beyond the electron-hole correlation that leads to the exciton. The most obvious example of this is the bound and unbound biexciton states which are not included in the SBE.

Recent experiments have shown other discrepancies with SBE calculations [14, 34, 79]. Green's function techniques [15], density matrix formalisms [78], exact calculations for a few excitons [52] and phenomenological terms have all been used to extend the theoretical description. Depending on the approximations inherent in the different approaches, each theory has some weaknesses and a limited regime of validity. Because it will always be necessary to make approximations in many-body physics, the interplay between experiment and theory in semiconductor optics provides an excellent opportunity to test the various approximations necessary in the theory and to explore the many-body effects found in

semiconductors.

1.2 Motivation for this work

In this work, we describe four-wave mixing experiments (FWM) done on the lowest lying excitons in bulk GaAs in a magnetic field. The motivation for this work is to understand how the magnetic field affects the dephasing and interactions of these excitons. Much work has been done on the effects of two-dimensional confinement due to heterostructures on the dephasing and interactions of excitons, and quantum wells in a magnetic field had been studied previously, but no ultrafast spectroscopy had yet been performed on the lowest lying excitons in bulk GaAs in a magnetic field. This work was originally intended to complement work done on the Fano resonances of higher lying magneto-exciton states [72], but has revealed interaction effects not seen in the higher magneto-excitons. We originally expected that the magnetic field would affect the exciton dephasing time because of the confinement of the exciton wavefunction by the magnetic field. But instead the magnetic field resulted in very strong correlated interactions between the excitons without significantly affecting the exciton dephasing.

Studying these interactions became the central focus of the work. We have shown that these interactions cannot be explained within the mean-field formalism of the Semiconductor Bloch Equations. Moreover, we have explored the coherence, strength, range, and other properties of these interactions.

1.3 Previous work on semiconductors in magnetic fields

Semiconductors in magnetic fields have been studied since 1960 when Elliott calculated the linear absorption spectrum for a semiconductor in a magnetic field at the band edge [21], and Hopfield measured the linear spectra of semiconductors in magnetic fields [28]. But significant advances have been made since then both in experimental techniques and in material quality. For example, only recently were the Fano resonances due to higher-lying magneto-exciton states seen, primarily because of improvements in crystal quality [25, 11]. The discovery was made in a high quality MBE grown layer of GaAs. In addition, mode-locked lasers with pulse durations short enough to resolve the electron dynamics in semiconductors have only become available in the last 15 years.

The dynamics of excitons in magnetic fields have been studied previously [17, 19, 32, 59, 73, 74], but this is the first study in which strong 4-particle correlations have been detected. In studies of the dynamics of the higher lying magneto-excitons, the Fano resonances, effects were seen which lead to a faster decay for the time-integrated four-wave mixing (FWM) than for the time-resolved FWM [72, 71]. This effect was named quantum destructive interference but was not explained on the basis of microscopic theory. It is clearly a many-body effect because calculations of the FWM from a simple model of a Fano resonance do not lead to quantum destructive interference [55].

Two of the previous studies dealt with strongly inhomogeneously broadened systems in which interaction effects are washed out [17, 59]. Inhomogeneous broadening tends to destroy or mask many of the effects of interactions on the FWM signal [31]. Thus, the FWM signal for negative time delay is not seen in inhomogeneously broadened systems. In ref. [59], the material studied was InGaAs which is a ternary alloy and, as such, is inherently

inhomogeneously broadened.

In GaAs quantum wells the strong correlation effects we discuss are not seen. A reduction in exciton interactions has been seen for the lowest lying exciton states in pump-probe measurements [74]. In these measurements, the strength of the exciton-exciton interactions was determined from the shift in the energy of the exciton resonance, and the interaction was modelled as a repulsive hard-core interaction between the excitons. Interactions between the lowest excitons and higher energy excitons have been measured by a novel four-wave mixing measurement and explained using a multilevel system model [19]. The nonlinear optical response has been calculated within a Hartree-Fock theory [73].

Jiang *et. al.* [32] performed a four-wave mixing measurement in the frequency domain on bulk GaAs and saw an increase in the nonlinear signal with increasing magnetic field which they attributed to reduced exciton diffusion. Photoluminescence measurements done on high-quality GaAs [60] found an increase in the exciton luminescence with magnetic field which was attributed to a lower exciton temperature in the magnetic field. The more effective exciton cooling in a magnetic field is ascribed to an increased energy relaxation rate.

1.4 Outline of this work

In the next chapter, we give the theoretical fundamentals necessary for interpreting the experiments: the GaAs band structure, effect of the magnetic field, and the basic theory of four-wave mixing experiments. Then, in chapter 3, we describe the experimental apparatus in detail. In chapter 4, linear spectroscopy on GaAs in a magnetic field is discussed as preparation for considering the nonlinear experiments. The main experimental

results are given in chapter 5 and the theoretical interpretation is presented in chapter 6. Chapter 7 discusses experiments that explore the interactions in more detail and chapter 8 reviews some additional experiments concerning further aspects of the behavior of excitons in a magnetic field. In Chapter 9 we summarize our results and discuss some of the questions raised by our research.

Chapter 2

Theoretical Background

2.1 Introduction

In this chapter, we review the band structure and optical selection rules of GaAs and discuss the effect of the magnetic field on the semiconductor. We then discuss the theoretical interpretation of four-wave mixing experiments using some of the accepted theories previous to the time of this research. These results set the background for interpreting our experiments.

2.2 GaAs band structure

The band structure of bulk GaAs near the band-edge is shown in figure 2.1. The band-edge is located at the Γ-point in the middle of the Brillouin zone. There are two S-like conduction bands and 6 P-like valence bands. If we ignore the slight warping of the bands due to the cubic symmetry of the crystal, the angular momentum is a good quantum number, and we can label the bands by their total angular momentum, **J**. The lowest lying

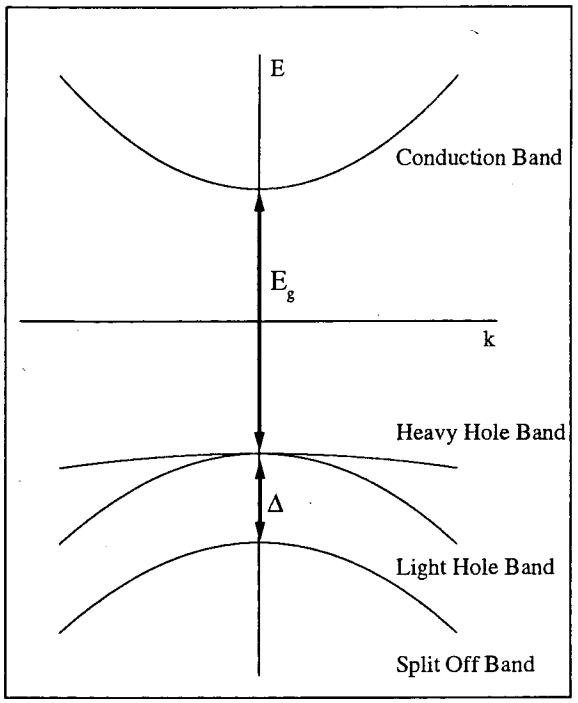

Figure 2.1: Band structure of GaAs. $E_g = 1.5192$eV and $\Delta = 0.341$eV at low temperature [13].

valence bands have $J = 1/2$ and are known as the split-off bands because they are lower in energy than the other two bands due to spin-orbit coupling. The bands with $J = 3/2$ and $m_J = \pm 3/2$ are the heavy-hole (hh) bands with effective mass $m_{hh} = 0.5m_0$ where m_0 is the bare electron mass. The bands with $m_J = \pm 1/2$ are the light-hole (lh) bands with $m_{lh} = 0.082m_0$. The conduction bands have $m_s = \pm 1/2$ and $m_e = 0.0665m_0$. Due to the symmetry of the bands, the transitions from the upper valence bands to the conduction bands are dipole allowed, and only the $l = 0$ exciton states can be excited. Table 2.1 at the end of the chapter lists some important parameters for bulk GaAs.

At low temperature, there is a mechanical strain in our sample induced by the sapphire window (The sample preparation is discussed in the next chapter.) which lifts the degeneracy of the lh and hh bands at $k = 0$, resulting in two distinct exciton species, the lh-X

and the hh-X [58]. In our experiments, we excite with σ^- polarized light so that only certain transitions are allowed, as shown in Fig. 2.2. In this polarization configuration, within the mean-field theory, the SBE, there is no interaction between the lh-X and hh-X. There is no interaction due to Fermi-statistics because the lh-X and hh-X do not share a common band, and there is no Coulomb interaction because the matrix element of the Coulomb interaction is zero between the lh-X and hh-X [61]. Furthermore no bound hh-X/hh-X or lh-X/lh-X biexcitons can be formed because all the hh-X/hh-X and lh-X/lh-X interactions are in the triplet state — the electrons have the same spin. The oscillator strength of the lh-X/hh-X bound biexciton is very weak. Thus, the effect of bound biexcitons is minimized in this polarization configuration.

The strain in the sample results in a mixing of the states of the lh-band and the states of the hh-band. The mixing of the lh and hh bands occurs at $k \sim 0.07\text{nm}^{-1}$ which we estimate from the difference in energy between the lh-X and hh-X resonances. The wavefunction of the exciton in k-space is $\frac{\sqrt{8a_0^3}}{\pi(1+(a_0k)^2)^2}$. Thus, the points in k-space above 0.07nm^{-1} only contribute 29% to the exciton wavefunction. For simplicity, we do not include band-mixing effects in the theoretical treatment.

2.3 The magnetic field

The magnetic field shifts the transition energies of the excitons due to the exciton diamagnetism and the Zeeman splitting [25], but, more importantly, the magnetic field affects the dynamics of the electrons and holes and the structure of the exciton.

The electrons and holes are confined to Landau levels in the plane perpendicular to the field so that applying a strong magnetic field to a bulk sample of GaAs results in a

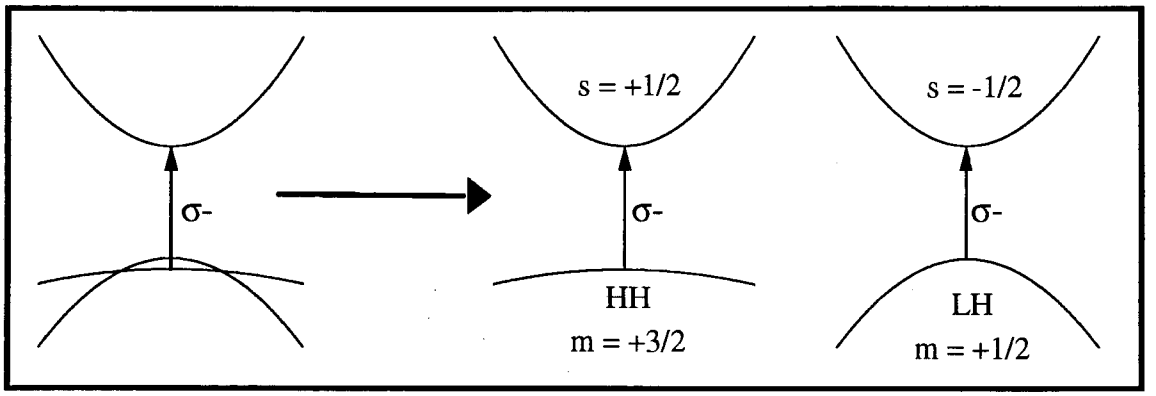

Figure 2.2: Allowed interband transitions, exciting with σ^- light.

transition from 3-dimensional motion of free electrons and holes to 1-dimensional motion. The confinement of the motion of the electron and hole results in a stronger Coulomb interaction between them. Thus the lowest lying excitons (those associated with the n=0 Landau level) are squeezed by the magnetic field. For large magnetic fields, the Bohr radius contracts $\propto \sqrt{|B|}$ in the plane perpendicular to B and $\propto \ln(|B|)$ in the direction parallel to B [42]. An important consequence of this elongation is that the exciton develops, at distances $\gg a_0$, a quadrupole moment as the magnetic field is increased, raising the possibility that, at low densities, the excitons might interact via a quadrupole-quadrupole interaction in high magnetic fields [44].

The exciton wavefunction only becomes significantly cigar-like for magnetic fields $B \gg B_c$ where B_c is the field strength at which the cyclotron radius equals the zero field Bohr radius, $\lambda_c = a_0$ [21].

$$B_c \equiv \frac{\mu^{*2} e^3 c}{\hbar^3 \epsilon^2} \tag{2.1}$$

where μ^* is the effective reduced mass of the exciton and ϵ is the background dielectric constant of GaAs. In GaAs, $B_c \approx 3.5T$ for the hh-X. We study the regime from B=0

to B=10 Tesla. At 10 Tesla, $\hbar\omega_c = 17.5$meV so the energy needed to make a transition between Landau levels is quite large for resonant excitation of the excitons with a $\sim$ 100fs Gaussian pulse (full width at half of the maximum of 18meV). For $B \ll B_c$ the magnetic field is a perturbation on the excitonic structure. For $B \gg B_c$, which is inaccessible in our experiment, the Coulomb interaction is a perturbation on the Landau levels. For $B \sim B_c$, the excitonic structure cannot be calculated analytically, but recently, the spectrum of the hydrogen atom in an arbitrary magnetic field has been calculated numerically [44]. We study the regime $B \sim B_c$ which is interesting both because of the computational difficulty in calculating the excitonic structure in this regime and because of the changes that occur to the biexcitonic ground state in this regime [43]. The hydrogen molecule has also been studied theoretically in arbitrary magnetic fields for the case of the magnetic field parallel to the molecular axis [43]. In this case it was found that the ground state of the molecule undergoes a transition at $B \approx 0.18B_c$ from the bound singlet state to the unbound triplet state. At $B \approx 14B_c$, beyond the range of our experiments, the ground state becomes the state $^3\Pi_u$.

2.4 Four-wave mixing

In a two-pulse degenerate four-wave mixing (FWM) experiment, two pulses from a modelocked laser at the same frequency, ω, with wavevectors $\vec{k}_1$ (pulse 1) and $\vec{k}_2$ (pulse 2) are focused on the sample separated by a time delay, Δt. The four-wave mixing signal emitted in the $2\vec{k}_2 - \vec{k}_1$ direction is then measured. By convention, Δt is positive when pulse 1 arrives at the sample first. A FWM signal is also emitted in the $2\vec{k}_1 - \vec{k}_2$ direction for which the roles of the two pulses are reversed. Figure 2.3 shows the basic setup.

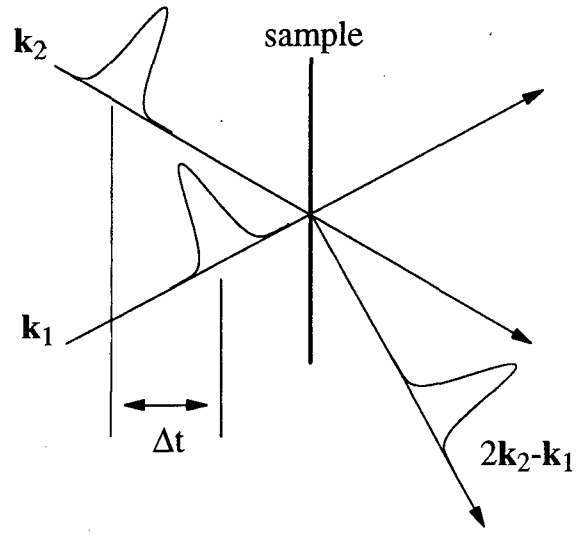

Figure 2.3: FWM Configuration

There are three basic measurements that can be made on the FWM signal. The intensity of the FWM signal can be measured in the time domain or frequency domain or the total energy can be measured. The frequency domain measurement, the FWM Power Spectrum (FWM-PS), is made by aligning the FWM signal into a spectrometer. The time-domain measurement, Time-Resolved FWM (TR-FWM), is made by doing a cross-correlation measurement of the FWM signal with a short reference pulse. The simplest measurement is time-integrated FWM (TI-FWM) in which the energy of the FWM signal is measured as a function of the time-delay, Δt. The setup for making these measurements will be discussed in the next chapter. Recently, techniques have been developed to fully characterize a weak signal such as a FWM signal, in both amplitude and phase, [23, 46], but these will not be discussed in this work.

2.5 Maxwell-Liouville equations

What we measure is the electric field of the light emitted in the direction $2\vec{k}_2 - \vec{k}_1$. To calculate this electric field, the coupled equations governing the light, described by Maxwell's equations, and the behavior of the sample, described by the Hamiltonian, need to be calculated. For many experiments, the light field can be treated classically. This is allowed because of the large number of photons interacting with the sample. Photoluminescence experiments are an exception because they involve the spontaneous emission of light which cannot be described semiclassically.

The equation for the light field is the wave equation for the electric field driven by the polarization created in the sample.

$$\nabla \times \nabla \times \vec{E}(r,t) + \frac{1}{c^2}\frac{\partial}{\partial t^2}\vec{E}(r,t) = -\frac{4\pi}{c^2}\frac{\partial}{\partial t^2}\vec{P}(r,t) \tag{2.2}$$

The polarization is then calculated quantum-mechanically. There are many different methods for calculating the polarization depending on the problem to be solved. One common formalism for calculating the polarization is with the density matrix, $\rho(t)$, [56].

$$\vec{P}(r,t) = Tr[\hat{P}(r,t)\rho(t)] \tag{2.3}$$

$$\frac{\partial}{\partial t}\rho(t) = -\frac{i}{\hbar}[\hat{H}(\vec{E}(r,t)),\rho(t)] \tag{2.4}$$

In general, these equations need to be solved self-consistently for $\vec{E}(r,t)$ and $\vec{P}(r,t)$ throughout the volume of the sample. We will make the simplifying assumption that the sample is optically thin. This allows us to ignore the spatial dependence of the polarization and the propagation of the fields through the sample. We calculate $\vec{P}(t)$ from the input fields to the sample and then calculate the emitted field from $\vec{P}(t)$. Thus, we can ignore

the propagation of fields and the problem reduces to solving equations 2.3 and 2.4 for the polarization.

2.6 Multilevel systems

It is helpful to consider the results of FWM experiments on some simple systems before considering the problem of a semiconductor which is a complicated many-body problem. The canonical system for thinking about the results of FWM experiments is an ensemble of non-interacting two-level systems. The Hamiltonian for this system is

$$\hat{H} = E_g|g\rangle\langle g| + E_e|e\rangle\langle e| - \vec{E}\cdot(\vec{\mu}|e\rangle\langle g| + \vec{\mu}^*|g\rangle\langle e|) \tag{2.5}$$

where $|g\rangle$ is the ground state and $|e\rangle$ is the excited state. The dipole moment is given by $\vec{\mu} = \langle e|e\vec{r}|g\rangle$, and $\vec{E}$ is the real electric field. The quantity we measure experimentally is the polarization, $P = \mu|e\rangle\langle g| + c.c.$

To calculate the optical response when the frequency of the light is close to resonance with the transition energy, the rotating wave approximation (RWA) can be made [1]. In the RWA, terms in the equations which oscillate at frequencies $\sim \Delta + \omega$ are ignored in favor of terms that oscillate at $\sim \Delta - \omega$ where $\Delta \equiv (E_e - E_g)$.

The density matrix formalism is used to account for relaxation effects, which are not included in the Hamiltonian, eqn. 2.5. The Liouville equation is written down for the individual components of the density matrix, ρ, and relaxation terms are added by hand. This leads to the well-known optical Bloch equations [1].

$$i\hbar\frac{\partial}{\partial t}\rho_{ee} = iIm[\mu^* E^* \rho_{eg}] - \frac{i\hbar}{T_1}\rho_{ee} \tag{2.6}$$

$$i\hbar\frac{\partial}{\partial t}\rho_{gg} = -iIm[\mu^* E^* \rho_{eg}] - \frac{i\hbar}{T_1}(\rho_{gg} - 1) \tag{2.7}$$

$$i\hbar\frac{\partial}{\partial t}\rho_{eg} = \Delta\rho_{eg} - \frac{1}{2}\mu E(\rho_{gg} - \rho_{ee}) - \frac{i\hbar}{T_2}\rho_{eg} \tag{2.8}$$

Here E is the complex electric field $E = \mathcal{E}e^{-i\omega t}$. T_1 is the longitudinal (population) relaxation time and T_2 is the transverse relaxation time or dephasing time. T_2 can also be expressed in terms of the dephasing rate, $\gamma = 1/T_2$.

These equations can be solved iteratively in powers of the electric field, starting with the 0th order solution which is just the density matrix for the system in its ground state when no electric field is applied.

$$\rho^{(0)} = \begin{pmatrix} \rho_{ee}^{(0)} & \rho_{eg}^{(0)} \\ \rho_{ge}^{(0)} & \rho_{gg}^{(0)} \end{pmatrix} = \begin{pmatrix} 0 & 0 \\ 0 & 1 \end{pmatrix} \tag{2.9}$$

The linear absorption can be calculated from the first order response to a monochromatic electric field. The susceptibility is then

$$\chi(\omega) = \frac{-\frac{1}{2}|\mu|^2}{(\hbar\omega - \Delta) + i\hbar/T_2} \tag{2.10}$$

and the absorption coefficient is

$$\alpha = \frac{\omega}{c\epsilon} Im[\chi(\omega)] \tag{2.11}$$

As already mentioned, the FWM signal is calculated by considering the polarization created with wavevector $2\vec{k}_2 - \vec{k}_1$ by a sequence of two pulses with wavevectors $\vec{k}_1$ and $\vec{k}_2$ separated by time delay, Δt. The third order response $\propto E_2^2 E_1^*$ is the desired FWM signal. The calculation begins from the ground state of the system.

The electric fields are assumed to be of the form $E = \mathcal{E}(t)e^{i(\vec{k}\cdot\vec{r}-\omega t)}$ where $\mathcal{E}(t)$ describes the pulse shape and is slowly varying with respect to the optical period. For the case of "delta-function" excitation where $\mathcal{E}_1(t) = E_1\delta(t)$ and $\mathcal{E}_2(t) = E_2\delta(t - \Delta t)$, the FWM response can be solved analytically to 3rd order in the electric field. The polarization in the

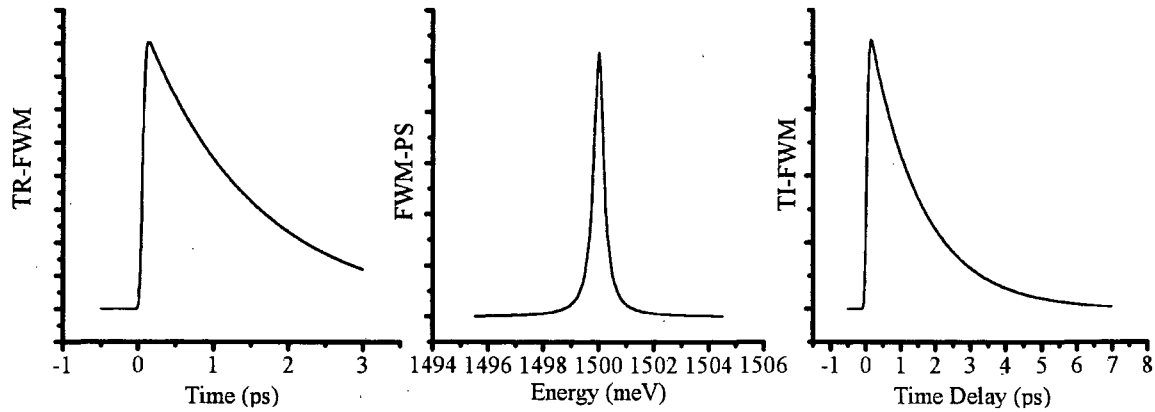

Figure 2.4: Results for a two-level system with $\Delta = 1.5$eV and $T_2 = 3$ps.

$2\vec{k}_2 - \vec{k}_1$ direction is

$$P(t) = \frac{-i}{4\hbar^3}|\mu|^4 E_2^2 E_1^* \Theta(\Delta t) e^{2i(\Delta-\omega)\Delta t}\Theta(t-\Delta t)e^{(-i\Delta-\gamma)t} \tag{2.12}$$

(Here Δ represents the frequency, not the energy.) It can be seen that a signal is emitted after the second pulse and only if pulse E_1 arrives first — i.e. $\Delta t > 0$. The TR-FWM is given by $|P(t)|^2$ and the FWM-PS is given by $|P(\omega)|^2$ where $P(\omega)$ is the Fourier transform of $P(t)$. The TI-FWM signal is

$$S_{TI}(\Delta t) = \int_{-\infty}^{+\infty} |P(t;\Delta t)|^2 dt = \frac{1}{16\hbar^6}|\mu|^8 I_2^2 I_1 \Theta(\Delta t)\frac{1}{2\gamma}e^{-2\gamma\Delta t} \tag{2.13}$$

The results of TI-FWM, FWM-PS, and TR-FWM calculated for an ensemble of non-interacting two-level systems and Gaussian excitation pulses are shown in figure 2.4.

The TR-FWM signal appears immediately after the second pulse arrives in the sample and decays with the time constant $T_2/2$ — this is the free induction decay of the polarization. The FWM-PS signal is the power in the frequency domain and will be a Lorentzian line with full width at half max of $2\hbar/T_2$. The TI-FWM signal is identically zero for $\Delta t < 0$ and decays with the same time constant as the TR-FWM for $\Delta t > 0$.

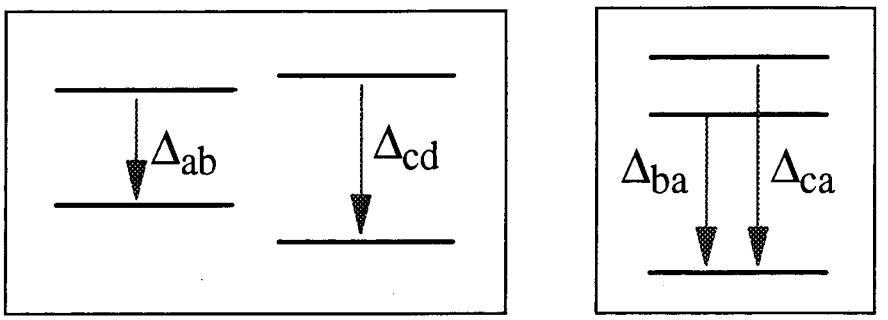

Figure 2.5: Multilevel Systems

The width of the resonance in the linear spectrum is also determined by T_2, so for the case of a homogeneously broadened ensemble of two-level systems, there is no new information to be gained from FWM. For an inhomogeneously broadened ensemble, the linewidth measured in the linear absorption is the inhomogeneous linewidth, i.e. the distribution of energies, Δ, in the ensemble. The FWM signal is emitted as a photon echo and not a free induction decay; it appears a time Δt after the second pulse and has a rise time and decay time given by the inhomogeneous linewidth. The homogeneous linewidth can be obtained by measuring the TI-FWM which decays with the time-constant $T_2/4$ [1].

We would like to discuss two slightly more complicated multilevel systems to make the distinction between polarization interference and quantum beats. Figure 2.5 shows the level diagrams for a four-level system and a three-level system both homogeneously broadened. In the four-level system, there are dipole transitions between levels a and b and between levels c and d, but there are no other possible transitions in the system. Thus the system can be thought of as two independent two-level systems. If we look at the emission from this system, it will consist of emission at the freqencies Δ_{ab} and Δ_{cd} which will beat resulting in oscillations in the emitted polarization.

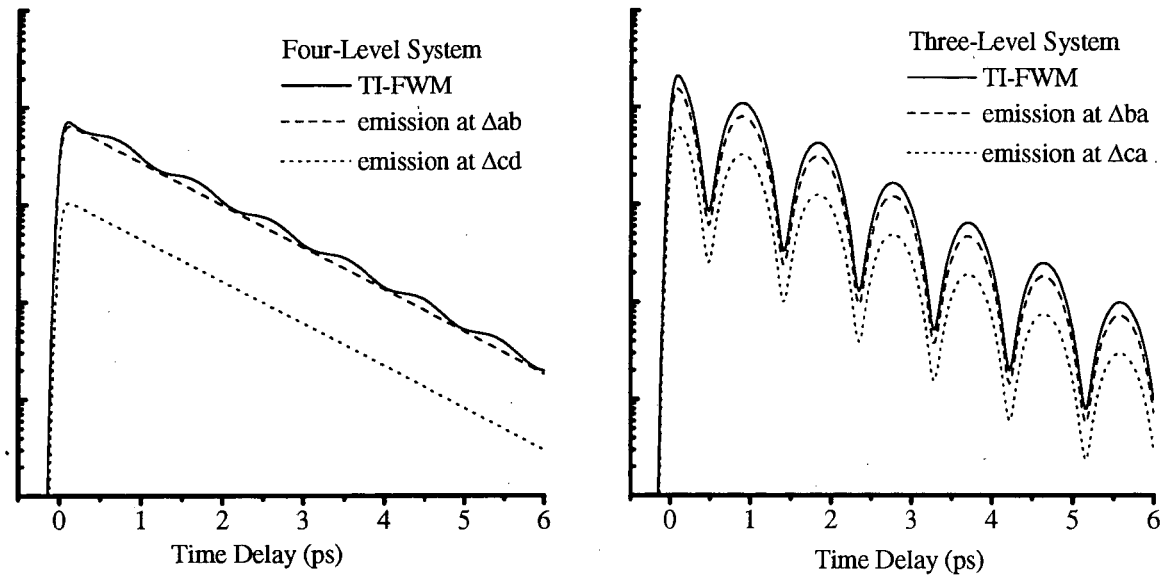

Figure 2.6: TI-FWM for a four-level and three-level system. These curves are calculated using the Liouville space formalism in [56]. The excitation pulses are Gaussian pulses. For the four-level system $\Delta_{ab} = 1.514eV$, $\Delta_{cd} = 1.518eV$, $\gamma_{ab} = \gamma_{cd} = 0.0005\text{fs}^{-1}$, and $\mu_{ab}/\mu_{cd} = 0.8$. For the three-level system $\Delta_{ba} = 1.514eV$, $\Delta_{ca} = 1.518eV$, $\gamma_{ba} = \gamma_{ca} = 0.0005\text{fs}^{-1}$, and $\mu_{ba}/\mu_{ca} = 0.8$.

In the three-level system, there are dipole transitions between levels b and a and between levels c and a. The three-level system will also emit at the frequencies Δ_{ba} and Δ_{ca}. The question is how to distinguish between the three-level and four-level systems by examining the optical emission. It is clear that these systems cannot be distinguished by their linear polarization or absorption. In both cases, there are two peaks in the spectrum and oscillations in the time domain.

On the other hand, the FWM provides several ways to distinguish between these two systems. Figure 2.6 shows that the TI-FWM for the two systems is clearly different. The oscillations are not only much more pronounced for the three-level system in the TI-FWM, but the emission from the two transitions separately also shows pronounced oscillations as a function of Δt. This is because the two transitions are coupled in the three-level system so that the populations of the excited levels oscillate as a function of Δt. In contrast,

in the four-level system, the emission from the two transitions does not show oscillations because they are decoupled. In an actual experiment, there will be small oscillations at a given frequency due to the finite linewidth of the emission from each transition [51]. The beating in the four-level system is known as polarization beating because it is entirely due to interference of the electromagnetic waves. In the case of the three-level system, it is known as quantum beating.

There is another way in which FWM can be used to distinguish between quantum beats and polarization interference [40]. If the time of emission of the TR-FWM is measured as a function of Δt, the relationship will be linear. A slope of one indicates that the polarization is emitted immediately after pulse 2 which is the case for quantum beats. A slope of two indicates that the polarization is emitted a time Δt after pulse 2, like an echo, which is the case for polarization interference.

2.7 The Semiconductor Bloch Equations

At first glance a semiconductor near the band edge is a multilevel system. If the excitonic states are being studied, the semiconductor can be thought of as a two-level system: the ground state is the unexcited state with no excitons and the excited state is the state with an exciton created. The continuum states can be modelled as an ensemble of inhomogeneously broadened two-level systems. Each state in k-space is a two-level system at a different energy given by the dispersion of the valence and conduction bands.

Optical experiments in semiconductors have been explained using a multilevel system approach (see, for example, [54] and [69]). However, the microscopic description of an optically excited semiconductor is, in general, a complicated problem in many-body

physics because of the strong interaction between all the excited electrons and holes in the semiconductor.

The correct starting point for calculating the optical response is the electron-hole Hamiltonian [26]. Here it is easiest to write the Hamiltonian in the second-quantized form.

$$\begin{aligned}\hat{H} &= \sum_{\mathbf{k}}\{\epsilon_{c\mathbf{k}} a^{\dagger}_{\mathbf{k}} a_{\mathbf{k}} + \epsilon_{h\mathbf{k}} b^{\dagger}_{\mathbf{k}} b_{\mathbf{k}}\} \\ &+ \frac{1}{2}\sum_{\mathbf{k}\neq\mathbf{k}'} V_{\mathbf{q}}\{a^{\dagger}_{\mathbf{k}+\mathbf{q}} a^{\dagger}_{\mathbf{k}'-\mathbf{q}} a_{\mathbf{k}'} a_{\mathbf{k}} + b^{\dagger}_{\mathbf{k}+\mathbf{q}} b^{\dagger}_{\mathbf{k}'-\mathbf{q}} b_{\mathbf{k}'} b_{\mathbf{k}} - 2a^{\dagger}_{\mathbf{k}+\mathbf{q}} b^{\dagger}_{\mathbf{k}'-\mathbf{q}} b_{\mathbf{k}'} a_{\mathbf{k}}\} \\ &- \sum_{\mathbf{k}} \vec{E}(t)\cdot\{\vec{\mu}_{cv} a^{\dagger}_{\mathbf{k}} b^{\dagger}_{-\mathbf{k}} + \vec{\mu}^{*}_{cv} b_{-\mathbf{k}} a_{\mathbf{k}}\}\end{aligned} \tag{2.14}$$

$$V_{\mathbf{q}} = \frac{4\pi e^2}{\Omega}\frac{1}{|\mathbf{q}|^2} \tag{2.15}$$

The first line of equation 2.14 gives the one particle energies of the electrons and holes and contains the band structure of the semiconductor in the electron-hole representation. The fermion operator $a^{\dagger}_{\mathbf{k}}$ creates an electron with wavevector $\mathbf{k}$ and $b^{\dagger}_{\mathbf{k}}$ creates a hole with wavevector $\mathbf{k}$. $\epsilon_{c\mathbf{k}}$ and $\epsilon_{h\mathbf{k}}$ give the energy dispersion for the conduction and valence bands respectively. Eqn. 2.14 includes only one conduction and one valence band, but it can easily be generalized to include more bands. We make the effective mass approximation, so that the electrons and holes can be treated as free particles. The band dispersion is then given by

$$\epsilon_{c\mathbf{k}} = \frac{1}{2}E_g + \frac{\hbar^2 k^2}{2m^*_e} \qquad \text{and} \qquad \epsilon_{h\mathbf{k}} = \frac{1}{2}E_g + \frac{\hbar^2 k^2}{2m^*_h}. \tag{2.16}$$

The Coulomb interaction of the full valence band is included in the band gap energy, E_g.

The second line of equation 2.14 is the energy of the Coulomb interaction between the electrons and holes. $V_{\mathbf{q}}$ is the unscreened Coulomb interaction in k-space. Only the monopole-monopole term of the Coulomb interaction is retained [30]. The last line is the

energy of the interaction with the applied electric field in the dipole approximation. $\vec{\mu}_{cv}$ is the dipole moment between the valence and conduction band states and is taken to be independent of the wavevector, $\mathbf{k}$. As with the multilevel system models, the rotating wave approximation will be made in calculating the polarization.

The polarization is given by the expression

$$\vec{P} = \sum_{\mathbf{k}} \vec{\mu}_{\mathbf{k}} \left\langle \hat{P}_{\mathbf{k}} \right\rangle = \sum_{\mathbf{k}} \vec{\mu}_{\mathbf{k}} \left\langle a^{\dagger}_{\mathbf{k}} b^{\dagger}_{-\mathbf{k}} \right\rangle \tag{2.17}$$

The dynamics of the polarization can be evaluated using Heisenberg's equation of motion for the polarization operator.

$$\frac{d}{dt}\hat{P}_{\mathbf{k}} = -\frac{i}{\hbar}[\hat{P}_{\mathbf{k}}, \hat{H}] \tag{2.18}$$

It is straightforward to calculate the result.

$$\begin{aligned} i\hbar\frac{d}{dt}\left\langle a^{\dagger}_{\mathbf{k}} b^{\dagger}_{-\mathbf{k}} \right\rangle &= (\epsilon_{c\mathbf{k}} + \epsilon_{h-\mathbf{k}}) \left\langle a^{\dagger}_{\mathbf{k}} b^{\dagger}_{-\mathbf{k}} \right\rangle - \sum_{\mathbf{q}\neq 0} V_{\mathbf{q}} \left\langle a^{\dagger}_{\mathbf{k}-\mathbf{q}} b^{\dagger}_{-\mathbf{k}+\mathbf{q}} \right\rangle \\ &+ \vec{\mu}\cdot\vec{E}(t)\left(1 - \left\langle a^{\dagger}_{\mathbf{k}} a_{\mathbf{k}} \right\rangle - \left\langle b^{\dagger}_{-\mathbf{k}} b_{-\mathbf{k}} \right\rangle\right) \\ &+ \sum_{\mathbf{k}',\mathbf{q}\neq 0} V_{\mathbf{q}}\{\left\langle a^{\dagger}_{\mathbf{k}} a^{\dagger}_{\mathbf{k}'} b^{\dagger}_{-\mathbf{k}+\mathbf{q}} a_{\mathbf{k}'+\mathbf{q}} \right\rangle - \left\langle a^{\dagger}_{\mathbf{k}+\mathbf{q}} a^{\dagger}_{\mathbf{k}'} b^{\dagger}_{-\mathbf{k}} a_{\mathbf{k}'+\mathbf{q}} \right\rangle \\ &+ \left\langle a^{\dagger}_{\mathbf{k}+\mathbf{q}} b^{\dagger}_{-\mathbf{k}'+\mathbf{q}} b^{\dagger}_{-\mathbf{k}} b_{-\mathbf{k}'} \right\rangle - \left\langle a^{\dagger}_{\mathbf{k}} b^{\dagger}_{-\mathbf{k}'-\mathbf{q}} b^{\dagger}_{-\mathbf{k}+\mathbf{q}} b_{-\mathbf{k}'} \right\rangle\} \end{aligned} \tag{2.19}$$

The first line of eqn. 2.19 gives the behavior of the undriven polarization. The first term gives the frequency dependence of the polarization due to the band structure and the second term is the Coulomb interaction between the electron and hole which results in the excitonic structure. This equation is formally equivalent to the equation for the hydrogen atom. The second line is the driving term resulting from the applied electric field. The first term in this line is responsible for the linear optics. The other two terms are proportional to the density of electrons and holes respectively and result in the same nonlinear signal which is seen in multilevel systems. This is the Pauli Blocking (PB) nonlinearity.

The third and fourth lines describe the nonlinear contribution to the polarization due to interactions between four-particles. These terms are responsible for much of the interesting physics in the optical response of semiconductors. They are also the source of the computational difficulty.

Without these terms involving four-particle correlations (by which we mean the expectation value of four particle operators), the polarization would only be coupled to the populations of electrons, $n_e = \langle a_k^\dagger a_k \rangle$, and holes, $n_h = \langle b_k^\dagger b_k \rangle$. The equations of motion for the populations can be calculated in the same manner as the equation for the polarization and, neglecting the four-particle correlations, we would have a closed set of three equations.

If we do not neglect the four-particle correlations, we must calculate the equations of motion for the four-particle correlations. We find that they are driven by six-particle correlations. The six-particle correlations are, in turn, driven by eight-particle correlations and so on in a never-ending hierarchy. Some approximation must be made which truncates this hierarchy of equations.

The most common approximation in dealing with semiconductors has been to factorize the four-particle correlations into products of two-particle correlations and make the random phase approximation (RPA), in which terms which oscillate rapidly due to large momentum differences are ignored. For example,

$$\begin{aligned} \left\langle a_k^\dagger a_{k'}^\dagger b_{-k+q}^\dagger a_{k'+q} \right\rangle &\overset{\text{factorization}}{\approx} \left\langle a_k^\dagger a_{k'+q} \right\rangle \left\langle a_{k'}^\dagger b_{-k+q}^\dagger \right\rangle \\ &\overset{\text{RPA}}{\approx} \left\langle a_k^\dagger a_{k'+q} \right\rangle \left\langle a_{k'}^\dagger b_{-k+q}^\dagger \right\rangle \delta_{k,k'+q} = n_{ek} P_{k-q} \end{aligned} \tag{2.20}$$

This approximation is also known as the time-dependent Hartree-Fock approximation. This leads to a set of equations for the two-particle density matrix which are the well known

Semiconductor Bloch Equations (SBE) [65]. The SBE in the relaxation time approximation are given below [26].

$$\frac{\partial}{\partial t}P_k + i(e_{\mathbf{ck}} + e_{h\mathbf{k}})P_k = i(1 - n_{ek} - n_{hk})\omega_{Rk} - \frac{1}{T_2}P_k \tag{2.21}$$

$$\frac{\partial}{\partial t}n_{bk} = -2Im(\omega_{Rk}P_k^*) - \frac{1}{T_1}n_{bk} \quad (b = e, h) \tag{2.22}$$

$$\hbar e_{b\mathbf{k}} \equiv \hbar\epsilon_{b\mathbf{k}} + \sum_q V_{k-q}n_{bq} \quad (b = e, h) \tag{2.23}$$

$$\omega_{Rk} \equiv \frac{1}{\hbar}\left\{\vec{d}_{cv}\cdot\vec{E} + \sum_{q\neq k} V_{k-q}P_q\right\} \tag{2.24}$$

The SBE are a mean-field theory at the level of the 2-particle correlations. Thus, they account for the exciton and all other 2-particle correlation effects, but neglect higher-order correlations. In eqns. 2.21 and 2.22, the elements of the density matrix, P_k, n_{ek}, and n_{hk} interact with an effective field, ω_{Rk}, which includes both the externally applied electric field and a term due to the polarization from all the other k states. Mean-field theories have played an important role in condensed matter physics. The BCS theory of superconductivity [67], the Heisenberg equation in magnetism [3] and the Landau-Ginzburg equation in thermodynamics are all mean-field theories. The SBE have been successful in explaining and predicting many experiments in semiconductors, including the AC Stark effect [65, 66], TR-FWM in quantum wells [83], phase measurements [18], and photon echoes from the continuum states [24, 48] to name a few.

One important result explained by the SBE, relevant for this work, is the existence of a FWM signal for $\Delta t < 0$ for experiments done on excitons in GaAs quantum wells [45, 81]. The SBE showed that this signal is a result of interactions between the exciton polarizations via the Coulomb interaction. This term results in a signal for $\Delta t < 0$ which rises twice as fast as the decay, as was seen experimentally. The prediction of a rise time

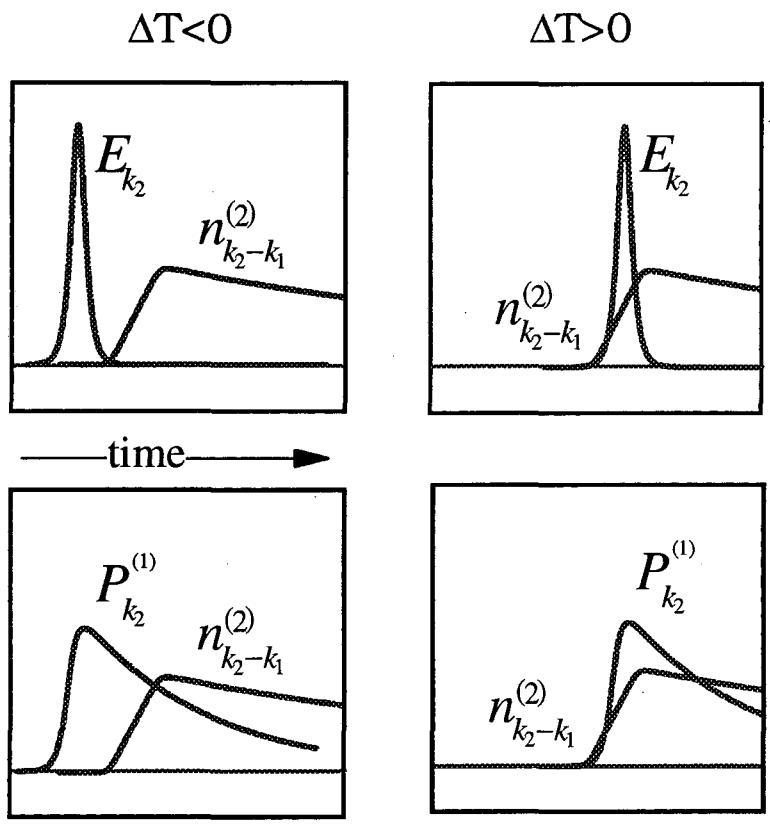

Figure 2.7: The PB nonlinearity (top) only produces a signal for $\Delta t > 0$. the BCI nonlinearity (bottom) produces a signal for $\Delta t < 0$ as well.

of $T_2/4$ is a very general result of the SBE and is not dependent on the details of the excitation or the material assuming homogeneous broadening. Inhomogeneous broadening in the sample results in a weaker signal for $\Delta t < 0$ [31].

The PB nonlinearity is the interaction of the laser pulse with the coherent population, $\propto E_{k_2}(t)n_{k_2-k_1}(t)$, and only results in a signal for $\Delta t > 0$ when the electric field and the coherent population overlap in time. (The subscripts refer to the modulation imposed by the wavevector of the pulses and not the crystal momentum.) The nonlinearity due to the bare Coulomb interaction (BCI) — the Coulomb interaction in the mean field approximation — is the interaction of the polarization with the coherent population, $\propto P_{k_2}(t)n_{k_2-k_1}(t)$. Because the polarization lasts much longer than the laser pulse, there is an interaction for

$\Delta t < 0$. This is shown schematically in Fig. 2.7.

2.8 Failures of the SBE

Because the SBE in the relaxation time approximation neglect all correlations beyond the 2-particle correlations, they are unable to explain some important experimental results. The most glaring omission of the SBE is the bound biexciton. Because the SBE factorize all four-particle correlations, they are unable to account for the binding of two excitons which is a correlated state of two electrons and two holes. In some cases, biexcitonic effects in FWM experiments have been explained using a multilevel system approach where the bound biexciton is a state at energy, $2\Omega_x - \epsilon_B$, where Ω_x is the exciton transition energy and ϵ_B is the biexciton binding energy [9, 54].

Another important failing of the SBE is their inability to explain the polarization dependence of the FWM signal. Experimentally, it is found that the FWM signal for two cross linearly polarized input pulses is weaker than that for co-linearly polarized excitation whereas the SBE predict that both signals should be of equal intensity (although not necessarily identical in form) [7].

Different approximation schemes have been used to extend the SBE beyond the relaxation time approximation. One well-known scheme is the inclusion of excitation induced dephasing (EID) [79, 29]. In this scheme the density dependence of the dephasing rate, γ, is calculated. EID is again the result of higher-order correlations. In the case of interactions with an incoherent bath of free electrons and holes, it is reasonable to factorize the higher-order correlations, and the dephasing, γ, can be calculated within the screened Hartree-Fock approximation. In the low-density limit, only the linear term in the excitation

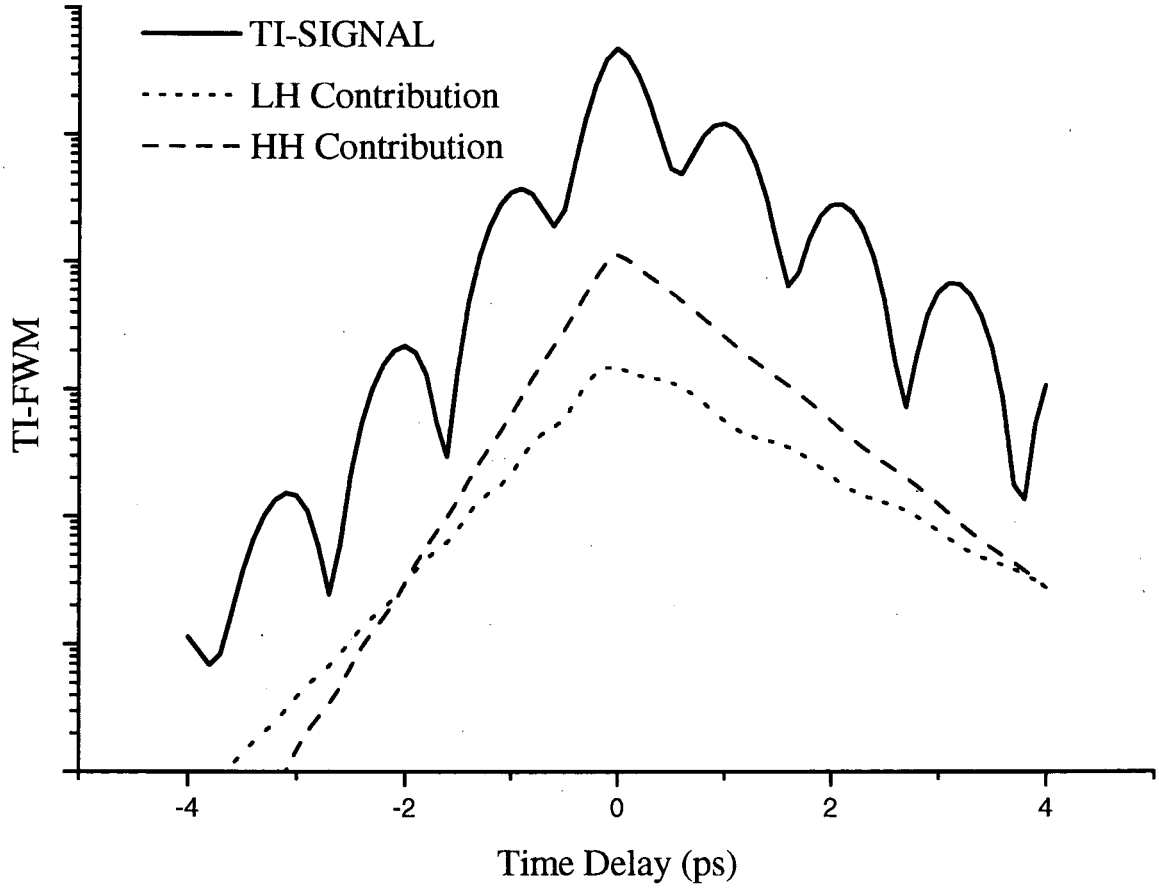

Figure 2.8: SBE Calculation of TI-FWM for bulk GaAs in a magnetic field

density is included and the dephasing can be written $\gamma = \gamma_0 + \gamma' \Delta n$, where Δn is the excitation density. Calculations within the EID approximation to third order in the electric field show qualitatively the polarization dependence of the FWM intensity seen experimentally. Calculations to fifth order in the electric field show a change in dephasing time with density. In [79], a pre-pulse was used to create a quasi-thermal incoherent electron-hole bath, so the screened Hartree-Fock approximation seems reasonable, but care must be taken in calculating EID for coherent measurements such as FWM. EID does not affect the rise time for $\Delta t < 0$ predicted by the SBE [80].

Parameters for unstrained GaAs [13]:	
The band gap, E_g	1.5192eV
Energy of the split-off band, Δ_0	0.341eV
the background dielectric constant at 1.6K, ϵ	12.40
conduction band effective mass, m_e	$0.0665m_0$
hh-band effective mass, m_{hh}	$0.5m_0$
lh-band effective mass, m_{lh}	$0.082m_0$
Parameters for GaAs in a magnetic field [25]:	
hh-X reduced mass, μ_{hh}	$0.042m_0$
hh-X Bohr radius, a_0^{hh}	156Å
hh-X binding energy	3.7meV
lh-X reduced mass, μ_{lh}	$0.052m_0$
lh-X Bohr radius, a_0^{lh}	126Å
lh-X binding energy	4.6meV
Magnetic field at which $\lambda_c = a_0$, B_c^{hh}	2.7 Tesla
B_c^{lh}	4.1 Tesla

Table 2.1: Important parameters for GaAs.

2.9 SBE calculation of GaAs in a magnetic field

Figure 2.8 shows a calculation of the SBE in the relaxation time approximation corresponding to our experiment: TI-FWM for bulk GaAs in a magnetic field excited with σ^- polarized light. The calculation is performed on a mixed basis of plane-wave states with $\vec{k} \parallel \vec{B}$ and Landau levels, keeping only the contribution from the lowest Landau level. Here we see the characteristic rise and decay times of $1/4\gamma$ and $1/2\gamma$. Also notice that while there are oscillations in the total signal, there are almost no oscillations at the lh-X or hh-X independently. GaAs excited with σ^- polarized light resembles the 4-level system mentioned previously. As mentioned before, in this system the transitions are not coupled quantum-mechanically — either by PB or the mean-field Coulomb interaction — and the beating in the signal is due to polarization interference.

2.10 Conclusion

In this chapter, we have reviewed the band structure of GaAs and the theory of four-wave mixing in semiconductors. The relevant parameters for GaAs are summarized in table 2.1. Exciting with σ^- polarized light, the lh-X and hh-X do not interact, and lh-X/lh-X and hh-X/hh-X bound biexcitons cannot be formed. Some FWM experiments in semiconductors can be explained using multilevel system models, but because the electron-hole pairs interact via the Coulomb interaction, there are interaction effects which go beyond these models. The Semiconductor Bloch Equations include the Coulomb interaction within the time-dependent Hartree-Fock approximation which includes all correlation effects at the 2-particle level. Because higher order correlations are ignored, the SBE cannot explain some important features of optical experiments in semiconductors.

Chapter 3

Experimental Setup

3.1 Introduction

The geometry of two-pulse degenerate four-wave mixing (FWM) experiments (Fig. 3.1) was described in the previous chapter, as were the three measurements that can be made on the FWM signal: time-integrated FWM (TI-FWM), time-resolved FWM (TR-FWM), and the FWM power spectrum (FWM-PS). In this chapter, the equipment used to make these measurements is described. The two main pieces of equipment needed are the laser for exciting the sample and the magneto-optic cryostat which applies the magnetic field and keeps the sample at a temperature of 1.6K. In addition there are optical and mechanical components for sending the pulses around the table and delaying one pulse with respect to the other. Finally there is a spectrometer for the frequency characterization and electronics for detecting the FWM signal. The structure and processing of the bulk GaAs samples will also be described, as will the details of a few other measurements and calculations that are necessary for evaluating the FWM experiments.

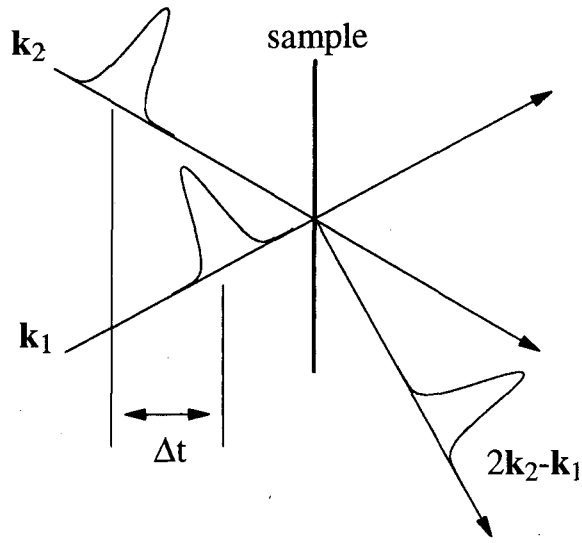

Figure 3.1: The FWM Configuration.

For our experiments, the excitation pulses were co-circularly polarized (σ^-) $\sim$ 100fs pulses from a Ti:Sapphire laser with central wavelength $\lambda \sim$ 820nm, resonant with the excitonic lines. The samples were high quality layers of MBE grown bulk GaAs, and the measurements were made in magnetic fields between 0T and 10T in the Faraday configuration ($\vec{k} \parallel \vec{B}$ — $\vec{k}_1$ and $\vec{k}_2$ are close to parallel.). The majority of the measurements were made at a temperature of 1.6K.

3.2 The laser system

The laser we used for these experiments was a Ti:Sapphire laser built from the NJA-2 kit manafactured by Clark MXR. The laser reliably produced output pulses with a length (FWHM) between 80 and 120fs and with output power between 200 and 330 mW. For most of the experiments, the laser was in a configuration in which a dye jet was installed in the cavity to assist in modelocking so that the laser would be self-starting. Two extra

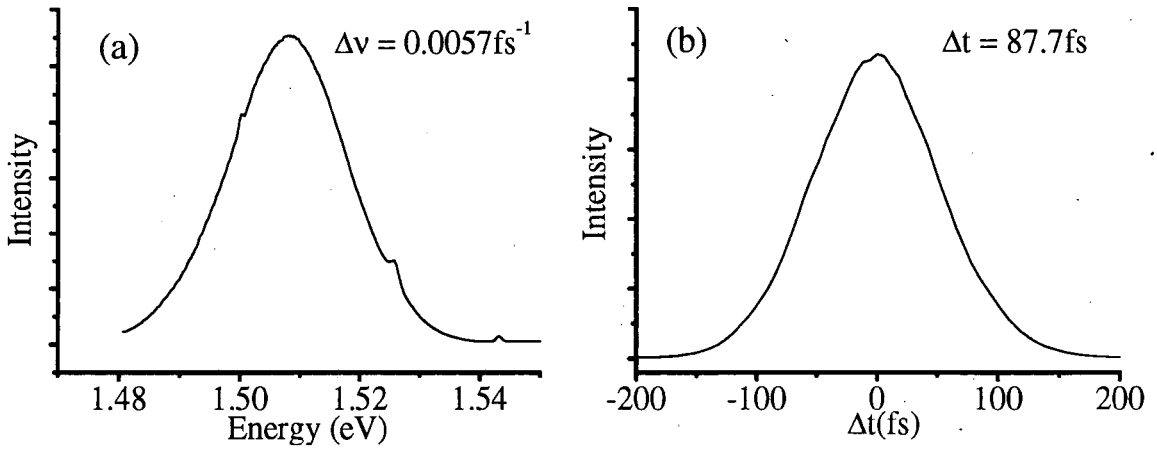

Figure 3.2: typical laser spectrum and autocorrelation. From these measurements, $\Delta\nu\Delta t = 0.5$ where $\Delta\nu$ and Δt are the full-width half-maximum (FWHM) values of the electric field intensity in the frequency and time domains respectively. For transform limited pulses $\Delta\nu\Delta t = 0.4413$.

curved mirrors were placed in the cavity to focus the beam in the jet. In this configuration, the pulse repetition rate, determined by the cavity length, was 86MHz. The dyes used were HITCI and IR140 dissolved in an ethylene glycol jet. For some of the experiments the laser was in a configuration without the dye jet. In this configuration, the output characteristics of the laser pulses were virtually the same as before, but the laser was not self-starting and the repetition rate was 105MHz.

In general, the laser was characterized by its autocorrelation (AC) and spectrum. The AC was taken using the same two pulses used for the FWM experiments (beams 1 and 2 in Fig. 3.4), focused into a 100μm thick KDP crystal. The two pulses were not collinear so that the AC signal (at the second harmonic) was in a background free direction. The AC signal was detected with a Hamamatsu 931A PMT and sent to a SR530 lockin amplifier. The spectrum was detected with the same setup as the FWM-PS. When measuring the laser spectrum and other coherent sources with large bandwidths, tracing paper was sometimes placed over the entrance slit to the spectrometer to reduce problems due to interference

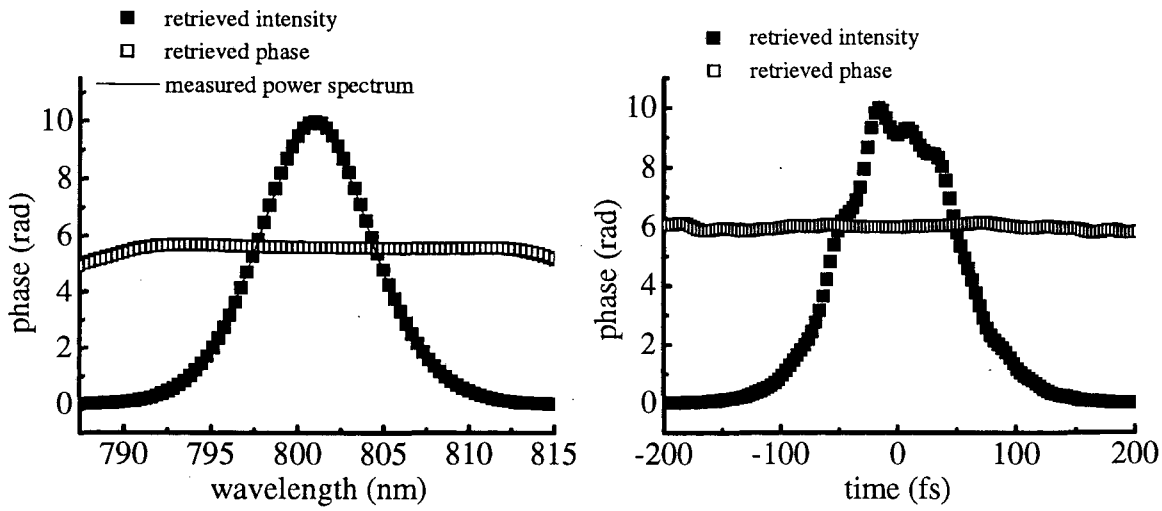

Figure 3.3: Results of a FROG measurement on the laser giving both the phase and amplitude of the electric field in both frequency (left) and time (right). Courtesy of M. V. Marquezini

within the spectrometer. A typical autocorrelation and spectrum are shown in figure 3.2. The pulses are close to Gaussian in shape and are typically close (within 15%) to the transform limit. In some configurations, there is some structure on the laser spectrum, as seen in Fig. 3.2, but the pulses are well-behaved and the experimental results are not affected.

The laser was also characterized a few times by frequency resolved optical gating (FROG) [20, 75]. In our configuration the optical gate was the same second-harmonic crystal used for the AC measurements. With this technique both the amplitude and phase of the electric field of the pulse can be determined. Figure 3.3 shows the results of the laser characterization on a typical day. The pulse shape is reasonably well fit by a Gaussian, and the phase of the pulse varies by less than $4.5 \times 10^{-2}\pi$ between the 2% points of the power spectrum [53].

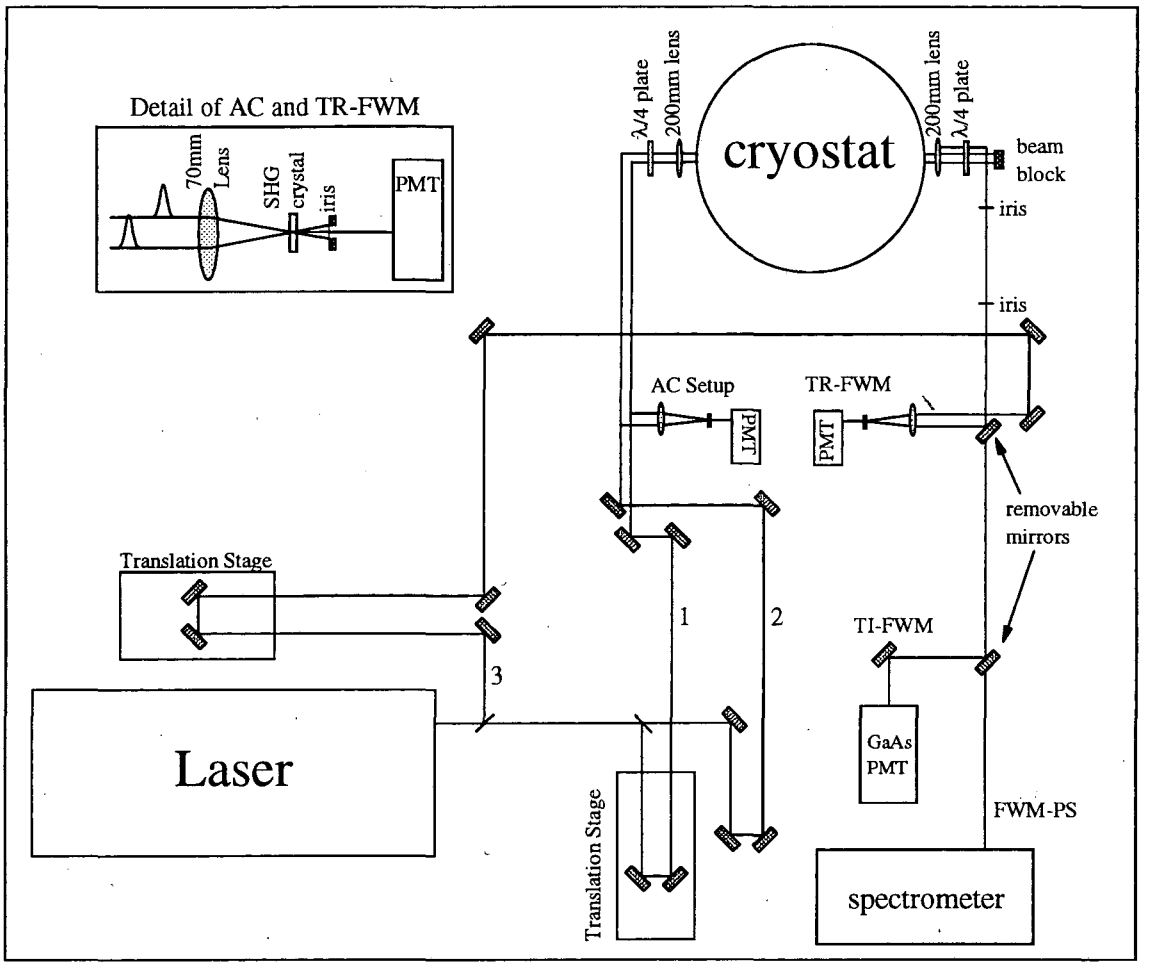

Figure 3.4: Layout of the Optical Table

3.3 Optical setup

A schematic diagram of the optical layout is shown in figure 3.4. This is a standard layout for FWM measurements. The pulse from the laser is split into 3 beams using two beamsplitters. Two pulses are sent into the cryostat to excite the sample, and the third pulse is the reference pulse used to measure the TR-FWM, as will be described in the next section. The mechanical stage in the path of beam 1 allows the delay of that pulse to be varied. The stage is a Klinger stepper motor with 0.1μm step size which allows time delay

increments of 0.667fs.

Beams 1 and 2 are aligned parallel approximately 8mm apart and 14cm above the optical table. The parallelism is checked by adjusting the separation at two points, one close to the steering mirrors and the other as far away as possible. A mirror on a removable magnetic mount can be placed in the beam path, sending both beams to the autocorrelation setup.

Two mirrors (not shown in Fig. 3.4) then send the beams to a height of 30cm to be sent through the cryostat. A zero-order $\lambda/4$ plate is placed directly before the focussing lens in front of the cryostat to create σ^- polarized light. The degree of polarization is better than 99.9%. With a separation of 8mm between the beams at the lens and a 200mm focal length, the angle between $\vec{k}_1$ and $\vec{k}_2$ is $\sim 2°$. The lens is a two inch lens with a nominal focal length of 200mm. There are two windows of either spectrosil WF or fused silica between the lens and the sample. The total thickness of glass is 5.175mm.

After the cryostat, the beams are sent down to the table (14cm) with two 2 inch mirrors. All three beams (at $\vec{k}_1$, $\vec{k}_2$, and $2\vec{k}_2 - \vec{k}_1$) can be captured by the mirrors, and any one of the beams can be aligned through the irises which send the beam into the characterization setup. This allows us to easily align different experiments such as pump-probe or linear characterization of the transmitted pulse.

3.4 Four-wave mixing detection and measurement

When describing the FWM setup and theory, a single FWM measurement is described in which two pulses of light are sent into the sample and the FWM pulse energy is measured. In a real experiment, this measurement is repeated at the repetition rate of

the laser ($\sim$ 12ns in our case), and the power not the energy is measured. In TI-FWM, the power in the FWM signal is measured as a function of time-delay, Δt. The input beams, $\vec{k}_1$ and $\vec{k}_2$, are differentially chopped with a HMS chopper, and the FWM signal is sent into a photo-multiplier tube (PMT). We use a RCA C31034A PMT with a GaAs photocathode in a water-cooled Products for Research housing. Typically, the PMT is biased at -1200V, and the FWM signal is reduced by a factor of $10^{1.5}$ with two ND filters before being sent into the detector. The PMT output is converted to a voltage with a $100K\Omega$ resistor and measured with the lock-in amplifier (Stanford Research Systems 530) which is referenced to the chopper. The signal is then recorded as the time delay of pulse 1 is varied. The output voltage measured varies from tens of microvolts to tens of millivolts. To estimate the background signal due to scattering, the signal was measured at large positive and negative time delays ($|\Delta t| > 30$ps). The background signal could be different for positive and negative time delays when the background was due to a pump-probe signal scattered into the FWM direction. The TI-FWM was corrected by subtracting off the background signal from the measurements for all Δt, using different background measurements for $\Delta t > 0$ and $\Delta t < 0$.

In a FWM-PS measurement, the power in the FWM signal is measured as a function of frequency at a given time delay. The FWM-PS is measured by sending the FWM signal into a spectrometer and optical multichannel analyzer (OMA). A background signal due to scattering and fluorescence is subtracted by measuring the spectrum with each beam individually blocked and then subtracting these two spectra from the measured FWM-PS. If the scattering and fluorescence are large compared with the FWM signal, this subtraction will typically not work well because it does not account for the phase of the light.

For most of the measurements, the spectrometer used was a 0.25m SPEX with a 1200 gr/mm grating. A diode array (EG&G Electronics) measured the spectrometer output and the diode array signal was sent to the OMA (also EG&G) which, in turn, was connected to the computer via a GPIB connection. The dispersion of this spectrometer was 0.059 ± 0.0001 nm/pixel. The spectrometer was calibrated using an Oriel argon lamp. For some experiments we used a 0.75m spectrometer (Spectra Pro 750 from Acton Research Corporation) with a 1200 gr/mm grating. The dispersion of this spectrometer was 0.0234 nm/pixel.

Lastly, the TR-FWM is a measurement of $|P_{FWM}(t, \Delta t)|^2$ as a function of time at a given time delay. This measurement is made by cross-correlating the FWM signal with a reference pulse (beam 3 in Fig. 3.4) from the laser in a 1mm thick BBO crystal. The second harmonic signal is then measured with a PMT (Hamamatsu 931A mounted in a Products for Research housing). If the reference pulse is short in comparison with $P_{FWM}(t, \Delta t)$, the second harmonic signal as a function of the time-delay of the reference pulse will be proportional to the FWM signal.

3.5 Finding the signal

To find the FWM signal, the input beams were aligned parallel as carefully as possible, and the zero delay was found by taking the autocorrelation. The zero delay of the autocorrelation did not correspond exactly to zero delay in the sample because the AC was not taken at the sample position, but the zero-delay of the FWM was always within about 200fs of the zero-delay of the AC.

We looked for the FWM signal at the output of the cryostat with an IR viewer,

looking on either side of the transmitted beams 1 and 2. Beams 1 and 2 were blocked directly after the cryostat so that the much weaker FWM signal could be detected. Unfortunately, when there is a lot of scattering, this technique does not work. Then it is sometimes helpful to image the sample surface onto a CCD camera to adjust the overlap of the pulses; when the pulses are overlapped on the sample, the interference can clearly be seen. Another technique for maximizing the overlap and determining the zero time delay is to measure the pump-probe signal which is much easier to align. Some luck is then needed to find the position of the FWM signal. The location of the FWM signal in relation to the two transmitted beams is known, so its path can be estimated and aligned into either the spectrometer or the PMT. Differentially chopping the input beams, the lock-in should read a maximum signal when the FWM is aligned correctly into the PMT. A scattered pump-probe signal will also be detected by the lock-in, so the response of the signal to time-delay must be checked. A pump-probe signal has a step-function response. On the spectrometer, the FWM signal has emission peaks at the lh-X and hh-X at low excitation density and the signal should disappear if either beam is blocked.

3.6 The magnet

The samples were housed in a magneto-optic cryostat custom built by Oxford Instruments, Inc. The magnet was a superconducting split-coil which operates between 0 and 11.8 Tesla and is uniform to better than 0.25% in a 10mm diameter spherical volume centered at the sample position. A cross section of the cryostat is shown in figure 3.5.

The samples were mounted on a flat metal sample holder with teflon tape. The sample holder was, in turn, mounted onto a 112cm sample arm that was inserted into the

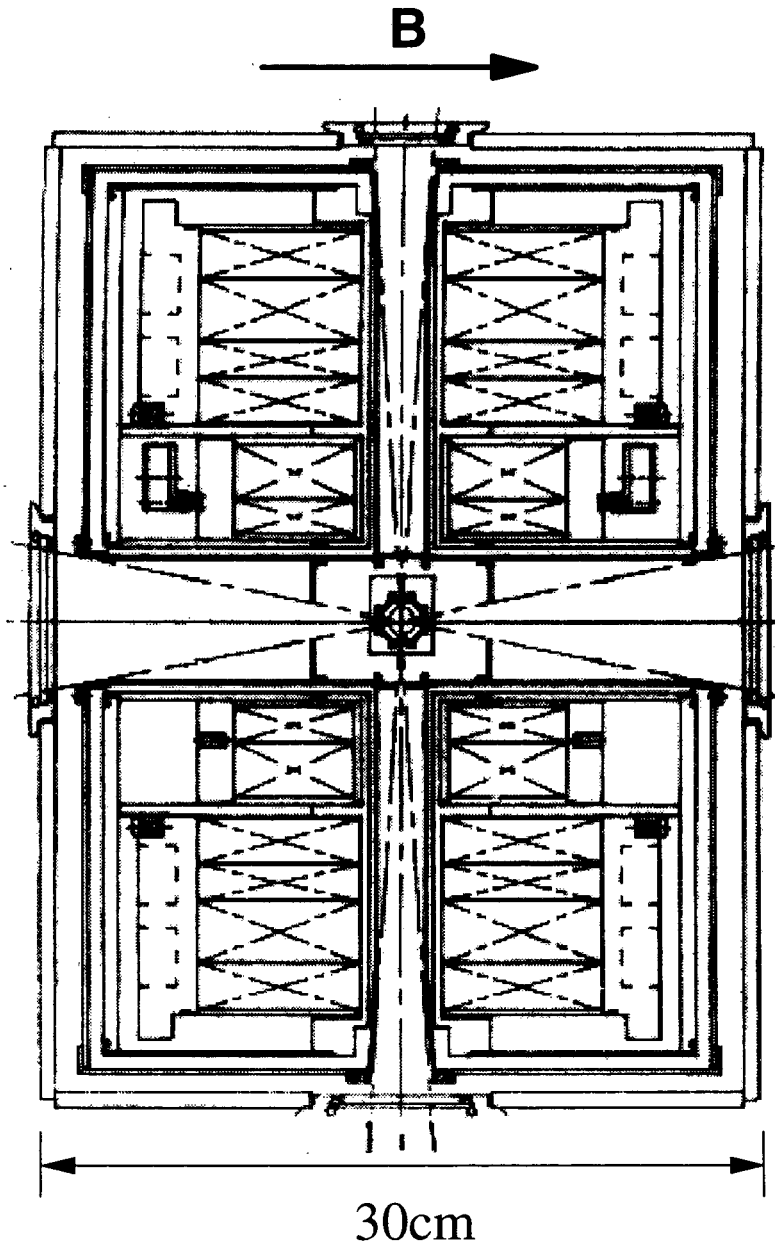

Figure 3.5: Magnet cross-section. The angular aperture is 25.5°.

sample cell. Most of the time, the system was stable, but we occasionally had problems with mechanical vibrations which may have been due to the long sample arm.

A capillary tube connected the sample cell to the helium reservoir. By opening a valve controlling the flow through the capillary and pumping on the sample cell, the temperature of the sample could be brought below 2K. The temperature of the sample was measured with a carbon glass resistor mounted just above the sample holder. In addition, there was a carbon glass resistor mounted at the base of the sample cell.

Also at the base of the sample cell was a resistive heating element. By regulating the flow of helium through the capillary and controlling the heater automatically, the temperature of the sample could be controlled with a feedback loop. In practice this feedback loop regulated the temperature measured at the base of the sample cell. The temperature measured on the sample holder would then stabilize at a higher value. It was not possible to regulate the feedback loop with the temperature sensor on the sample holder because this introduced a pure time delay into the feedback loop so that it was unstable. The feedback loop is a proportional-integral-derivative (PID) feedback loop in the Oxford ITC4 temperature controller; We found that the values 90%, 0.3 minutes, and 0 minutes worked well for the proportional, integral and derivative settings for our system.

We used both an Alcatel 2063C mechanical pump with a displacement of 50 cfm and a Leybold Sogevac UV25 with a displacement of 17 cfm to pump on the sample cell. The Alcatel pump was capable of bringing the sample to 1.6K with a pressure of < 1 Torr in the sample cell. The Leybold pump brought the temperature to 1.8K with a pressure of ~ 5 Torr in the sample cell.

3.7 Samples

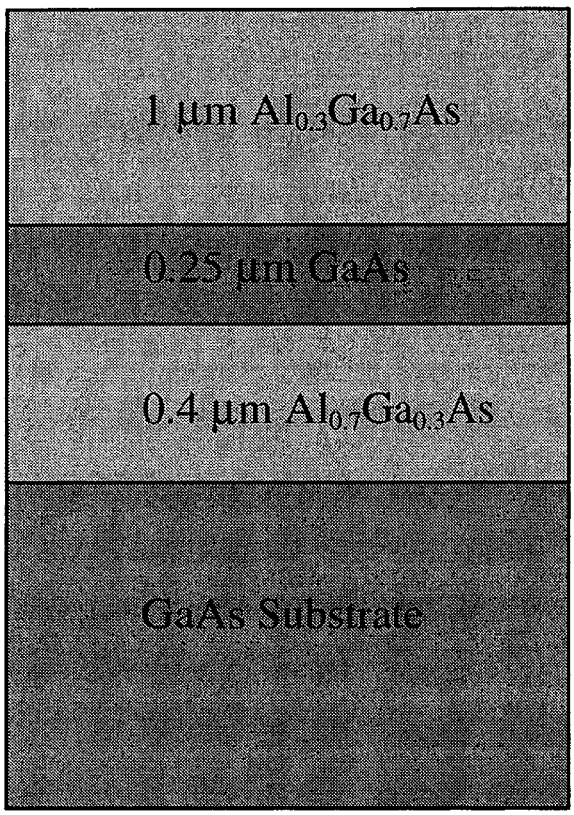

Figure 3.6: Structure of the 0.25μm Sandia sample.

Most of the measurements in this work were made on a 0.25μm thick layer of bulk GaAs grown at Sandia National Laboratories. All measurements mentioned in this work were taken on this sample unless explicitly stated. I will also discuss a few measurements taken on a 1.0μm sample, and 0.5μm and 0.25μm samples grown at Bell Labs. The 0.25μm Sandia sample consists of an AlGaAs layer, the 0.25μm GaAs layer, and another AlGaAs layer grown by MBE on a bulk GaAs substrate. The two AlGaAs layers serve to remove the bulk layer from the surface so that band-bending effects are avoided. The AlGaAs layer between the substrate and GaAs layer also serves as the stop etch layer. The sample structure is shown in figure 3.6.

The entire 2 inch wafer was anti-reflection coated on the polished side. An approximately 3mm x 3mm piece of the wafer was cleaved and glued to a sapphire window with UV cured Norland optical adhesive 61. Sapphire was chosen because of its high thermal conductivity. The window was 1.0 mm thick and 11mm diameter, c-axis cut to avoid any problems due to bi-refringence. The bulk GaAs substrate was then sanded to a thickness of 0.004 inches after which the rest of the substrate was chemically etched until the stop

etch layer was reached [47]. We used a jet etch (Model 550D Single Vertical Jet Electropolisher from South Bay Technology) for the etching process. The progress of the etching was monitored with a Zeiss microscope. The surface would appear wavy before the stop-etch layer was reached, and would become very smooth at the stop-etch layer. After the etching, the etched side was anti-reflection coated. The anti-reflection coating is a single $\lambda/4$ layer of Si_3N_4 (the refractive index and thickness were measured to be 2.09 and 1018Å by Dr. Howard at Sandia National Laboratories). The compressive mechanical strain in our samples is the result of the different thermal contraction of the GaAs layer and the sapphire window when the sample is cooled to 1.6K.

The 0.25μm and 0.5μm samples from Bell Labs have a 100Å GaAs layer at the polished surface, a 0.5μm $Al_{0.3}Ga_{0.7}As$ layer, the 0.25μm or 0.5μm bulk GaAs layer, a 1.0μ $Al_{0.3}Ga_{0.7}As$ stop-etch layer, and an additional 1.0μm of MBE grown GaAs on the GaAs substrate. The purpose of the 100Å layer at the surface is to prevent oxidation of the $Al_{0.3}Ga_{0.7}As$. The 1.0μm sample consists of a 1.08μm GaAs layer on the surface, a 1.0μm $Al_{0.3}Ga_{0.7}As$ etch stop layer, and the bulk substrate.

3.8 Linear absorption measurements

The linear absorption of the sample was measured by transmission measurements done with an incandescent light bulb. The light bulb was collimated with a simple lens of between 50mm and 70mm focal length, and polarized in the same direction as the laser with a Glan-Thompson polarizer. The light beam was focused onto the sample using the optics of the FWM setup and was sent to the spectrometer. Spectra were taken with and without

the sample in place, and the absorption coefficient was calculated according to Beer's law,

$$\alpha(\omega) = \frac{-1}{L} \ln \frac{I_{ws}(\omega)}{I_{ns}(\omega)} \tag{3.1}$$

where L is the sample thickness, $I_{ws}(\omega)$ is the transmission spectrum measured through the sample, and $I_{ns}(\omega)$ is the spectrum measured without the sample. Because the light bulb is not a perfect point source – due to the finite size of the filament – the spot size of the focussed beam is large and the whole sample is illuminated. As a result, the inhomogeneity of the exciton energy due to inhomogeneous strain in the sample results in a larger linewidth measurement for the absorption spectra taken with the light bulb. The resolution of the SPEX spectrometer was also a limiting factor in measuring the linewidth of the lowest lying excitonic states.

Linear absorption spectra were also taken with the laser and the 0.75m spectrometer. These measurements give more accurate linewidths, but have their own difficulties. The energy range that can be measured is narrow. Interference effects can result in a noisy spectrum (as mentioned before tracing paper was sometimes used to minimize these problems) and fluctuations in the central frequency of the laser pulse can cause problems in the calculation of $\alpha(\omega)$.

3.9 Spot size measurements

The spot size of the focused pulses on the sample was measured by passing a knife edge through the beam and recording the intensity transmitted around the knife edge. The measurement could not be made directly at the sample position. Instead, the beams were steered alongside the magnet and the lens was place in the path so the beam followed an

equivalent path length with the same optics. The distance to the knife edge was measured to be the same as that to the sample within the cryostat and an equivalent amount of glass was placed in the sample path.

The knife edge measurements were typically made by mounting the knife edge, a razor blade, on a Klinger stage so that the data could be collected automatically. Measurements were also made with the knife edge mounted on a Line Tool translation stage when a Klinger stage was not available. The power as a function of knife edge position was then fitted to an error function to extract w_0, the beam waist assuming a Gaussian TEM_{00} mode. The fits were quite good, indicating that the beam had a good profile. The lens was mounted on a translation stage along the beam direction so that the lens focus could be found. The beam waist was measured as a function of lens position, and this data was fitted to the parameter $w(z)$ of a Gaussian TEM_{00} mode.

The measured beam waist was $w_0 = 26.6 \pm 1.0$ microns. Because we cannot be absolutely certain that the sample is at the focus, this value represents a lower bound for the spot size.

3.10 Density calculations

Once $\alpha(\omega)$ and the spot size are known, the excitation density can be calculated. The total power absorbed per unit area in the sample is

$$\int d\omega I(\omega)(1 - e^{-\alpha(\omega)L})\text{W-cm}^{-2} \tag{3.2}$$

where $I(\omega)$ is the laser intensity and $\alpha(\omega)$ is the absorption coefficient of GaAs. The average number of carriers created by one pulse per unit length in the z direction — the propagation

direction — per unit area in the xy plane is

$$\frac{1}{Lf}\int d\omega \frac{I(\omega)}{\hbar\omega}(1-e^{-\alpha(\omega)L})\ \mathrm{cm}^{-3} \tag{3.3}$$

where f is the laser repetition rate. The intensity is, of course, not uniform in the radial direction (the plane $\perp \vec{k}$). We approximate $I(\omega)$ by averaging the intensity for $r < w_0$. For a Gaussian beam with peak intensity I_0, the average intensity is

$$\tilde{I} = 0.865\frac{I_0}{2} = \frac{0.865P_t}{\pi w_0^2} \tag{3.4}$$

where P_t is the total power in the beam as measured with a power meter (Newport 815). The profile of the laser spectrum, $L(\omega)$, can be measured with the spectrometer and normalized so that

$$\int d\omega L(\omega) = 1 \tag{3.5}$$

Thus the carrier density is

$$N = \frac{0.865P_t}{\pi w_0^2 Lf}\int d\omega \frac{L(\omega)}{\hbar\omega}(1-e^{-\alpha(\omega)L})\mathrm{cm}^{-3} \tag{3.6}$$

The integral is calculated numerically from the absorption data and the measured laser spectrum.

This carrier density estimate is an upper bound: The spot size is a lower bound. The quantum efficiency is assumed to be 100%. The absorption is not corrected to account for bleaching or to account for energy that is reflected from the sample. And the power measured is higher than the power incident on the sample because there are optical components between the sample and the position where the power measurement is made.

Here is a representative calculation:

$$\text{measured power} \quad P_t \quad = \quad 10.8\mathrm{mW}/100$$

$$
\begin{aligned}
\text{laser repetition rate} \quad 1/f &= 12\text{ns} \\
\text{total pulse energy} \quad P_t/f &= \frac{10.8\text{mW}}{100} \times 12\text{ns} = 8.1 \times 10^6\text{eV} \\
\int d\omega \frac{L(\omega)}{\hbar\omega}(1 - e^{-\alpha(\omega)L}) &= 0.18151\text{eV}^{-1} \\
w_0 &= 26\mu \\
L &= 0.25\mu \\
\Rightarrow \quad N &= 2.4 \times 10^{15}\text{cm}^{-3}
\end{aligned}
$$

The factor of 100 comes from an nd2.0 filter which was not in place for the power measurement. The density is calculated for 1 pulse exciting the sample.

3.11 Data collection software

The lock-in amplifier, OMA and Klinger stepper-motor driver were all connected to a PC via a GPIB connection. The majority of the data was collected using software that we wrote in Visual Basic. There were two main programs, one which acquired data from the OMA and one which acquired data from the lock-in amplifier.

The program which controlled the OMA would read data into one memory of the OMA, download it into the PC and then display it on the computer screen. One scan could be read and saved as a scan of the dark current of the diode array and would then be subtracted from all the scans to correct for the dark current. The program was also capable of collecting an array of scans as the stepper motor was moved. This allowed us to measure the FWM-PS as a function of Δt. The program set the OMA to cool the detector array to 5°C and set the exposure time to 30μs. Some data was taken with the program WINSPEC supplied by Princeton Instruments.

The program which read the lock-in amplifier would scan through a range of stepper motor positions, waiting at each stepper motor position a specified amount of time and then reading the value measured by the lock-in. The starting and stopping stepper motor positions and the number of positions at which to take measurements were specified within the program using a setup menu. The program was capable of repeating a scan of the stepper motor positions a specified number of times and averaging. The lock-in parameters (sensitivity, time constants, etc.) were chosen from the front panel of the lock-in. The waiting time and number of scans were also specified from the setup menu. Some data was taken with an older program written in ASYST by Jean-Yves Bigot.

Chapter 4

Linear Measurements

4.1 Introduction

In this chapter, we briefly give the results of some linear measurements on the sample. These measurements characterize the sample, and give a good framework for evaluating the results of the nonlinear measurements.

4.2 Absorption spectra

Figure 4.1 shows a series of absorption measurements on the 0.25μm Sandia sample taken with σ^- polarization. We see the lh-X and hh-X below the band-edge and a series of higher-lying magneto-exciton states above the band edge. As mentioned in chapter 2, the strain in the sample splits the lh and hh bands at k=0 and results in the two distinct exciton species. The higher-lying magneto-excitons have Fano profiles due to coupling of the exciton to the lower lying Landau levels [25]. Only the lowest-lying excitons retain a Lorentzian profile. The linear and nonlinear optical properties of the higher-lying magneto-excitons

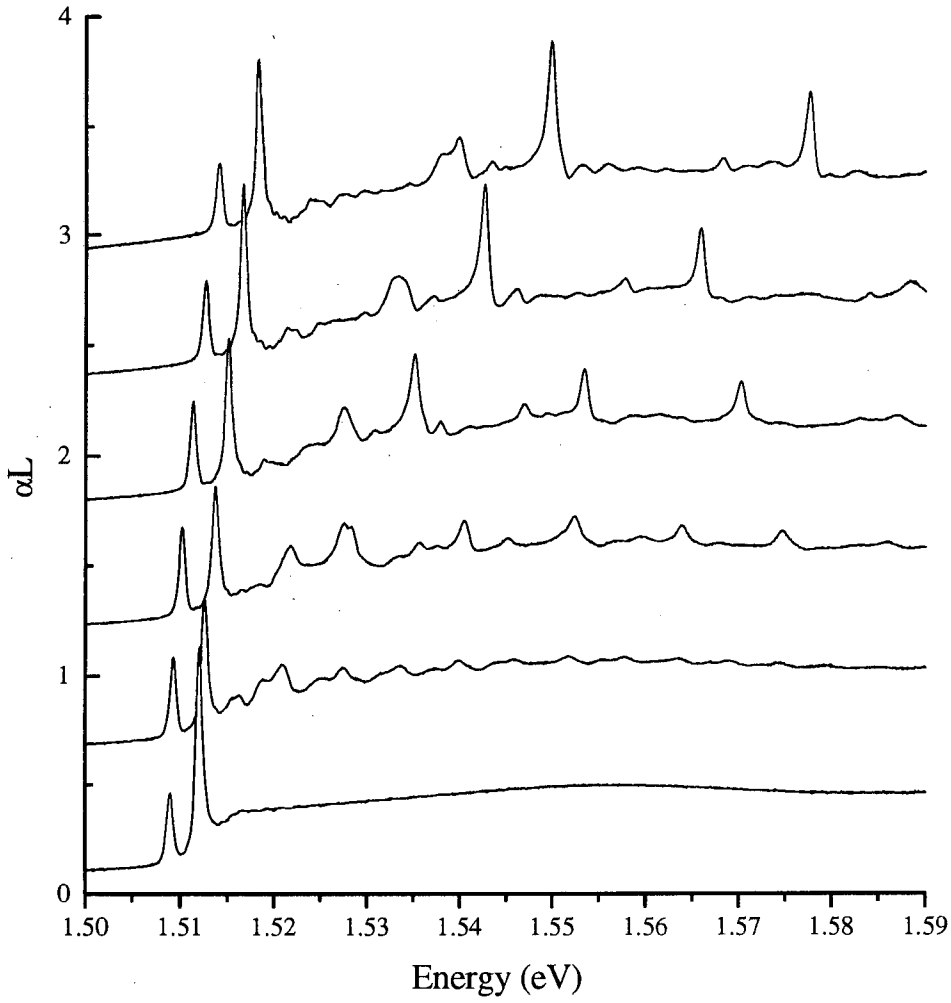

Figure 4.1: Light bulb absorption spectra of the 0.25 micron Sandia sample at 0, 2, 4, 6, 8, and 10 Tesla, from bottom to top.

have been studied elsewhere [72, 71, 11, 38]. Here only the Lorentzian magneto-excitons, the lh-X and hh-X, will be studied.

The positions, linewidths, and areas of the lh-X and hh-X are plotted in figure 4.2. These are the parameters used in the numerical simulations of the experiment. The positions of the lh-X and hh-X shift to higher energy with increasing magnetic field. But the changes in the linewidth and area of the resonances with magnetic field are not significant. This is in contrast to the common argument (as in [2]) that the oscillator strength of the exciton

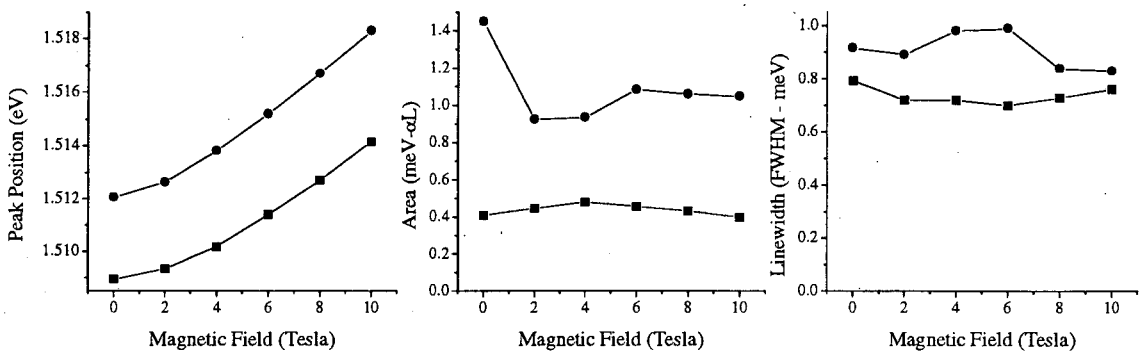

Figure 4.2: (a) Peak Positions (b) Areas and (c) Linewidths of the hh-X (circles) and lh-X (squares) vs. magnetic field

increases with magnetic field because the exciton wavefunction is squeezed by magnetic confinement. The increase in oscillator strength has been seen in microcavity structures [2] and InGaAs [59]. The most significant change is in the area of the hh-X as the field is increased from 0 to 2 Tesla. The large area of the hh-X at 0 Tesla is most likely due to overlap with the lh continuum. As the magnetic field is turned on, the overlap of the lh continuum with the hh-X diminishes and the hh-X area and linewidth decrease.

Although the light bulb measurements give a broad energy range, there are two difficulties with the above measurements. The light bulb illuminates the entire sample so that there is inhomogeneous broadening due to variations in the strain throughout the sample. The other difficulty is the resolution of the 0.25m spectrometer. We took a series of absorption measurements with the laser and the 0.75m spectrometer to compare with the measurements made with the light bulb.

Absorption measurements were taken with the laser at densities of $N \approx 6 \times 10^{15}\text{cm}^{-3}$ and $N/10 \approx 6 \times 10^{14}\text{cm}^{-3}$, considerably higher than the density excited by the light bulb. The density N corresponds to the density used for many of the FWM measurements, and these absorption measurements are shown in Fig. 4.3. No drastic changes

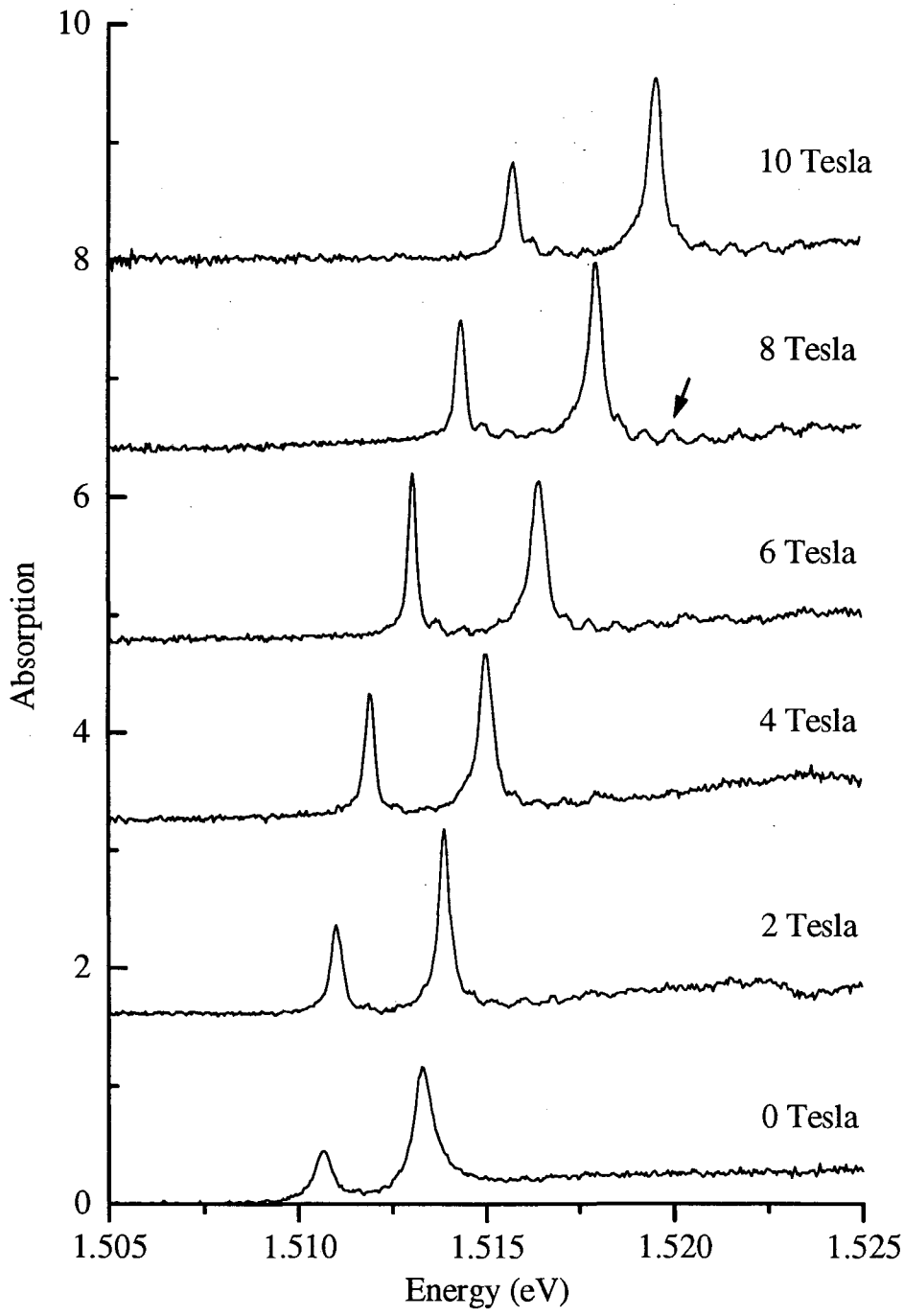

Figure 4.3: Absorption spectra taken with the laser at an excitation density of $\approx 6 \times 10^{15}\mathrm{cm}^{-3}$. The arrows points to one of the small peaks mentioned in the text.

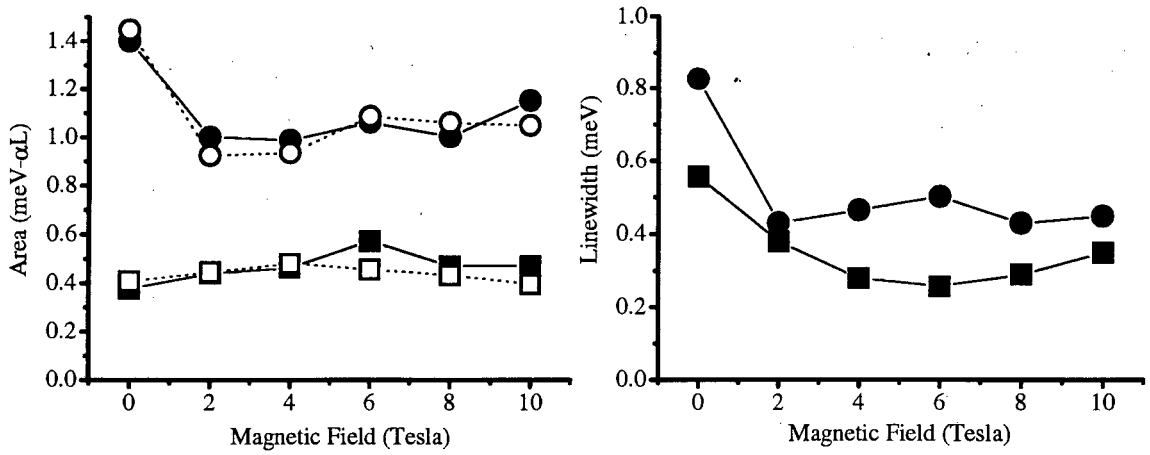

Figure 4.4: Laser measurements : (a) Areas and (b) Linewidths of the hh-X (circles) and lh-x (squares). The open symbols correspond to the lightbulb measurements.

occur in the absorption when going to densities lower than N. The results of the laser measurements are in good agreement with the light bulb measurements with regard to the changes in linewidth although the the linewidths measured with the laser are more than a factor of 2 narrower, and the change in the hh-X linewidth between 0 and 2 Tesla is evident. The oscillator strength measurements with the laser and lightbulb agree excellently. See Fig. 4.4. The linewidths from the linear spectra should correspond to the decay of the TI-FWM at the same excitation density. Thus, at a density of N, $2\gamma_{lh} = 0.35$meV and $2\gamma_{hh} = 0.45$meV, and the decay of the TI-FWM should be $T_2/2 = \frac{\hbar}{2\gamma} \approx 1.46$ps.

The other important difference revealed in measurements made with the new spectrometer is that a series of small peaks above the lh-X and hh-X appear in the absorption spectrum at high magnetic field. These peaks are due to the quantization of the center of mass motion of the excitons [57, 76]. The change in the structure of the continuum states makes these peaks more visible at high magnetic field. Using a simple particle in a box

model of the center of mass quantization [76], the peaks should appear at the energies

$$E_n = E_0 + n^2 \frac{\hbar^2 \pi^2}{2M_x L^{*2}} \tag{4.1}$$

where E_0 is the exciton energy, M_x is the total exciton mass and $L^* = L - 2a_0$ where L is the sample thickness. The peaks correspond to quantum numbers between $n = 6$ and $n = 20$ although it is not possible to definitely assign a quantum number to each peak.

4.3 Time-domain measurements

The linear transmission can also be measured in the time domain by upconverting the pulse transmitted through the sample as explained in chapter 3. This measurement indicates whether pulse propagation through the sample is important [1] and, thus, whether propagation effects must be included in the theoretical description of the experiment.

Figure 4.5 shows a series of time-resolved transmitted pulses for different magnetic field strengths. The transmitted pulse can be clearly seen followed by the free-induction decay of the polarization. The oscillations in the polarization result from the interference between the lh-X and hh-X emission. There is an increase in the strength of the free-induction decay as the magnetic field is increased. The decay time of the free-induction decay at 8 Tesla is 2.0ps, and at 10 Tesla it is 1.2ps in reasonable agreement with the frequency-domain results.

4.4 Conclusion

From the linear measurements we expect a decay of the FWM signal of $\approx$ 1.46ps, relatively independent of magnetic field. We also note that the oscillator strength of the

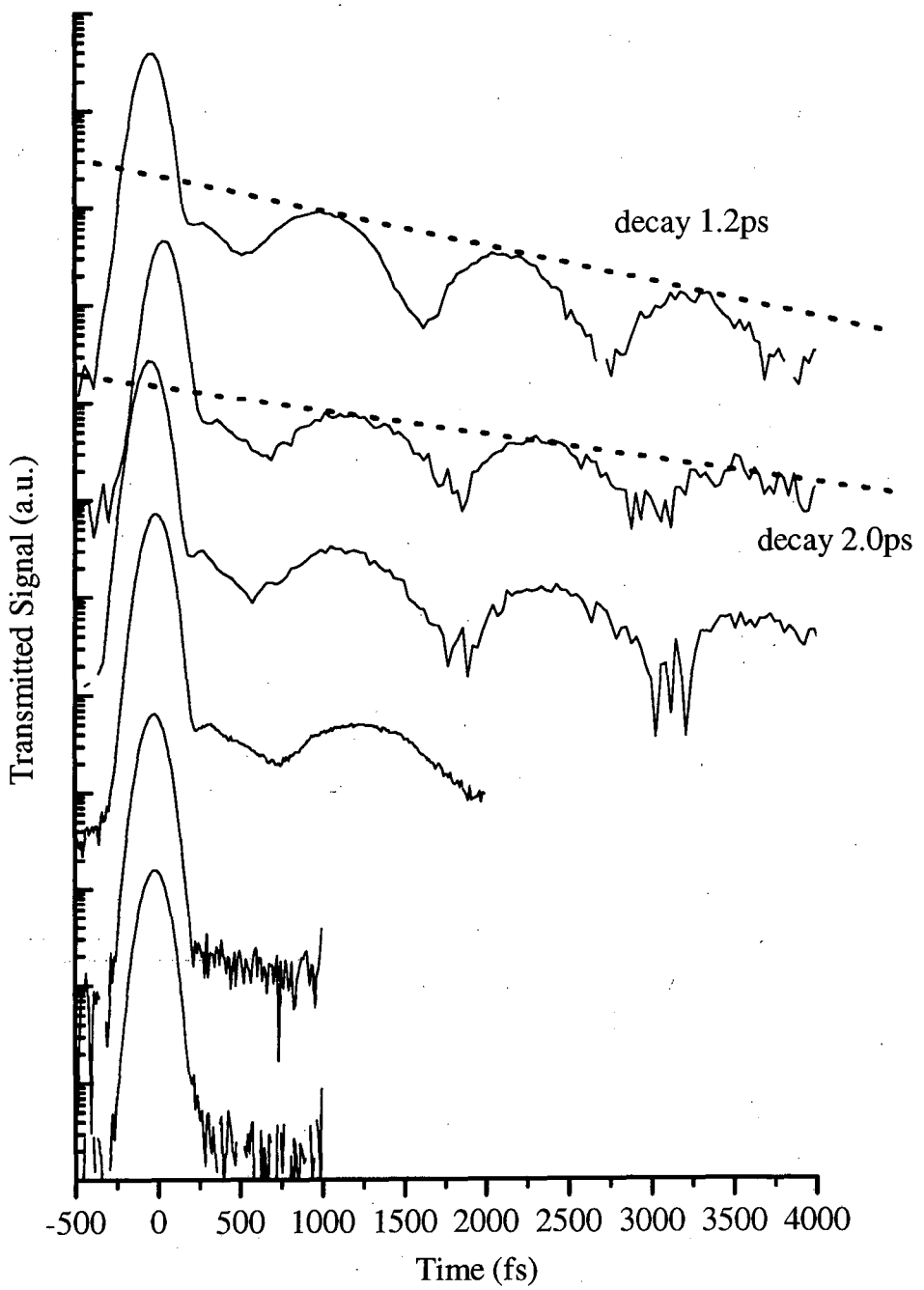

Figure 4.5: Time-resolved transmission for 0, 2, 4, 6, 8, and 10 Tesla. $N \approx 6 \times 10^{15}\text{cm}^{-3}$.

excitons does not change significantly with magnetic field, indicating that the exciton wavefunction does not change size. Upconversion of the transmitted pulse shows the pulse followed by the free induction decay of the polarization demonstrating that propagation effects can be neglected.

Chapter 5

Experimental Results

5.1 Introduction

In this chapter, we discuss the results of a series of FWM experiments done as a function of magnetic field. The results of these experiments indicate that at zero magnetic field, the behavior of excitons can be explained within the mean-field theory, the SBE, but that at high magnetic field, the experimental results are not consistent with the mean-field theory. A series of TI-FWM measurements are presented first. Then we show some FWM-PS measurements which support our interpretation of the TI-FWM results. Lastly we discuss TR-FWM data which provides some further information about our sample.

All the measurements in this chapter were made with resonant excitation of the excitons. As the magnetic field was increased, the excitonic lines shifted, and we tuned the laser so that the laser center frequency was always approximately between the lh-X and hh-X resonances. Figure 5.1 shows the laser spectrum superimposed on the absorption for B=0 Tesla.

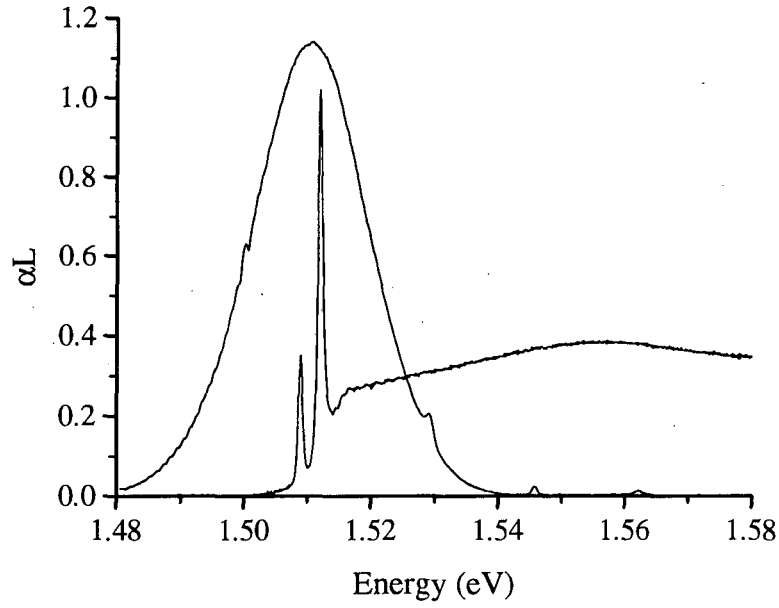

Figure 5.1: Laser and absorption spectra at 0 Tesla.

5.2 Time-integrated four-wave mixing

Figure 5.2 shows a series of TI-FWM measurements on the Sandia sample for different magnetic field strengths. The TI-FWM at B=0 Tesla has an exponential decay with oscillations for $\Delta t > 0$. The decay time, τ_d, is 1.48ps, in good agreement with the linewidths of the linear spectra taken with the laser at a comparable density. The oscillation period corresponds to the lh-X/hh-X energy splitting. For $\Delta t < 0$, there is a much smaller signal with a rise time, τ_r, of 0.25ps. This signal — which does not follow the rise of the laser pulse — is clear evidence of exciton-exciton interactions. There is also a large fast signal around $\Delta t = 0$, which is due to coherent excitation of the free carriers which dephase rapidly.

The decay of the signal for $\Delta t > 0$ gives the exciton dephasing time. The $\Delta t < 0$ signal is a result of the Coulomb interaction between the excitons. The fact that the rise

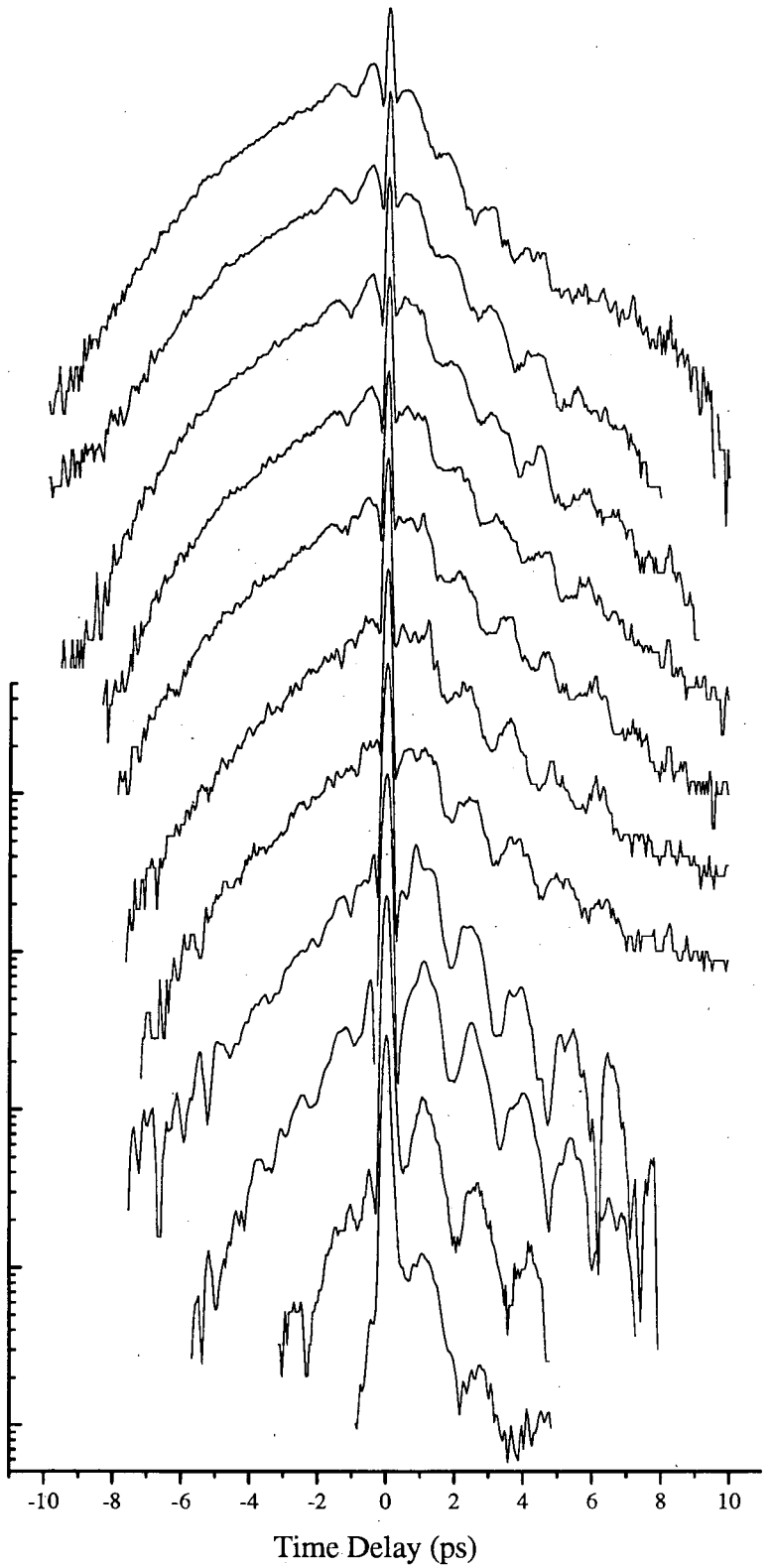

Figure 5.2: TI-FWM for the Sandia sample from 0 Tesla (bottom curve) to 10 Tesla (top curve) every 1 Tesla. The curves are displaced for clarity. The excitation density is $N \approx 5 \times 10^{15}\text{cm}^{-3}$.

time is not twice as fast as the decay time is most likely due to the influence of excited and continuum states with faster dephasing times. A small inhomogeneous broadening in the sample might also contribute to the faster rise time. The oscillations are quantum beats between the lh-X and the hh-X [40] which will be conclusively demonstrated with the FWM-PS and the TR-FWM data later in the paper.

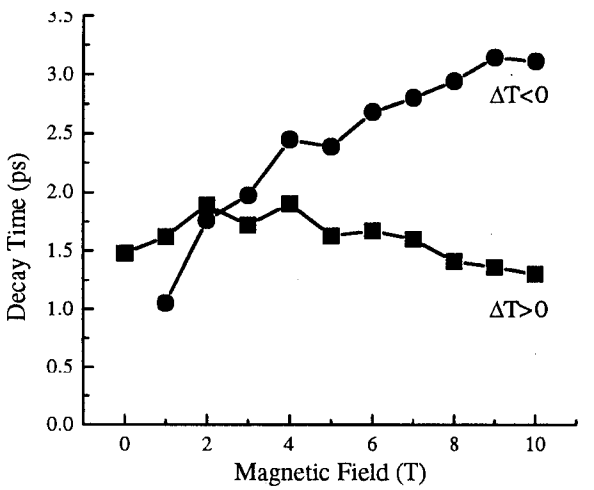

Figure 5.3: Rise and decay times of the TI-FWM shown in Fig. 5.2. The rise time is estimated from the signal near $\Delta t = 0$.

As the magnetic field is increased, the positive time signal, $S_{TI}^{+} \equiv S_{TI}(\Delta t > 0)$, changes only slightly: τ_d remains about 1.5ps while the signal magnitude increases slightly and the depth of the quantum beats diminishes. τ_d is determined by a fit of S_{TI}^{+} to $Ae^{-\Delta t/\tau_d}(1+C\cos(\omega\Delta t+\phi))$. The qualitative features of S_{TI}^{+} remain the same as the magnetic field is increased. The signal decays exponentially with oscillations at the frequency of the lh-X/hh-X energy splitting.

The negative time signal, $S_{TI}^{-} \equiv S_{TI}(\Delta t < 0)$, on the other hand, changes drastically as the magnetic field is increased. The magnitude of the signal changes by more than 2 orders of magnitude at $\Delta t = -500$fs. In contrast, at $\Delta t = 0$, the change is only about a factor of 4. τ_r goes from 0.25ps to 3.0ps. We have estimated τ_r with a simple exponential fit to the negative time signal for $-0.4 > \Delta t > -5$ps. Clearly, the rise of the signal is not a simple exponential, which suggests that non-Markovian processes are important. From the slow rise time of the TI-FWM ($\gg 1/4\gamma$), it is evident that, at high magnetic field, effects

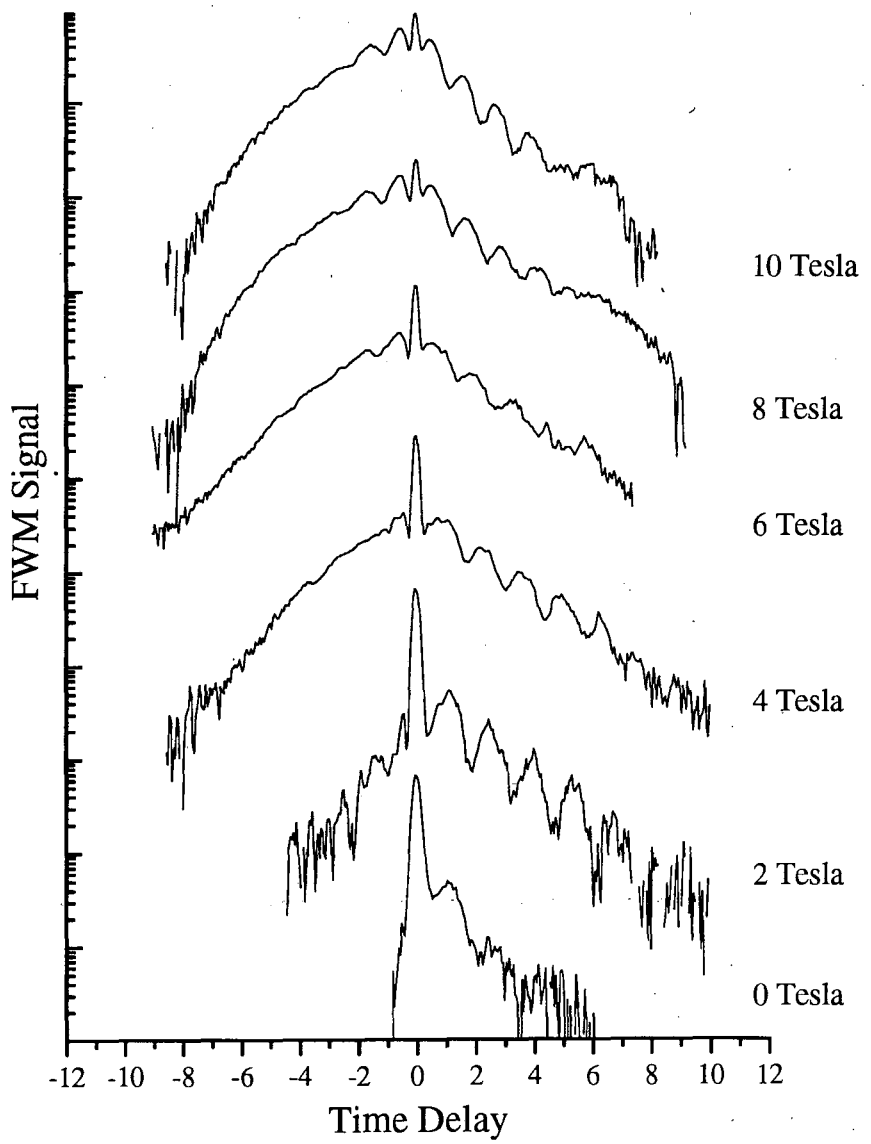

Figure 5.4: TI-FWM vs. B for the Bell Labs sample. $N \approx 10^{16}\text{cm}^{-3}$.

that are not included in the SBE become important. Fig. 5.3, a plot of τ_r and τ_d vs. B, shows that above about 4 Tesla, τ_r becomes greater than τ_d. It is interesting to compare this value with $B_c \approx 3.5$ Tesla.

Figure 5.4 shows the measurements from the Bell Labs 0.25 micron sample. We see exactly the same behavior on this sample as we do on the Sandia sample. The rise and decay times for the samples are quite similar — compare Fig. 5.3 and Fig. 5.5. This, and the narrow linewidths of both samples, indicate that both samples are high quality and that the effects we are measuring are intrinsic and not sample dependent. The differences in dephasing time between the two samples are partly due to different excitation density and partly due to the larger linewidth of the Bell Labs sample. At B=0T $2\gamma_{lh} = 0.58$meV and $2\gamma_{hh} = 0.53$meV calculated from the linear spectra of the Bell Labs sample. The excitation densities for the measurements on the Bell Labs sample are roughly 1.6 times higher than for the Sandia sample.

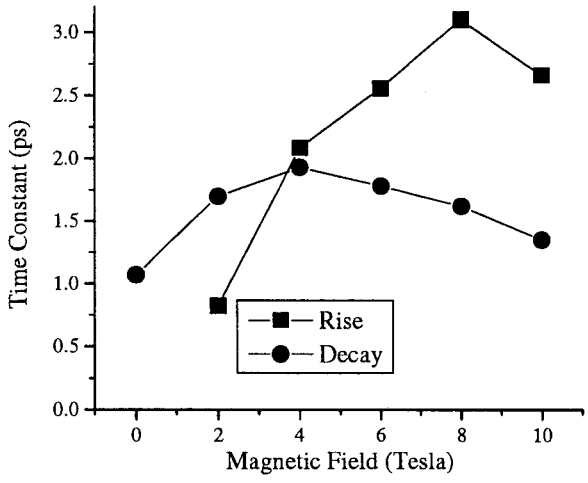

Figure 5.5: Rise and decay times for the TI-FWM of Fig. 5.4

We have calculated the density of excited excitons and excited free carriers from the measured laser spectra and the measured absorption spectra. The calculated densities for the Sandia sample are shown in figure 5.6. Due to the change in the continuum absorption, the number of free carriers excited decreases as the magnetic field is increased although the laser is tuned to keep the number of excitons excited roughly constant. Thus, at high magnetic

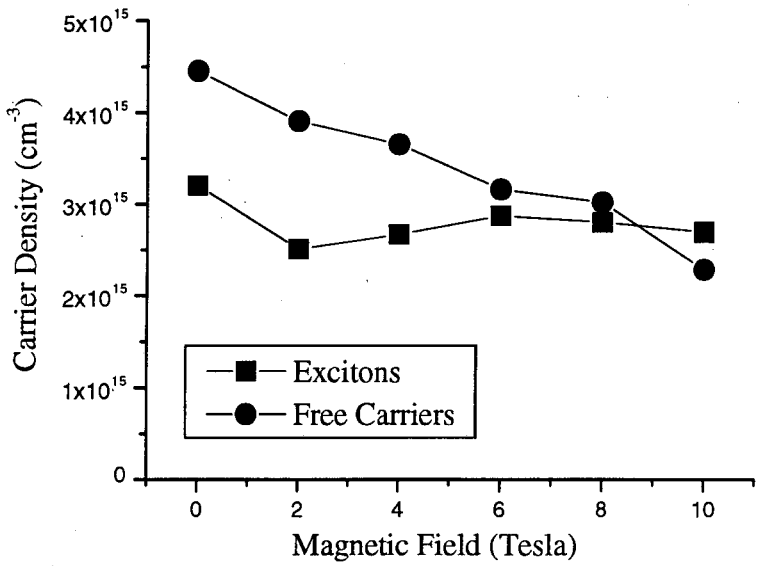

Figure 5.6: Exciton and free carrier density vs. B for the Sandia sample.

fields there are fewer free carriers available to screen the Coulomb interaction and the interactions between the excitons are stronger. This agrees with the experimental result that S_{TI}^{-}, which must be due to interactions, grows with B. But the increase in the strength of the Coulomb interaction most likely cannot fully explain the change in S_{TI}^{-} with B because S_{TI}^{-} does not simply grow with B but also changes qualitatively.

5.3 Four-wave mixing power spectra

The SBE predict that the lh-X signal is smaller than the hh-X signal because of the smaller oscillator strength of the lh-X. If we look at the FWM-PS at $\Delta t = 0$ as a function of magnetic field, Fig. 5.7, we also see the transition from a regime at low magnetic field, consistent with the mean-field theory, where the lh-X signal is about a factor of 3.5 smaller than the hh-X signal to a regime at high magnetic field, inconsistent with the mean-field theory, where the lh-X signal is stronger than the hh-X signal.

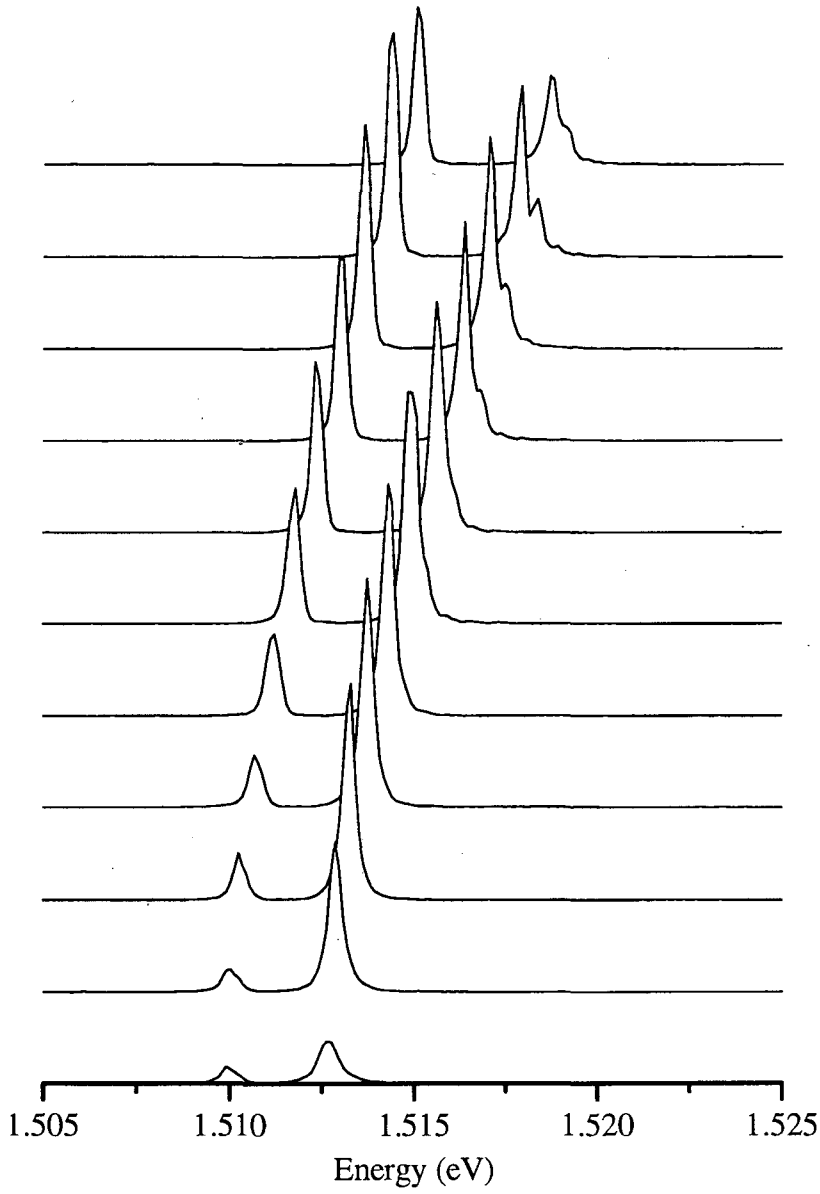

Figure 5.7: FWM-PS at $\Delta t = 0$ vs. B. These curves correspond to the TI-FWM in Fig. 5.2.

Within the SBE (Fig. 2.8) the beating between the lh-X and hh-X is polarization interference, but the oscillations in our data are quantum beats. The quantum beats can clearly be seen on the lh-X and hh-X emission peaks as a function of Δt in plots of the FWM-PS vs. Δt shown in Fig.5.8. As a last piece of spectrally resolved data, Fig. 5.9 shows a set of FWM-PS data at different time delays. From the data it is clear that the relative strength of the lh-X and hh-X signals changes as a function of Δt. This is further evidence of the strong interaction between the lh-X and hh-X which is beyond the mean-field predictions.

5.4 Time-resolved four-wave mixing

The emission of the TR-FWM as a free induction decay is also evidence of quantum beating. A few TR-FWM curves at different delays are shown in Fig. 5.10, and the arrival time of the TR-FWM vs. Δt is plotted in Fig. 5.11. For $\Delta t < 0$, the arrival time is a linear function of Δt with slope 1 indicating that the TR-FWM is emitted immediately after the second pulse as a free induction decay and not Δt later as a photon echo [1]. This demonstrates that the oscillations in the TR-FWM and TI-FWM are quantum beating [40], and, furthermore, this is proof that the sample is homogeneously broadened.

There are very pronounced beats in the TR-FWM in Fig. 5.10 for all Δt, consistent with the FWM-PS which shows two peaks, even though the S_{TI}^{-} is smooth. In fact the oscillations in the S_{TI}^{+} are also not very pronounced. In SBE calculations, there are pronounced beats in the TI-FWM corresponding to the beats in the TR-FWM. The delayed rise in the TR-FWM is due to interaction effects which have been explained within the framework of the SBE [83]. Figure 5.12 is a contour plot of the TR-FWM vs. Δt.

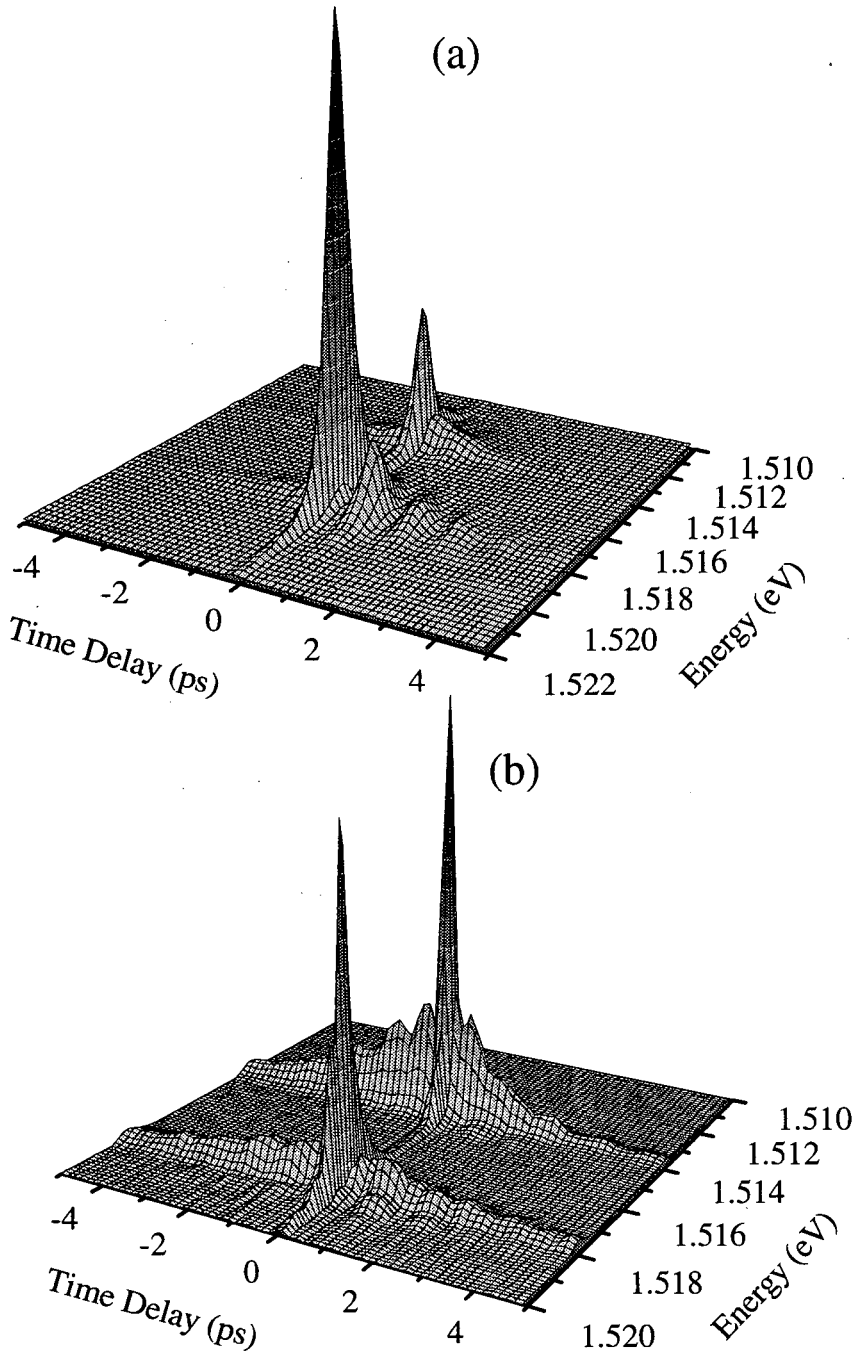

Figure 5.8: FWM-PS vs. Δt at 10 Tesla and (a) $5 \times 10^{16}\text{cm}^{-3}$ and (b) $3 \times 10^{15}\text{cm}^{-3}$.

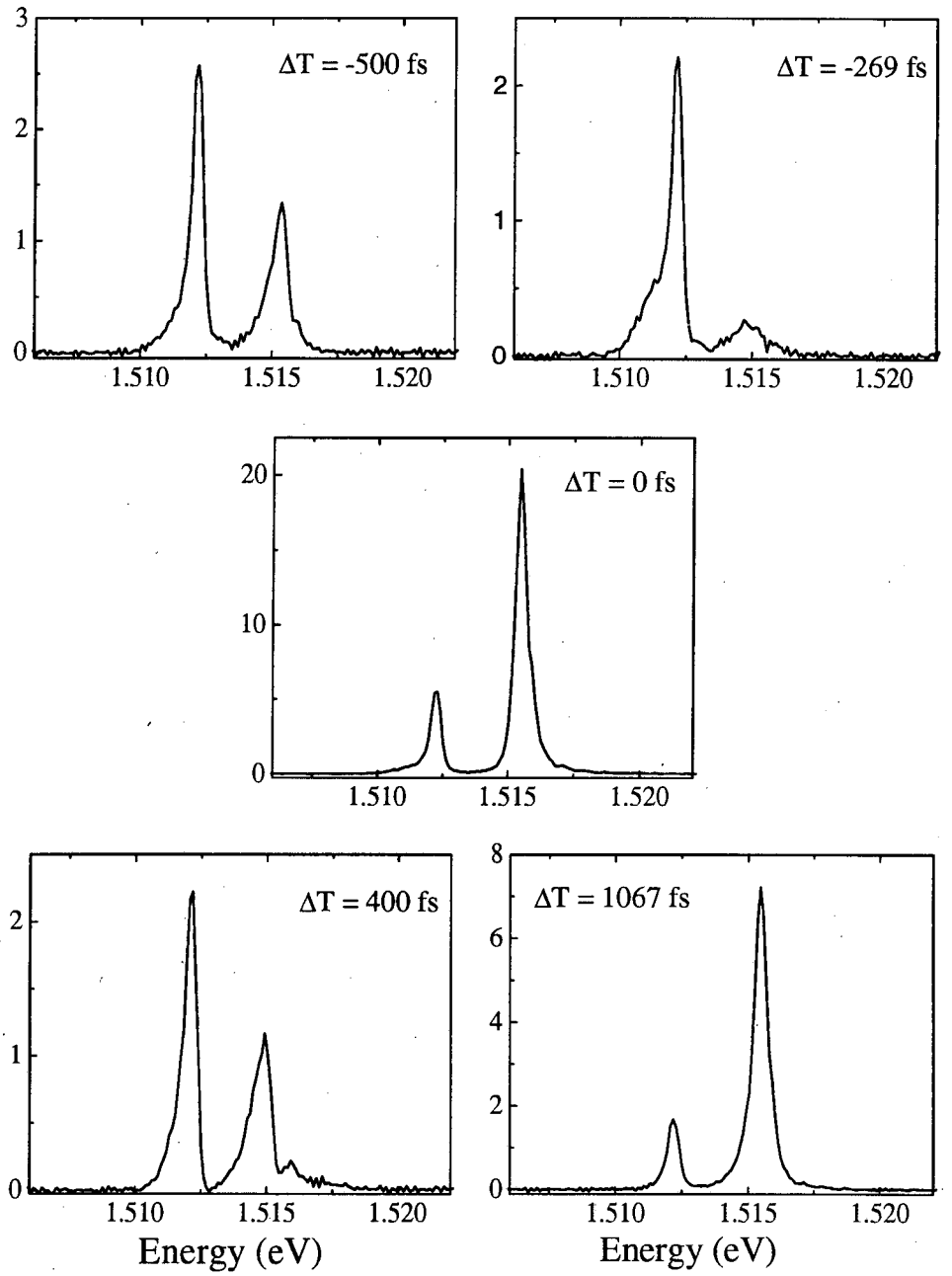

Figure 5.9: FWM-PS at different delays, showing an exchange of relative emission strength between the lh-X and hh-X. For these measurements, B=6T, $N \approx 5 \times 10^{15}\text{cm}^{-3}$ and $I_{k_2} \approx 4I_{k_1}$.

5.5 Conclusion

In this chapter we have described a series of TI-FWM and FWM-PS measurements taken at magnetic fields between 0 and 10 Tesla. These measurements are consistent with the mean-field theory at 0 Tesla, but at 10 Tesla, they show a number of discrepancies with the SBE calculations. The discrepancies are

- the large signal for $\Delta t < 0$;
- $\tau_r \gg \tau_d$;
- the comparable strength of the lh-X and hh-X signals at $\Delta t = 0$;
- the quantum beating;
- and the exchange of relative oscillator strength between the lh-X and hh-X.

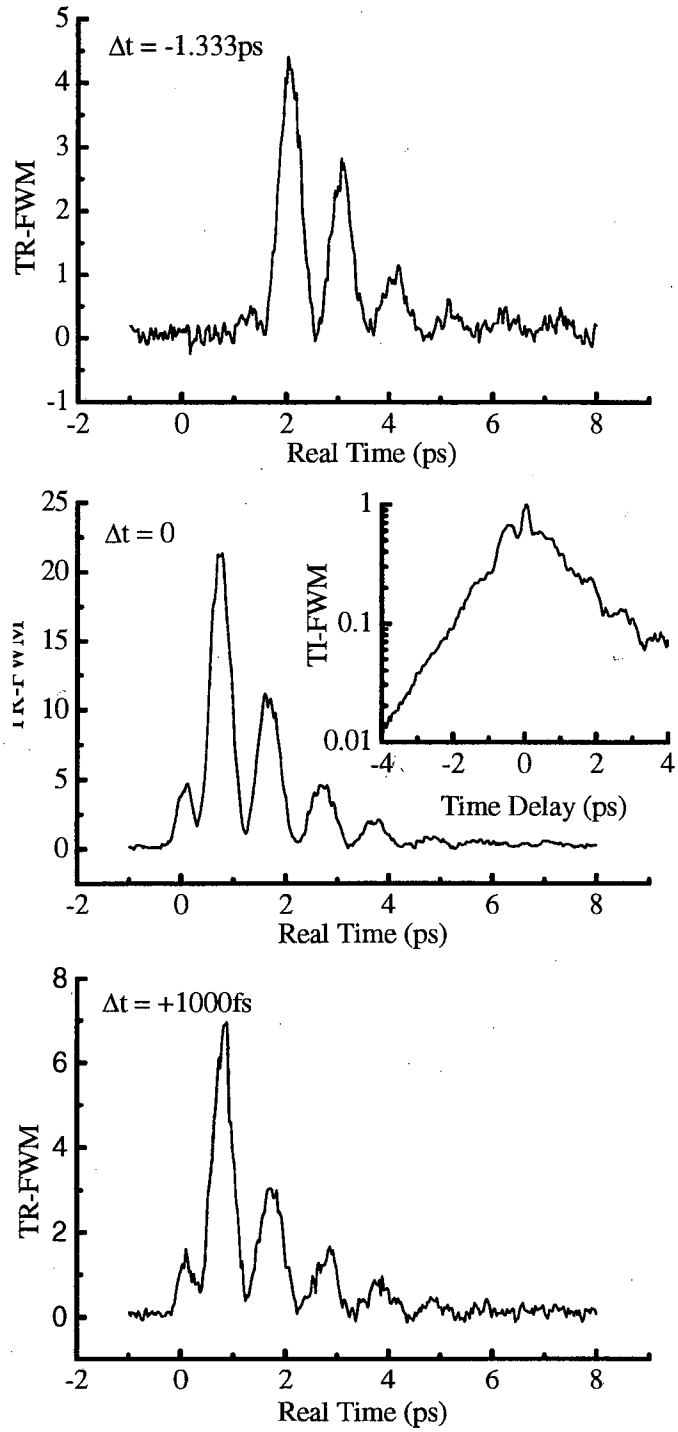

Figure 5.10: TR-FWM for a few Δt at 10 Tesla. Inset: TI-FWM. For these measurements $N \approx 10^{16}\text{cm}^{-3}$ and $I_{k_2} \approx 4I_{k_1}$.

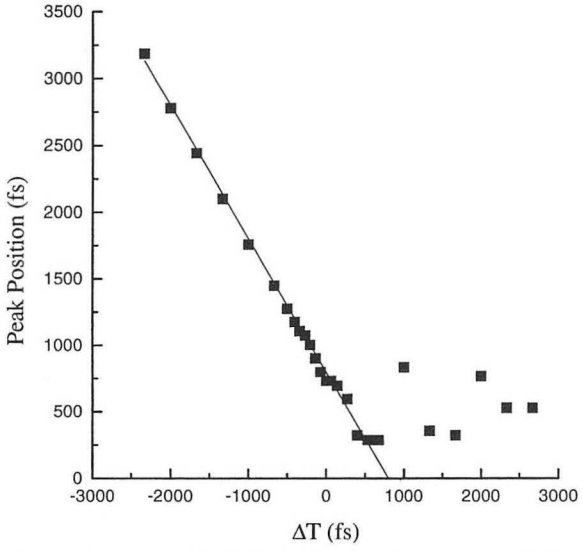

Figure 5.11: Time of maximum of TR-FWM vs. Δt. The solid line has a slope of 1.

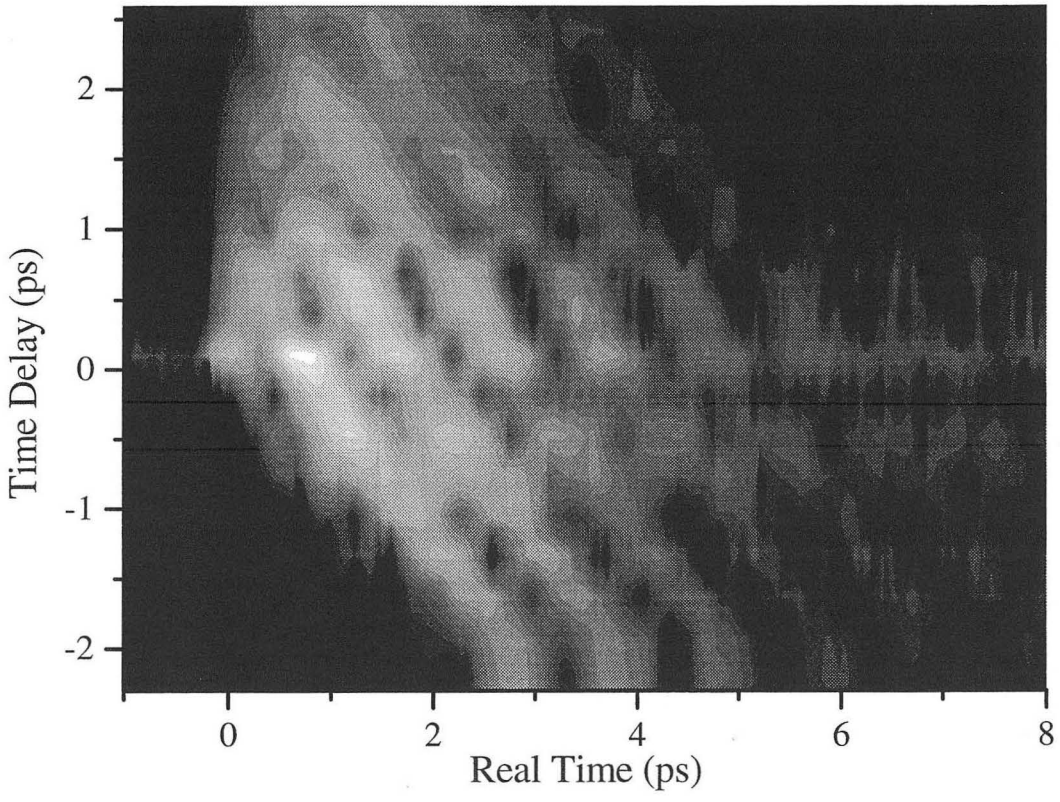

Figure 5.12: Contour plot of TR-FWM. Lighter indicates stronger signal. On this plot, the emission of the TR-FWM following the second pulse, the beating and the delayed rise of the TR-FWM can all be seen. The Contour plot was made from 26 TR-FWM measurements between $\Delta t = -2.3$ps and $\Delta t = 2.6$ps. For these measurements $N \approx 10^{16}\text{cm}^{-3}$ and $I_{k_2} \approx 4I_{k_1}$.

Chapter 6

Theory

6.1 Introduction

In the last chapter, we discussed the results of several FWM measurements. Many features of these results cannot be explained by the SBE: the shape of S_{TI}^{-}, the relative size of the lh-X and hh-X signals, the quantum beats and the exchange of oscillator strength between the lh-X and hh-X with Δt at high magnetic field. To explain these results we need to go beyond mean-field theory and include higher-order correlations than the 2-particle correlations included in the SBE. In particular, because the SBE always predict that the rise of S_{TI}^{-} is twice as fast as the decay of S_{TI}^{+}, a modification or improvement to the theory within the SBE will not explain the results. To go beyond the mean-field theory in a systematic way, we employ the Dynamics Controlled Truncation Scheme (DCTS) [6, 78]. The application of the DCTS to our problem is due to Wilfried Schäfer [37, 50, 62].

Using the DCTS, we show that the large S_{TI}^{-} seen experimentally at high magnetic field is due to exciton-exciton — 4-particle — correlations in the continuum of unbound

biexciton states.

6.2 The Dynamics Controlled Truncation Scheme

In the DCTS, the optical response of the semiconductor is calculated to a given order in the electric field, keeping all relevant correlations of electrons and holes, i.e. without making the Hartree-Fock approximation. This is possible because, in intrinsic semiconductors, each *e-h* pair is created by a photon so that successively higher-order correlations are proportional to higher orders in the electric field, allowing higher-order correlations to be ignored.

Calculating the optical response starts with the Hamiltonian, eqn. 2.14, and the calculation of the polarization which is given by the equation of motion for the 2-particle correlations, eqn. 2.19. The 2-particle correlations are driven by the electric field, 2-particle and 4-particle correlations. In the mean field theory, the 4-particle correlations are factorized into products of 2-particle correlations so that a closed set of equations at the level of 2-particle correlations can be written down.

In the DCTS, the 4-particle correlations are not factorized, and the equations of motion for the 4-particle correlations is written down. The 4-particle correlations are driven by 6-particle correlations and so the equation of motion for the 6-particle correlations should be written down and so on. The DCTS consists of a series of mathematical results which show that higher-order correlations are proportional to higher powers of the electric field and can, thus, be neglected for a calculation of the optical response to a given order in the electric field. The assumption behind this formalism is that the optical response can be expanded in powers of the electric field and that the higher-order terms in the expansion

become successively weaker.

The result of the DCTS is a finite set of equations of motion for the different relevant correlations. Each correlation is driven by a set of terms involving the applied optical electric field and the Coulomb interaction. While the DCTS is an essentially mathematical result for keeping track of the errors in a set of approximations, each correlation has a physical interpretation and the resulting set of equations can be interpreted reasonably straightforwardly. Some of the 2 and 4-particle correlations are given below. $\hat{e}_k^\dagger$ and $\hat{e}_k'^\dagger$ refer to different conduction bands.

$$P_k^{eh} \equiv \langle \hat{e}_k^\dagger \hat{h}_{-k}^\dagger \rangle = \text{Exciton creation} \tag{6.1}$$

$$f_k^{ee} \equiv \langle \hat{e}_k^\dagger \hat{e}_k \rangle = \text{Electron occupation} \tag{6.2}$$

$$f_k^{hh} \equiv \langle \hat{h}_k^\dagger \hat{h}_k \rangle = \text{Hole occupation} \tag{6.3}$$

$$\langle \hat{e}_{k_1}^\dagger \hat{e}_{k_2} \hat{h}_{k_3} \hat{e}_{k_4} \rangle = \text{Electron-screened exciton destruction} \tag{6.4}$$

$$\langle \hat{e}_{k_1}^\dagger \hat{e}_{k_2}^\dagger \hat{e}_{k_3} \hat{e}_{k_4} \rangle = \text{Conduction band density-density correlation} \tag{6.5}$$

$$\langle \hat{e}_{k_1}^\dagger \hat{h}_{k_2}^\dagger \hat{h}_{k_3} \hat{e}_{k_4} \rangle = \text{Exciton occupation} \tag{6.6}$$

$$\mathsf{B}_{k_1 k_2 k_3 k_4}^{ehe'h'} \equiv \langle \hat{e}_{k_1}^\dagger \hat{h}_{k_2}^\dagger \hat{e}_{k_3}'^\dagger \hat{h}_{k_4}'^\dagger \rangle = \text{Biexciton creation} \tag{6.7}$$

The homogeneous equation of motion for P_k^{eh} gives the excitonic structure, and the homogeneous equation of motion for $\mathsf{B}_{k_1 k_2 k_3 k_4}^{ehe'h'}$ gives the biexcitonic structure — both bound and unbound states. Because of the factorization, biexcitonic effects are not included in the SBE.

The main result of the DCTS is the truncation theorem, given in references [4], [6] and [78]: Theorem: Let $\hat{A}_n(m, n_g, n_u)$ be an n-particle operator in normal order according to the electron hole representation. Let n_c (n_d) denote the number of electron (hole) operators

contained in $\hat{A}_n$ such that $n = n_c + n_d$. $m \equiv \max\{n_c, n_d\}$; n_g is the number of effectively annihilated pairs in the n-particle operator (n_g is negative if pairs are created); and n_u is the number of unpaired particles which, by its sign, expresses the particle type. Consider now a semiconductor which is initially in the ground state consisting of filled valence bands and empty conduction bands. Then it follows for the expectation value of $\hat{A}_n(m, n_g, n_u)$:

$$\langle \hat{A}_n(m, n_g, n_u) \rangle = O(E^m) \quad \text{where } E \text{ is the electric field} \tag{6.8}$$

The electrodynamic response theorem [78] follows directly: A $\chi^{(n)}$ calculation of the electromagnetic response to an optical field only requires the evaluation of the particle operators $\hat{A}_s(m, n_g, n_u)$ where $m + \max\{|n_g| - 1, 0\} \leq n$.

There are two other useful theorems which comprise the DCTS: The contraction and factorization theorems. We only give a few relevant applications of these theorems. For the theorems in their most general form, we refer the reader to refs. [77] and [78]. The contraction theorem relates an n-particle correlation to a sum over (n+2)-particle correlations:

$$\langle \hat{e}^{c\dagger}_k \hat{e}^c_k \rangle = \sum_v \langle \hat{e}^{c\dagger}_k \hat{h}^{v\dagger}_{-k} \hat{h}^v_{-k} \hat{e}^c_k \rangle + O(E^4) \tag{6.9}$$

$$\langle \hat{e}^\dagger_{k+q} \hat{h}^\dagger_{-k} \hat{e}^{c\dagger}_{k'} \hat{e}^c_{k'+q} \rangle = \sum_{k''v} \langle \hat{e}^\dagger_{k+q} \hat{h}^\dagger_{-k} \hat{e}^{c\dagger}_{k'} \hat{h}^{v\dagger}_{k''} \hat{h}^v_{k''} \hat{e}^c_{k'+q} \rangle + O(E^5) \tag{6.10}$$

(The superscripts on the operators are band indices.) The factorization theorem specifies the error in powers of the electric field incurred by factorizing an n-particle correlation:

$$\langle \hat{e}^{c\dagger}_k \hat{h}^{v\dagger}_{-k} \hat{h}^v_{-k} \hat{e}^c_k \rangle = \langle \hat{e}^{c\dagger}_k \hat{h}^{v\dagger}_{-k} \rangle \langle \hat{h}^v_{-k} \hat{e}^c_k \rangle + O(E^4) \tag{6.11}$$

$$\langle \hat{e}^\dagger_{k+q} \hat{h}^\dagger_{-k} \hat{e}^{c\dagger}_{k'} \hat{h}^{v\dagger}_{k''} \hat{h}^v_{k''} \hat{e}^c_{k'+q} \rangle = \langle \hat{e}^\dagger_{k+q} \hat{h}^\dagger_{-k} \hat{e}^{c\dagger}_{k'} \hat{h}^{v\dagger}_{k''} \rangle \langle \hat{h}^v_{k''} \hat{e}^c_{k'+q} \rangle + O(E^5) \tag{6.12}$$

These two theorems are only strictly valid in the coherent limit, i.e. when the dephasing can be ignored. This would be the case for an ideal system of electrons and holes interacting with

a coherent light pulse. In real systems, there are impurities and lattice defects and phonons which contribute to the dephasing of the *e-h* system. We will account for dephasing using phenomenological parameters which lead to the decay of the polarization-like quantities.

The DCTS has been successfully applied to FWM, pump-probe and terahertz spectroscopy experiments that cannot be explained by the SBE [5, 7, 12, 64]. In FWM experiments, DCTS can explain the change in signal magnitude with relative polarization angle (for linear polarization), and bound biexcitonic effects, in contrast to the SBE in the relaxation time approximation. DCTS should be contrasted with phenomenological theories [16] which can explain some polarization dependence and multilevel system approaches for including bound biexciton effects [9, 54] which cannot be derived rigorously from the semiconductor Hamiltonian.

6.3 The $\chi^{(3)}$ Truncation Scheme

To calculate the FWM response, we employ the DCTS to 3rd order in E in the coherent limit. The truncation theorem tells us that the highest order correlation we will need to include in the theory is $\langle \hat{e}^{\dagger}_{k_1} \hat{h}^{\dagger}_{k_2} \hat{e}'^{\dagger}_{k_3} \hat{h}'^{\dagger}_{k_4} \hat{e}''^{\dagger}_{k_5} \hat{h}''^{\dagger}_{k_6} \rangle$. In the coherent limit, we make use of the contraction and factorization theorems to make substitutions for the 4-particle correlations, allowing us to reduce the number of correlations that we need to include.

$$\langle \hat{e}^{\dagger}_{k+q} \hat{h}^{\dagger}_{-k} \hat{e}^{c\dagger}_{k'} \hat{e}^{c}_{k'+q} \rangle = \sum_{k''v} \langle \hat{e}^{\dagger}_{k+q} \hat{h}^{\dagger}_{-k} \hat{e}^{c\dagger}_{k'} \hat{h}^{v\dagger}_{k''} \rangle \langle \hat{h}^{v}_{k''} \hat{e}^{c}_{k'+q} \rangle + O(E^5) \tag{6.13}$$

It follows that only two quantities are needed to calculate the FWM response: the 2-particle correlation P_k and the 4-particle correlation $B^{ehe'h'}_{k_1k_2k_3k_4}$. Here we define $B^{ehe'h'}_{k_1k_2k_3k_4}$ somewhat

differently than before:

$$B^{ehe'h'}_{k_1k_2k_3k_4} = \langle \hat{e}^\dagger_{k_1} \hat{h}^\dagger_{k_2} \hat{e}'^\dagger_{k_3} \hat{h}'^\dagger_{k_4} \rangle - \langle \hat{e}^\dagger_{k_1} \hat{h}^\dagger_{k_2} \rangle \langle \hat{e}'^\dagger_{k_3} \hat{h}'^\dagger_{k_4} \rangle + \langle \hat{e}^\dagger_{k_1} \hat{h}'^\dagger_{k_4} \rangle \langle \hat{e}'^\dagger_{k_3} \hat{h}^\dagger_{k_2} \rangle \tag{6.14}$$

The equations of motion for P^{eh}_k and $B^{ehe'h'}_{k_1k_2k_3k_4}$ have the following structure:

$$\begin{aligned} \frac{\partial}{\partial t} P &= \mu^{eh} E + \text{PB terms} + \text{mean-field interaction} \\ &\quad + (P)^* B + O(E^4) \qquad (6.15) \\ \frac{\partial}{\partial t} B &= (P)^2 + O(E^6) \qquad (6.16) \end{aligned}$$

Note that the first line of eqn. 6.15 is equivalent to the mean-field theory. This is the advantage of defining $B^{ehe'h'}_{k_1k_2k_3k_4}$ as in eqn. 6.14. Thus we can interpret $B^{ehe'h'}_{k_1k_2k_3k_4}$ as representing deviations from the mean-field result. $B^{ehe'h'}_{k_1k_2k_3k_4}$ is the coherent part of the 4-particle correlation; for a pair of excitons that are not coherent with each other, $B^{ehe'h'}_{k_1k_2k_3k_4}$=0. The full equations are given in the next section.

6.4 Results for GaAs in a magnetic field

In a high magnetic field, the semiconductor Hamiltonian, eqn. 2.14, is modified in the following way. Because we are considering excitation at the band edge in a high magnetic field, we include only the lowest Landau level. Thus, the single particle energies become

$$\epsilon^{e,h}_k = \epsilon^{e,h}_0 + \frac{\hbar^2}{2m_{e,h} l^2} + \frac{\hbar^2 k^2}{2m_{e,h}} \tag{6.17}$$

where l is the magnetic length, $l = \sqrt{\hbar/eB}$. Each particle is now indexed by a 1-dimensional momentum, k, along the direction $\parallel \vec{B}$ and a 2-dimensional vector, $\vec{\eta} = (\eta, \phi)$ in the plane

$\perp \vec{B}$. The Coulomb matrix element is now

$$\nu_k^{\eta,\eta'} = \frac{e^2}{\epsilon_0 L^2} \frac{e^{-l^2\eta^2/2}}{\eta^2 + k^2} e^{il^2\vec{\eta}\times\vec{\eta}'} \tag{6.18}$$

To calculate the FWM signal, the equations of motion for P_k^{eh} and $B_{k_1k_2k_3k_4}^{ehe'h'}$ are projected onto the basis of magneto-exciton eigenfunctions with vanishing center of mass motion. The equations for P_k^{eh} and $B_{k_1k_2k_3k_4}^{ehe'h'}$ are given in an appendix to this chapter. To find the eigenfunctions, $\phi_{n,0}^{eh}(k)$, the homogeneous part of eqn. 6.30 is solved with the substitution

$$P_k^{eh} = \sum_n P_n^{eh} \phi_{n,0}^{eh}(k) \tag{6.19}$$

The equations of motion in the exciton basis are [50]

$$\begin{aligned}
&(-i\hbar\frac{\partial}{\partial t} - \gamma_P - \epsilon_n^{eh})P_n^{eh} = E\mu^{eh}\phi_n^{eh}(r=0) \\
&+ \sum_{e'h'ml} E\left[\mu^{e'h'} b_{nml}^{eh'e'h'} P_m^{eh'} + \mu^{eh'} b_{nml}^{e'he'h'} P_m^{e'h}\right] P_l^{e'h'*} \\
&+ \sum_{e'h'jlm} V_{njlm}^{st} P_j^{eh'} P_l^{e'h'*} P_m^{e'h} \\
&+ \sum_{e'h'jnm,q\eta} P_j^{e'h'*} \left[\tilde{B}_{nm,q,\eta}^{eh'e'h} \nu_q^{\eta,0} M_{in,q,\eta}^{eh} M_{jm,-q,\eta}^{e'h'} + \tilde{\tilde{B}}_{nm,q,\eta}^{e'h'eh} V_{nmji,q,\eta}^{XC}\right]
\end{aligned} \tag{6.20}$$

and

$$\begin{aligned}
(-i\hbar\frac{\partial}{\partial t} - i\gamma_B - \epsilon_{nq}^{e'h} - \epsilon_{mq}^{eh'})\tilde{B}_{nm,q,\eta}^{eh'e'h} &= -\frac{L^2}{2\pi l^2}\nu_q^{\eta,0} \sum_{ij} M_{in,-q,\eta}^{eh} M_{jm,q,\eta}^{eh} P_i^{eh} P_j^{e'h'} \\
(-i\hbar\frac{\partial}{\partial t} - i\gamma_B - \epsilon_{nq}^{e'h} - \epsilon_{mq}^{eh'})\tilde{\tilde{B}}_{nm,q,\eta}^{eh'e'h} &= -\sum_{\eta'} \nu_q^{\eta',\eta} \sum_{ij} M_{in,-q,\eta}^{eh} M_{jm,q,\eta}^{eh} P_i^{eh} P_j^{e'h'}
\end{aligned} \tag{6.21}$$

$\tilde{B}$ and $\tilde{\tilde{B}}$ are components of B. Their definitions, along with definitions of the matrix elements, are given in the appendix. Because the Coulomb interaction terms are not included on the left of eqns. 6.21, only the unbound biexciton states are included which is consistent with the experimental polarization geometry in which no bound hh-X/hh-X and lh-X/lh-X biexcitons can be created.

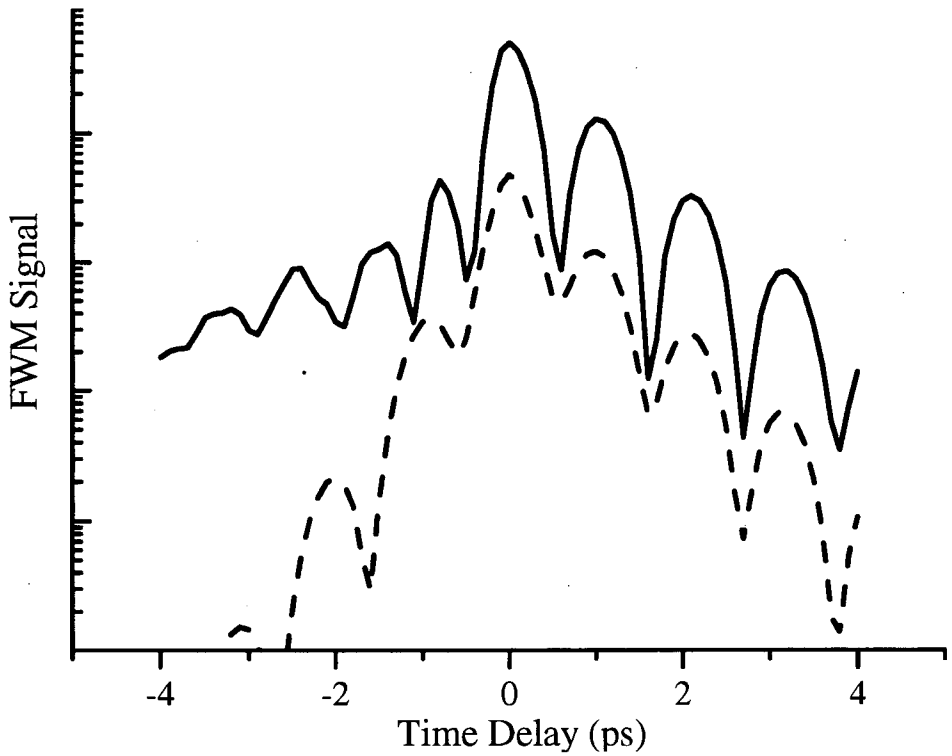

Figure 6.1: TI-FWM in a magnetic field calculated from the $\chi^{(3)}$ truncation scheme. The dashed curve is the calculation with $B^{ehe'h'}_{k_1k_2k_3k_4}$ set to 0 and is equivalent to the SBE.

Figure 6.1 shows the results of the calculation for the TI-FWM (solid curve). The results of the calculation without 4-particle correlation effects (setting B=0) are also shown for comparison (dashed curve). The theory correctly gives the slow rise time seen in the experimental data in contrast to the calculation without 4-particle correlations. The theoretical S^{-}_{TI} has pronounced oscillations that are not seen in the experimental data. We currently believe that these oscillations are smoothed out by exciton-exciton density correlations, $N^{e'h'eh}_{k_1k_2k_3k_4} = \langle \hat{e}'^{\dagger}_{k_1} \hat{h}'^{\dagger}_{k_2} \hat{e}_{k_3} \hat{h}_{k_4} \rangle - \langle \hat{e}'^{\dagger}_{k_1} \hat{h}'^{\dagger}_{k_2} \rangle \langle \hat{e}_{k_3} \hat{h}_{k_4} \rangle$, which contribute to the FWM beyond third order in the electric field. $N^{e'h'eh}_{k_1k_2k_3k_4}$ corresponds to fluctuations in the exciton density about the mean value.

The theory also agrees with the experiment with regard to the relative contributions of lh-X and the hh-X. This can be seen in the FWM-PS in Fig. 6.2 which shows the

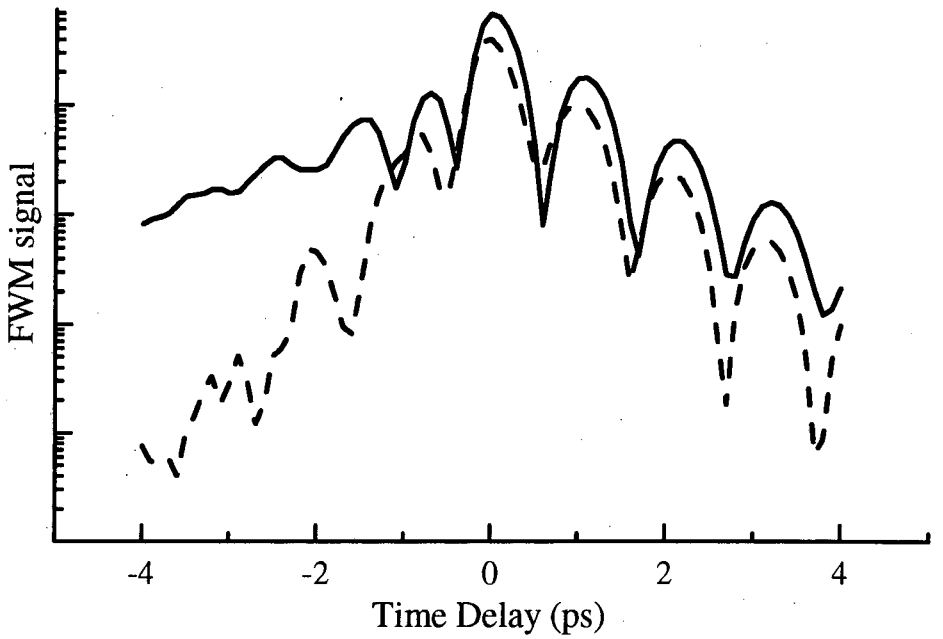

Figure 6.2: hh-X (solid) and lh-X (dashed) contributions to the FWM.

area in the lh-X and hh-X peaks as a function of time delay. In contrast to the SBE calculation, the lh-X and hh-X signals are the same order of magnitude and the quantum beats are clearly seen at both frequencies. The exchange of oscillator strength between the lh-X and the hh-X can be seen in Fig.6.2 but is more evident in Fig. 6.3 which shows a series of TR-FWM and FWM-PS for different Δt. We have calculated the TI-FWM for a few different magnetic field strengths as well, Fig. 6.4, showing the increase in S_{TI}^{-} with increasing magnetic field. For these calculations, the 4-particle correlation dephasing rate, $\gamma_B = 0$, and the rise time of the TI-FWM is determined by the memory kernel of the correlation function [37]. The rise time is finite due to the interference of the various contributions of the biexciton continuum.

The $\chi^{(3)}$ Truncation Scheme which includes exciton-exciton correlations correctly reproduces most of the important features of the experimental results which don't appear

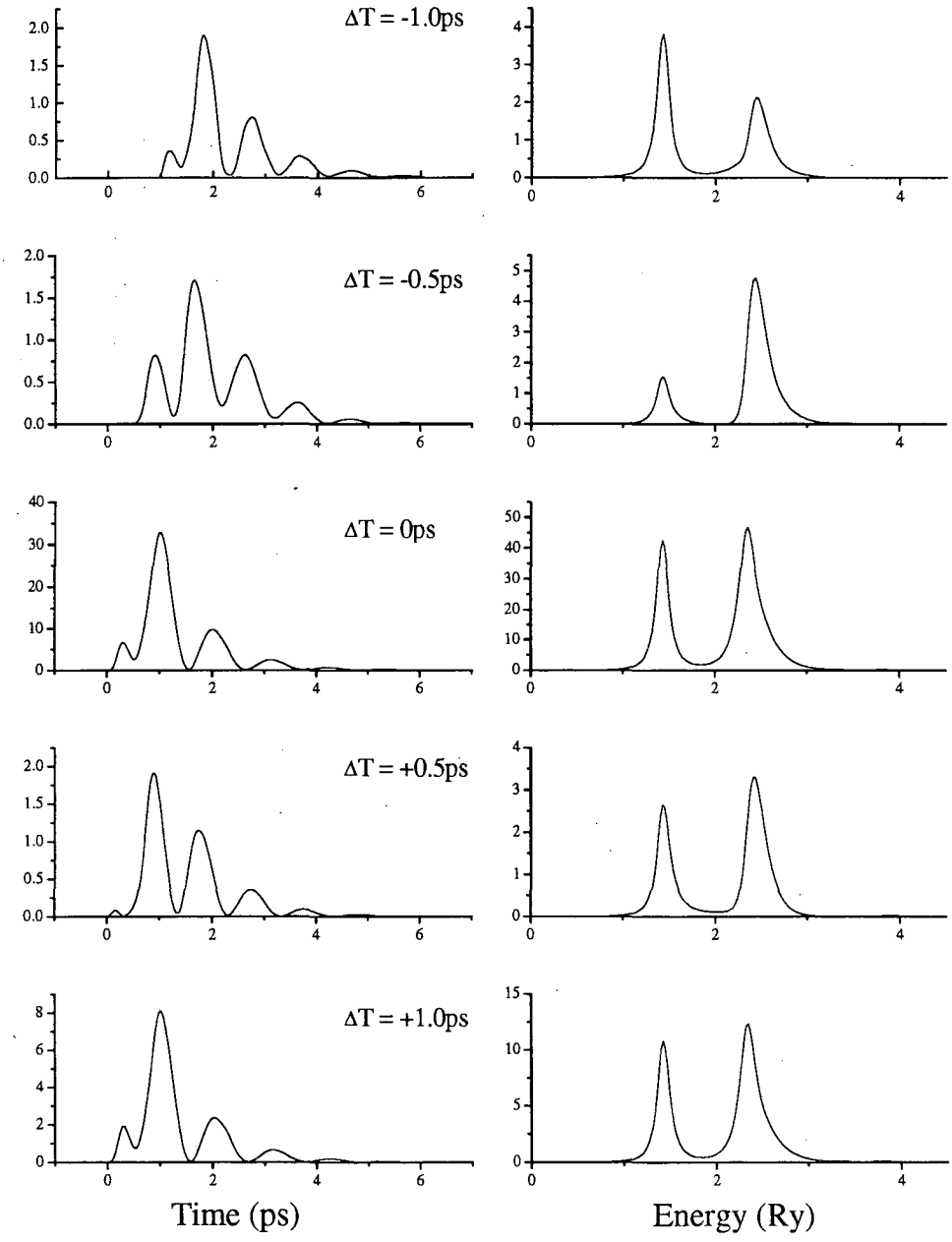

Figure 6.3: TR-FWM and FWM-PS calculated from the $\chi^{(3)}$ truncation scheme.

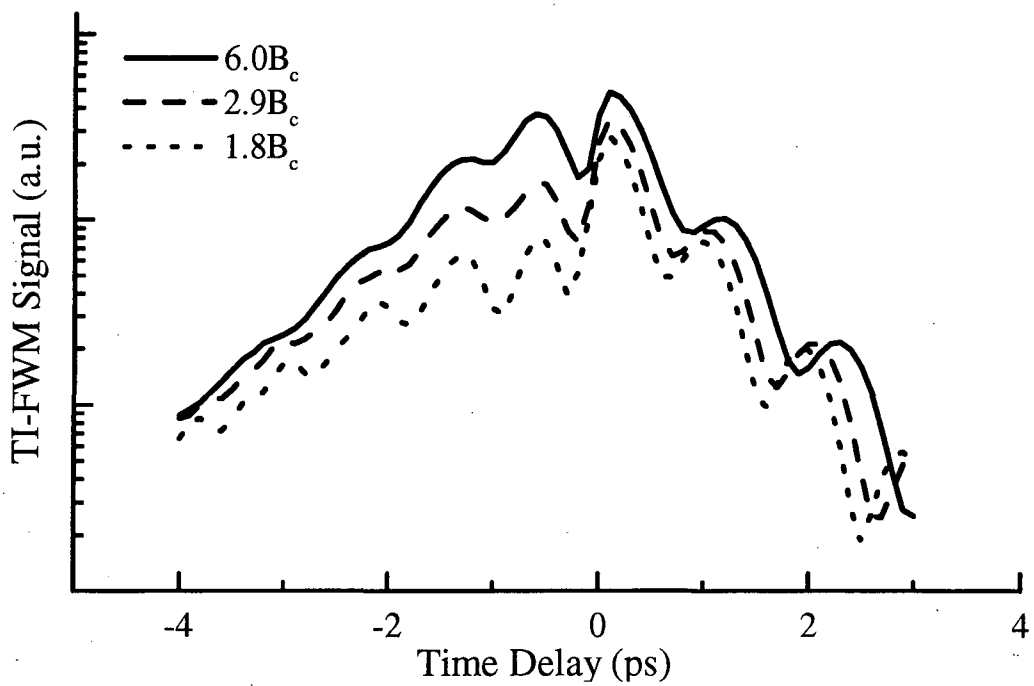

Figure 6.4: TI-FWM calculated for a few different magnetic field strengths from the $\chi^{(3)}$ truncation scheme.

in the SBE calculations. Unfortunately, the theory is quite complicated, and it is hard to develop an intuitive understanding of what is happening. In the next section we develop a simple model derived from the full theory.

6.5 The average polarization model

Equations 6.20 and 6.21 can be reduced to a one-dimensional model by averaging over the lowest excitonic contributions [36, 64]. The advantages of this model are that it captures the essential physics but is computationally much simpler and can be solved analytically in powers of the electric field for the case of delta-function excitation, providing more intuition into how the 4-particle correlations affect the FWM signal. The biexciton continuum is modelled as a single resonance at twice the exciton frequency. First we consider

the case of a single species of exciton:

$$\left[-i\frac{\partial}{\partial t} - i\gamma_P - \Omega_0\right] P(t) = -\mu \cdot \mathbf{E}\left(1 - \frac{|P(t)|^2}{P_s^2}\right) + \nu P(t)|P(t)|^2 + B(t)P(t)^* \tag{6.22}$$

$$\left[-i\frac{\partial}{\partial t} - i\gamma_B - 2\Omega_0\right] B(t) = aP(t)^2 \tag{6.23}$$

Equation 6.22 has the structure of a single resonance driven by four terms. The first term is simply the driving electric field and is responsible for the linear response of the polarization. The second term, $\propto E|P(t)|^2$, is the effect of Pauli blocking (PB) on the excitation. The third term comes from the Coulomb interaction between the excitons in the Hartree-Fock approximation. This term, referred to as the Bare Coulomb Interaction (BCI) term, is responsible for the $\Delta t < 0$ signal which has a rise time of $1/4\gamma_P$.

The last term in eqn. 6.22 is the contribution of 4-particle correlations to the polarization. Eqn. 6.23 is the equation of motion for B, the effective 4-particle correlation, and the parameter a is the strength of the exciton-exciton correlation (XXC), i.e. the coupling of B to P. Figure 6.5 shows the results of a calculation of the model with the parameters P_s, ν, and a chosen to reproduce the lineshape of the experimental curves (absent the quantum beats, of course). The three other curves are the contributions to the total signal from PB, BCI and XXC.

From Fig. 6.5 it is clear that the XXC contribution clearly dominates S_{TI}^-. The 4-particle correlation gives such a long negative time signal because B is the integral of the polarization, and, hence, has a memory of P. B can be viewed as a non-Markovian source for the polarization. It is interesting to note that all three contributions decay at the rate $2\gamma_P$ for S_{TI}^+. We cannot distinguish between PB, BCI and XXC in S_{TI}^+, but the decay of

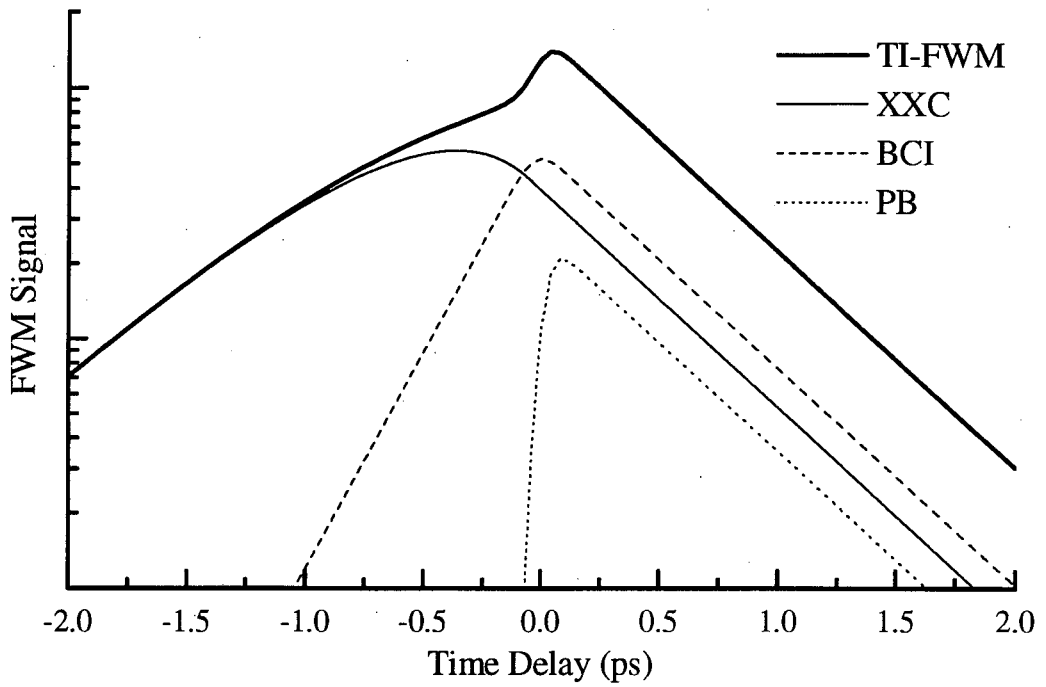

Figure 6.5: TI-FWM calculated from eqns. 6.22 and 6.23. $P_s = 1.12$, $\nu = .05$, $a = 10^{-4}$, $\gamma_P = 0.001\text{fs}^{-1}$ and $\gamma_B = 0.001\text{fs}^{-1}$.

S^+_{TI} unambiguously yields γ_P.

Extending the model to include both the lh-X and hh-X for σ^- excitation is straightforward.

$$\left[-i\frac{\partial}{\partial t} - i\gamma_P - \Omega_{hh}\right] P^a(t) = -\mu_{\mathbf{hh}} \cdot \mathbf{E}\left(1 - \frac{|P^a(t)|^2}{P_s^2}\right) + \nu P^a(t)|P^a(t)|^2 + P^a(t)^* B^{aa}(t) + P^b(t)^* B^{ab}(t) \tag{6.24}$$

$$\left[-i\frac{\partial}{\partial t} - i\gamma_P - \Omega_{lh}\right] P^b(t) = -\mu_{\mathbf{lh}} \cdot \mathbf{E}\left(1 - \frac{|P^b(t)|^2}{P_s^2}\right) + \nu P^b(t)|P^b(t)|^2 + P^b(t)^* B^{bb}(t) + P^a(t)^* B^{ab}(t) \tag{6.25}$$

and

$$\left[-i\frac{\partial}{\partial t} - i\gamma_B - 2\Omega_{hh}\right] B^{aa}(t) = V_{aa} P^a(t)^2 \tag{6.26}$$

$$\left[-i\frac{\partial}{\partial t} - i\gamma_B - 2\Omega_{lh}\right] B^{bb}(t) = V_{bb} P^b(t)^2 \tag{6.27}$$

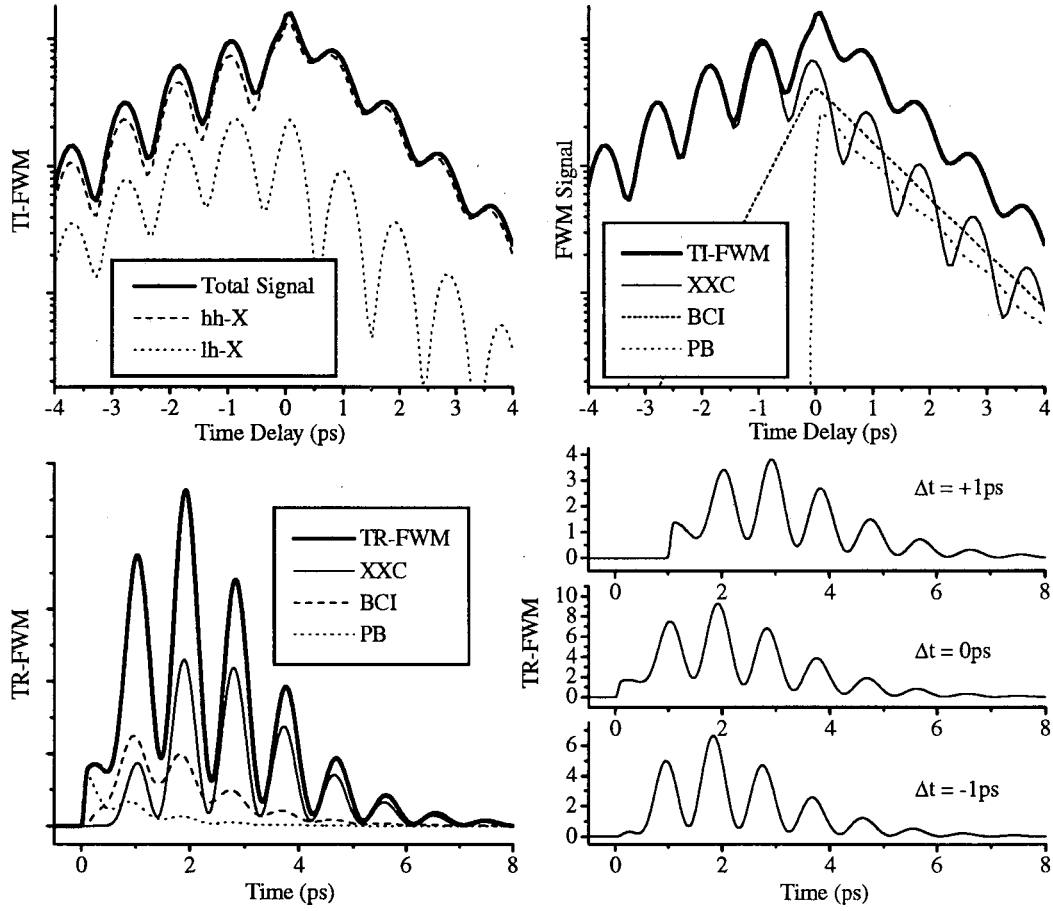

Figure 6.6: TI-FWM and TR-FWM calculated from eqns. 6.24 - 6.28. $P_s = 1$, $\nu = 10^{-3}$, $V_{aa} = V_{bb} = V_{ab} = 10^{-6}$, $\gamma_P = 0.0005\text{fs}^{-1}$ and $\gamma_B = 0.0005\text{fs}^{-1}$.

$$\left[-i\frac{\partial}{\partial t} - i\gamma_B - \Omega_{hh} - \Omega_{lh}\right] B^{ab}(t) \quad = \quad V_{ab}P^a(t)P^b(t) \tag{6.28}$$

The superscript a refers to the hh transition from the $m_J = +3/2$ valence band to the $m_s = +1/2$ conduction band and the superscript b refers to the lh transition from the $m_J = +1/2$ valence band to the $m_s = -1/2$ conduction band. B^{ab} refers to the 4-particle correlation $B^{c+1/2,lh,c-1/2,hh}$. Figure 6.6 gives some of the TI-FWM and TR-FWM results showing that the quantum beating is due solely to the 4-particle correlations and that the strength of the lh-X signal is increased by the 4-particle correlations.

6.6 Effect of the magnetic field

The structure of the unbound biexcitons which is contained in the quantity $B^{ehe'h'}_{k_1k_2k_3k_4}$ is clearly changing as the magnetic field is increased. The problem of biexciton states (or, equivalently, the molecule H_2) in strong magnetic fields has been studied by many authors — see [41] and [43] and references therein. For the situation, $B \sim B_c$ which we have investigated, the magnetic energy and the Coulomb energy are of comparable strength, and there is no straightforward perturbative solution for finding the energy states of the hydrogen molecule, but the problem has been solved for the case of a magnetic field parallel to the molecule axis using a numerical Hartree-Fock approach [43].

For the regime $0.18 < B/B_c < 14$, the ground state of the biexciton is the unbound state $^3\Sigma_\mu$ and the excitons will only interact weakly. As mentioned in chapter 2, when the excitons are far apart the interaction is a quadrupole-quadrupole interaction. It is possible that this interaction is responsible for the strong exciton-exciton correlations which become more pronounced as the quadrupole moment of the exciton grows with magnetic field. For two excitons in a magnetic field, the potential of the quadrupole-quadrupole interaction is

$$U(R,\theta) = \frac{1}{R^5} P_4(\cos\theta) \tag{6.29}$$

where R is the separation between the excitons, θ is the angle between $\vec{B}$ and the exciton-exciton axis, and $P_4(x)$ is the fourth Legendre polynomial. This potential can be either attractive or repulsive depending on the angle θ.

6.7 Propagation/Polariton effects

An effect which has not been taken into account in theory is the effect of the propagation of light through the sample. Propagation effects can also result in a FWM signal for $\Delta t < 0$ in optically dense samples [8, 35, 70]. To ensure that we can neglect propagation effects, we have done measurements on 1 micron and 0.5 micron layers in addition to the 0.25 micron layer. These measurements are discussed in chapter 8. In the thicker layers we see reabsorption of the FWM signal which shows up in the FWM-PS as a splitting of the resonance which is not seen in the 0.25 micron sample.

Our results are not in agreement with the theoretical predictions for propagation effects. In [8], Bakker and Kurz predict a rise time of $T_2/4$ due to propagation effects as well as a nonlinear beating in the TR-FWM and TI-FWM signals. They made calculations for a 1 micron layer of GaAs which showed a smaller signal for S_{TI}^{-} than we see in a 0.25 micron layer, and we don't see the nonlinear beating that appears in their calculations. We conclude that propagation effects are not important in these experiments.

6.8 Conclusion

We have developed a theory which calculates the FWM signal for bulk GaAs in a magnetic field taking into account the effects of 2-particle and 4-particle correlations. The theory is developed using the formalism of the Dynamics Controlled Truncation Scheme to third order in the electric field. From the theory we see that the 4-particle correlations are responsible for the large S_{TI}^{-} and slow τ_r as well as the interactions between the lh-X and hh-X. A simpler model which captures the essential physics of the full theory has also been

described.

6.9 Appendix

In this appendix, we give some further equations and definitions for the $\chi^{(3)}$ Truncation Scheme in a magnetic field, eqns. 6.20 and 6.21. The equations for P_k^{eh} and $B_{k_1k_2k_3k_4}^{ehe'h'}$ in a magnetic field are:

$$
\begin{aligned}
&(-i\hbar\frac{\partial}{\partial t} - i\hbar\gamma - \epsilon_k^e - \epsilon_k^h)P_k^{eh} + \sum_{q\eta}\nu_{k-q}^{\eta,0}P_q^{eh} = \mu^{eh}E \\
&-\sum_{e'h'}(\mu^{e'h}EP_k^{eh'} + \mu^{eh'}EP_k^{e'h})(P_k^{e'h'})^* + \\
&\sum_{q\eta,e'h'}\nu_{k-q}^{\eta,0}((P_k^{e'h'})^* + (P_q^{e'h'})^*)(P_q^{eh'}P_k^{e'h} + P_k^{eh'}P_q^{e'h}) \\
&\sum_{k'q\eta,e'h'}\nu_q^{\eta,0}((P_{k'}^{e'h'})^* - (P_{k'+q}^{e'h'})^*)(B_{k+q,k,k'+q,k'}^{ehe'h'\eta} + B_{k,k+q,k',k'+q}^{ehe'h'\eta})
\end{aligned}
\tag{6.30}
$$

and

$$
\begin{aligned}
&(-i\hbar\frac{\partial}{\partial t} - i\hbar\gamma_B - \epsilon_{k+q}^e - \epsilon_{k'+q}^{h'} - \epsilon_{k'}^{e'} - \epsilon_k^h)B_{k+q,k'+q,k',k}^{eh'e'h\eta} \\
&-\sum_{q'\eta'}[\nu_{q'}^{\eta-\eta',\eta}(B_{k+q-q',k'+q,k'+q',k}^{eh'e'h\eta'} + B_{k+q,k'+q-q',k',k+q'}^{eh'e'h\eta'}) \\
&-\nu_{q'}^{\eta-\eta',0}(B_{k+q-q',k'+q-q',k';k}^{eh'e'h\eta'} + B_{k+q,k'+q,k'-q',k-q'}^{eh'e'h\eta'}) \\
&-\nu_{q'}^{\eta',\eta}(B_{k+q-q',k'+q,k',k-q'}^{eh'e'h\eta} + B_{k+q,k'+q-q',k'-q',k}^{eh'e'h\eta})] \\
&= -\frac{L^2}{2\pi l^2}\nu_q^{\eta,0}(P_k^{eh} - P_{k+q}^{eh})(P_{k'+q}^{e'h'} - P_{k'}^{e'h'}) \\
&-\sum_{\eta'}\nu_{k-k'}^{\eta',\eta}(P_{k'+q}^{eh'} - P_{k+q}^{eh'})(P_k^{e'h} - P_{k'}^{e'h}) + O(E^6)
\end{aligned}
\tag{6.31}
$$

$\tilde{B}$ and $\tilde{\tilde{B}}$ are defined as follows.

$$
B_{k+q,k'+q,k',k}^{eh'e'h\eta} = \sum_{k_y,k_y'}\exp(il^2(k_y - k_y')q_x)B_{\mathbf{k+q},\mathbf{k'+q},\mathbf{k'},\mathbf{k}}^{eh'e'h} \tag{6.32}
$$

$$
B_{k+q,k'+q,k',k}^{eh'e'h\eta} = \tilde{B}_{k+q,k'+q,k',k}^{eh'e'h\eta} - \tilde{\tilde{B}}_{k',k'+q,k+q,k}^{e'h'ehn} \tag{6.33}
$$

$$\tilde{B}^{eh'e'h\eta}_{k+q,k'+q,k',k} = \sum_{nm} \tilde{B}^{eh'e'h}_{nm,q,\eta} \phi^{eh}_{n,\eta}(k+\beta q)\phi^{e'h'}_{m,\eta}(k'+\alpha q) \tag{6.34}$$

$$\tilde{\tilde{B}}^{e'h'ehn}_{k',k'+q,k+q,k} = \sum_{nm} \tilde{\tilde{B}}^{e'h'eh}_{nm,k'-k,\eta} \phi^{e'h}_{n,\eta}(k+\beta(k'-k))\phi^{eh'}_{m,\eta}(k'+q+\alpha(k'-k)) \tag{6.35}$$

$\tilde{B}^{eh'e'h\eta}_{k+q,k'+q,k',k}$ ($\tilde{\tilde{B}}^{e'h'ehn}_{k',k'+q,k+q,k}$) is the solution of eqn. 6.31 with only the first (second) term included. The matrix elements in eqns. 6.20 and 6.21 are given below.

$$V^{XC}_{nmji,q,\eta} = \sum_{kk'} \nu^{\eta,0}_{k-k'} \phi^{e'h}_{n,\eta}(k+\beta q)\phi^{eh'}_{m,\eta}(k'+\alpha q)$$
$$\times(\phi^{e'h'}_{j0}(k'+q) - \phi^{e'h'}_{j0}(k+q))(\phi^{eh}_{i0}(k) - \phi^{eh}_{i0}(k')) \tag{6.36}$$

From [64]

$$b^{eh'e'h'}_{nml} = \sum_{k} \phi^{eh}_{n,0}(k)\phi^{eh'}_{m,0}(k)\phi^{e'h'}_{l,0}(k) \tag{6.37}$$

$$V^{st}_{nmlk} = \sum_{kq} \nu^{0,0}_{k-q} \phi^{eh*}_{n,0}(k)(\phi^{e'h'*}_{m,0}(k) - \phi^{e'h'*}_{m,0}(q))$$
$$\times(\phi^{eh'}_{k,0}(q)\phi^{e'h}_{l,0}(k) + \phi^{eh'}_{k,0}(k)\phi^{e'h}_{l,0}(q)) \tag{6.38}$$

$$M^{eh}_{in,q,\eta} = \sum_{k} \phi^{eh}_{i,\eta}(k)(\phi^{eh}_{n,\eta}(k-\alpha q) - \phi^{eh}_{n,\eta}(k+\beta q)) \tag{6.39}$$

$$\alpha \equiv \frac{m_e}{m_e+m_h} \tag{6.40}$$

$$\beta \equiv \frac{m_h}{m_e+m_h} \tag{6.41}$$

Chapter 7

Properties of 4-particle Correlations

7.1 Introduction

Now that S_{TI}^{-} at high magnetic field has been identified as resulting from 4-particle correlations, we can set the magnetic field at 10 Tesla and vary other parameters in order to study the properties of the 4-particle correlations. In this chapter, we discuss three experiments done at high magnetic field where there is a strong signal due to 4-particle correlations. This is a rare opportunity because the 4-particle correlations are difficult to access experimentally. We are seeing the effect of unbound 4-particle correlations which are not revealed by a resonance in the spectrum as are bound biexcitons. The two questions we explore are how do the X-X interactions change as the X-X separation changes and how sensitive is the coherence of the X-X correlations.

7.2 Density dependence

By changing the exciton density, the length scales over which 4-particle correlations persist can be studied, as can their sensitivity to density. Figure 7.1 shows a series of TI-FWM curves for different densities between $N \approx 10^{17}\text{cm}^{-3}$ and $N \approx 5 \times 10^{14}\text{cm}^{-3}$. We change the density by changing the laser intensity, so, in all cases, we are dealing with an initially coherent population. At the lowest density (lowest curve in Fig.7.1), $S_{TI}^{-} > S_{TI}^{+}$ and $\tau_r \gg \tau_d$, both of which indicate the presence of 4-particle correlations. At this density the average separation between excitons is $\sim 9a_0$. Because the correlations are in scattering states (not bound biexcitons), it is reasonable to assume that the exciton distribution is uniform and the excitons are correlated over distances of $9a_0$. It is remarkable that the 4-particle correlations exist over such large distances. As the density is decreased further, we would expect that at some separation the excitons must start to behave like independent two-level systems, but this density is too low for us to access experimentally.

At high densities, S_{TI}^{-} has a shape consistent with the mean-field theory. $S_{TI}^{-} < S_{TI}^{+}$ and $\tau_r = \tau_d/2$. In fact, it is interesting to note that the data at high density and high magnetic field is in better agreement with the mean-field theory than the data at B=0T. At high densities, the excitons are very close together allowing each exciton to interact with many of its neighbors over the time scale of the experiment. This is exactly the regime in which mean-field theory is valid. We see that the transition to the mean-field regime occurs at an X-X separation of $\sim 2a_0$. Below this density, the mean free time for X-X scattering is of the order of the rise time of the FWM signal. Not enough scattering events occur over the time span of the experiment for the mean-field conditions to be established. Thus, what is observed in our experiments are the deviations from the mean-field theory, i.e. the

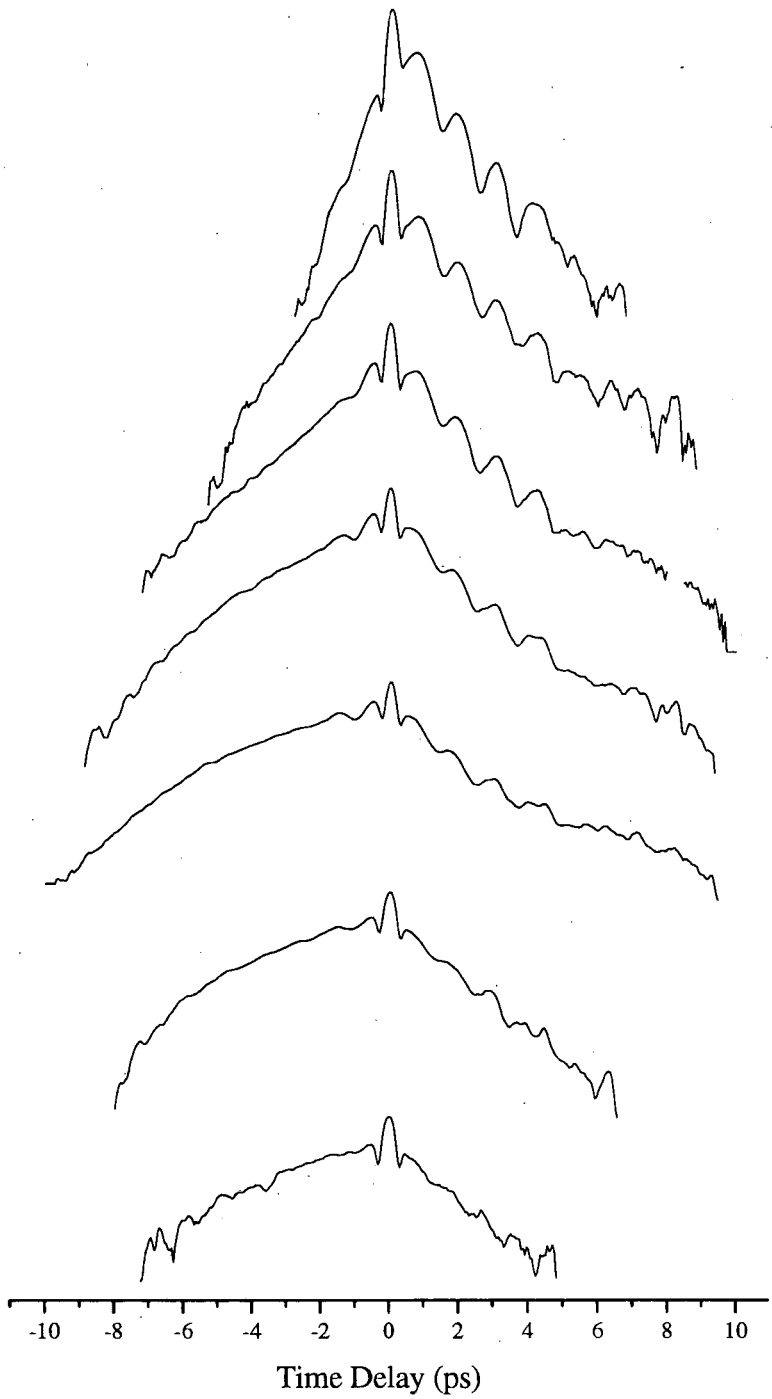

Figure 7.1: TI-FWM vs. Density at B=10T on logarithmic scale. From top to bottom: $N \approx 10^{17}\text{cm}^{-3}$, N/2, N/3, N/6, N/20, N/63, and N/200. These densities correspond to X-X separations of $1.5a_0$, $1.9a_0$, $2.2a_0$, $2.8a_0$, $4a_0$, $6a_0$, and $9a_0$. The curves are displaced for clarity.

fluctuations in X-X scattering which are accounted for by $B^{ehe'h'}_{k_1k_2k_3k_4}$. We might expect the mean-field theory to work well even at very low densities because the Coulomb interaction is a long-range force, but the excitons are neutral so the interaction is not via a $1/r$ potential. The potential of the quadrupole-quadrupole interaction is $\propto 1/r^5$.

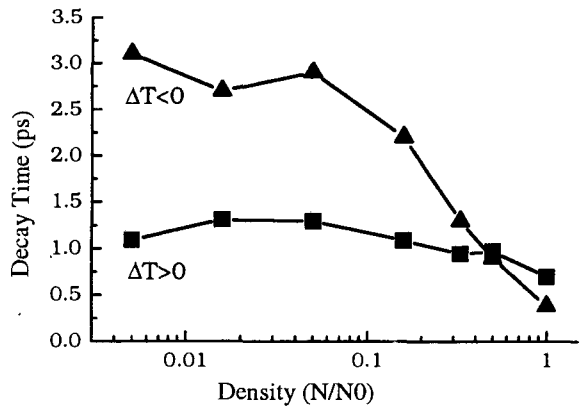

Figure 7.2: τ_r and τ_d vs. density. $N0 = 10^{17}\text{cm}^{-3}$.

Another possible explanation for the changes with density is an increase in screening with density which would cause a reduction in the Coulomb interaction non-linearity. As the density is increased, we also expect the screening to increase, but the nearest neighbor distance decreases faster than the interaction length. $r \propto N^{-\frac{1}{3}}$ and even for Thomas-Fermi screening the interaction length is $\lambda_{TF} \propto N^{-\frac{1}{6}}$. Here we are dealing mainly with an exciton gas for which we can treat the screening as wavevector independent [27].

As is clear from the changes in the shape of $S_{TI}(\Delta t)$ with density seen in Fig. 7.1, we are not in the $\chi^{(3)}$ regime where $S_{TI}(\Delta t = 0) \propto I^3$. This is shown more clearly in figure 7.3 where $S_{TI}(\Delta t = 0)$ is plotted against the input intensity. This is in agreement with recent work [82] that has shown that in bulk GaAs (at zero magnetic field) at densities as low as 2×10^{14} cm^{-3} the FWM signal is still not in the $\chi^{(3)}$ regime. Many-body effects which cannot be well described by an expansion in powers of the electric field play an important role even at densities where the excitons are quite far apart.

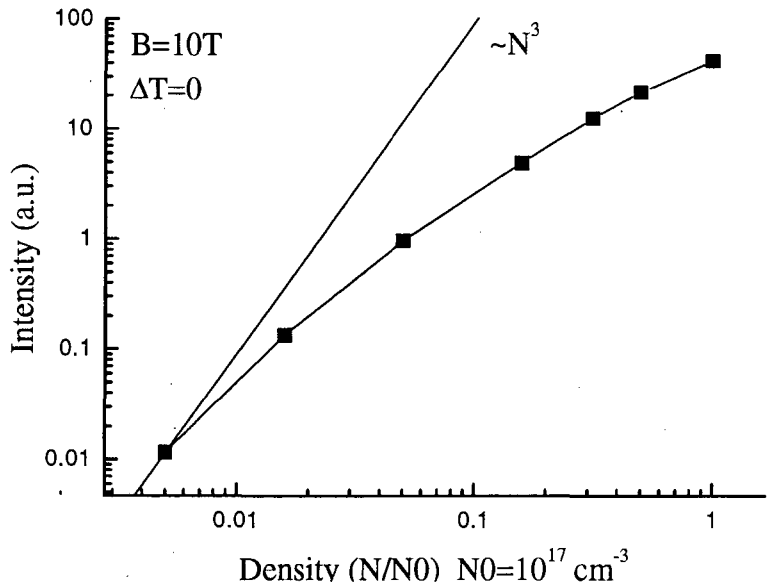

Figure 7.3: Peak FWM Intensity vs. carrier density

7.3 Coherence

Another important question about 4-particle correlations is their coherence. In semiconductor physics, the coherence (or dephasing) of excitons — 2-particle correlations — has been studied extensively, but the coherence of correlations between excitons has almost never been looked at. Even the coherence of bound biexcitons is not well studied. Here we have a unique opportunity to examine the coherence of X-X correlations.

We can determine the exciton dephasing time directly from the decay of S^{+}_{TI}. The 4-particle dephasing time determines S^{-}_{TI}, but the situation is not as simple because the rise time of S^{-}_{TI} is determined by both the exciton dephasing time and the 4-particle dephasing time as well as the strengths of the BCI and XXC nonlinearities. Nevertheless, we can still extract information about the 4-particle coherence. First we have studied the effect of temperature on the 4-particle and 2-particle coherence. This should give information

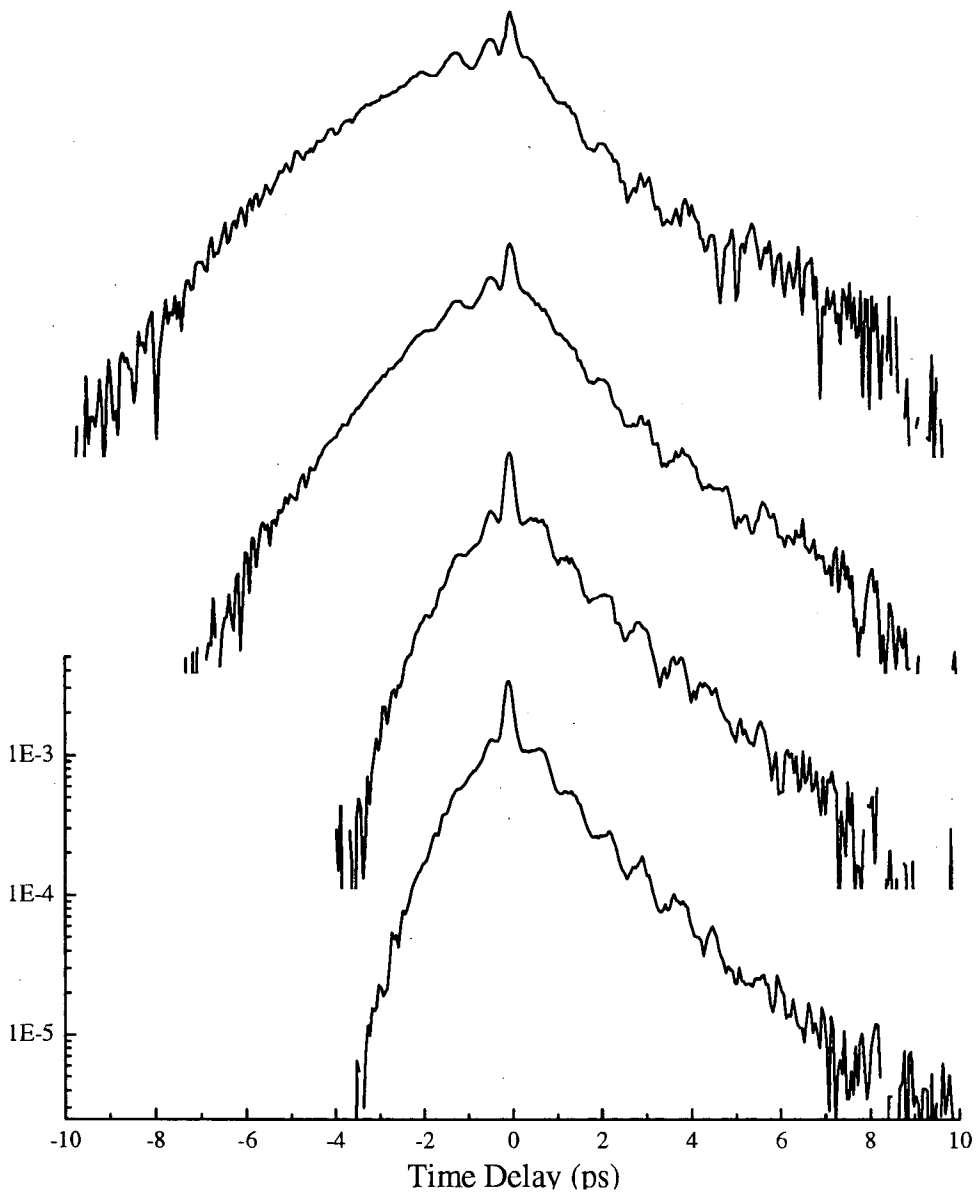

Figure 7.4: TI-FWM on the Sandia sample for temperatures 2K, 16K, 29K and 44K (from top to bottom).

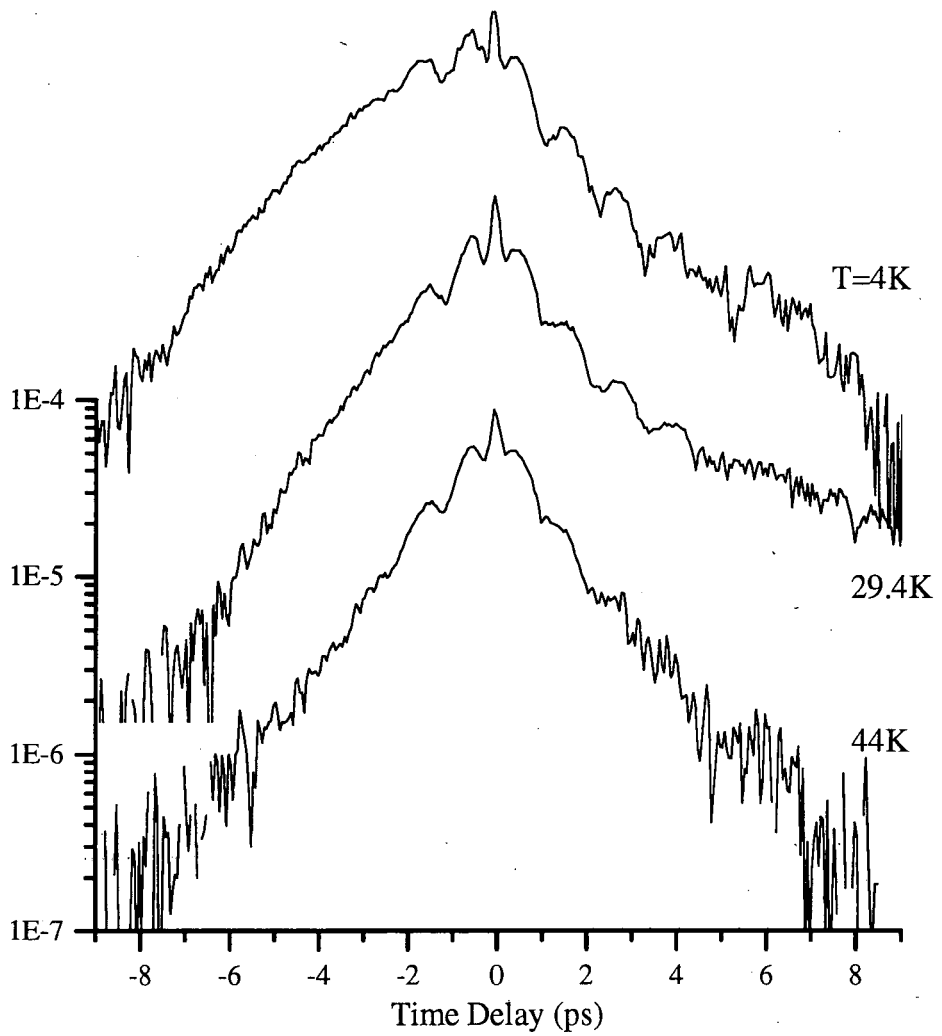

Figure 7.5: TI-FWM on the Bell Labs sample for temperatures 4K, 29K and 44K (from top to bottom).

about phonon scattering processes involving 2 correlated excitons as compared with single exciton-phonon scattering.

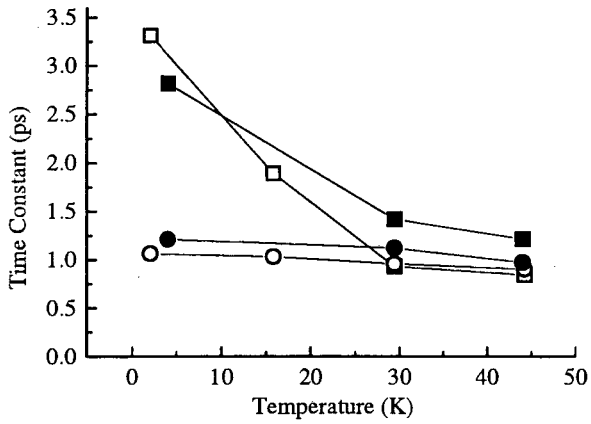

Figure 7.6: τ_r (squares) and τ_d (circles) vs. temperature. Solid symbols are for the Bell Labs sample and open symbols are for the Sandia sample.

Figure 7.4 shows a series of TI-FWM curves for four different temperatures between 2K and 44K taken on the Sandia sample. The magnetic field was kept at B=10T, and the laser was again tuned between the lh-X and the hh-X. As the temperature is increased, the band edge shifts to lower energy and the laser was retuned to keep the overlap roughly the same. The density of excited e-h pairs is roughly $N \approx 10^{16}$ cm^{-3} corresponding to an average distance between pairs of 40nm $\approx 3.3a_0$. Between 2K and 44K τ_d changes by only about 10%, indicating that the exciton dephasing rate does not change significantly in this temperature range. In contrast τ_r changes by more than a factor of 3, indicating a strong change in the dephasing of the X-X correlations. We estimate τ_r from the slope of S_{TI}^- between $\Delta t = -2$ps and $\Delta t = -0.5$ps, and τ_d from the slope of S_{TI}^+ between $\Delta t = 0.5$ps and $\Delta t = 2$ps. TI-FWM measurements taken on the Bell Labs sample vs. temperature are shown in Fig. 7.5. The rise and decay time are shown plotted against temperature in Fig. 7.6.

The theory does not explicitly include phonon interactions, so that all temperature effects are included in the dephasing parameters from eqns. 6.20 and 6.21, γ_P and γ_B. Thus to model the effects of temperature shown in Fig. 7.4, we have made a calculation of the full theory with $\gamma_B = 2\gamma_P$. The resulting TI-FWM is shown in Fig. 7.7. For comparison,

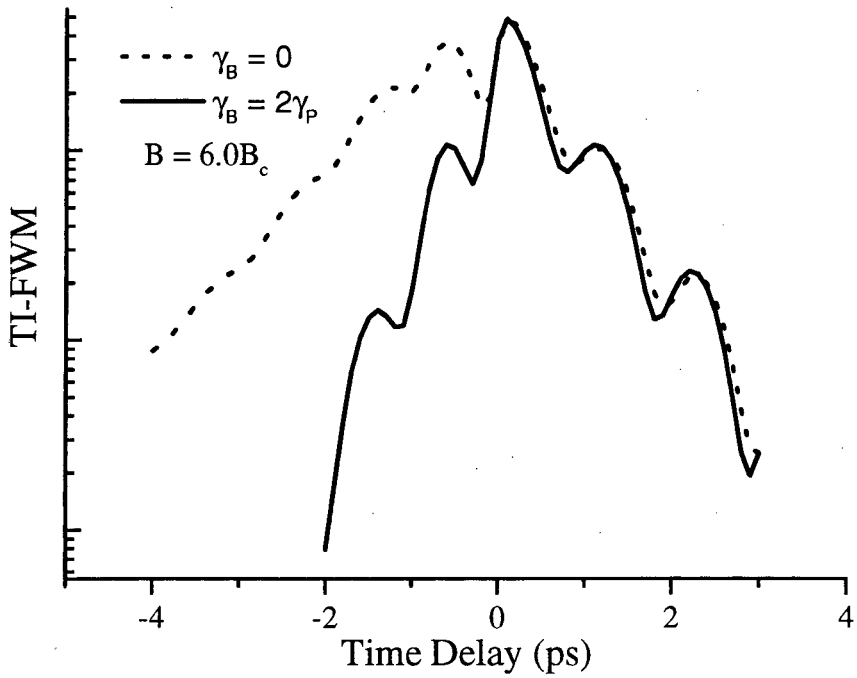

Figure 7.7: $\chi^{(3)}$ Truncation Scheme calculation with $\gamma_B = 2\gamma_P$.

the curve with $\gamma_B = 0$ is also shown. We see that increasing γ_B reduces S_{TI}^{-} in the same manner as increasing temperature does experimentally.

It is unlikely that LO-phonon scattering plays a significant role because at temperatures below 44K, the LO-phonon occupation number is $< 6 \times 10^{-5}$. The scattering of the phonon and the 4-particle correlation can be viewed as a 3-body scattering problem, as compared to the phonon-exciton scattering which is a 2-body event. The 3-body event has more degrees of freedom in phase space, resulting in more scattering channels. Thus, the 4-particle correlation may be more sensitive to phonons simply because there are more ways for scattering with a phonon to occur. Another factor is that the exciton-exciton correlations, $B^{ehe'h'}_{k_1k_2k_3k_4}$, involve excitons with finite center of mass momentum whereas the exciton polarization, P^{eh}_{k}, only involves excitons with zero center of mass momentum; the dephasing of states with large center of mass momentum is larger than those with 0 center

of mass momentum [63]. Calculations of the dephasing of the 4-particle correlations due to acoustic and LO phonons based on the microscopic theory predict and effect two orders of magnitude lower than that seen experimentally. At present the temperature effect remains unexplained.

Carrier density is also a test for the coherence of the 4-particle correlations. By changing the detuning of the laser, we can change the relative excitation density of bound excitons and free e-h pairs as well as the total excitation density excited by the laser. In this way we can study how both free carriers and bound excitons affect the 4-particle and 2-particle coherences. We are always studying initially coherent populations although the free carriers dephase very rapidly. The effect of incoherent populations on the 2-particle coherence has been investigated by Schultheis *et. al.* [69, 68]. Three curves are shown in Fig. 7.8. The middle curve is for approximately zero detuning (The center freq. of the laser tuned between the lh-X and the hh-X). The top curve is for negative detuning (the laser tuned to lower energy) and the bottom curve is for positive detuning.

At zero detuning the signal is similar to the data in the previous figures. S_{TI}^{-} is large and has only about one oscillation near $\Delta t = 0$. At negative detuning S_{TI}^{-} becomes significantly larger in comparison with S_{TI}^{+}. Also, there are large oscillations in S_{TI}^{-}. As we discuss in the theory section, the lack of oscillations in S_{TI}^{-} for zero detuning is most likely due to exciton-exciton density correlations which are beyond $\chi^{(3)}$ and hence not included in the theory. At negative detuning, fewer excitons are being excited, so the exciton-exciton density correlations become less important, and the oscillations in S_{TI}^{-} become more pronounced. It is also remarkable that the maximum of S_{TI}^{-} is larger than the coherent peak at $\Delta t = 0$. At positive detuning, the coherent peak dominates the signal and the

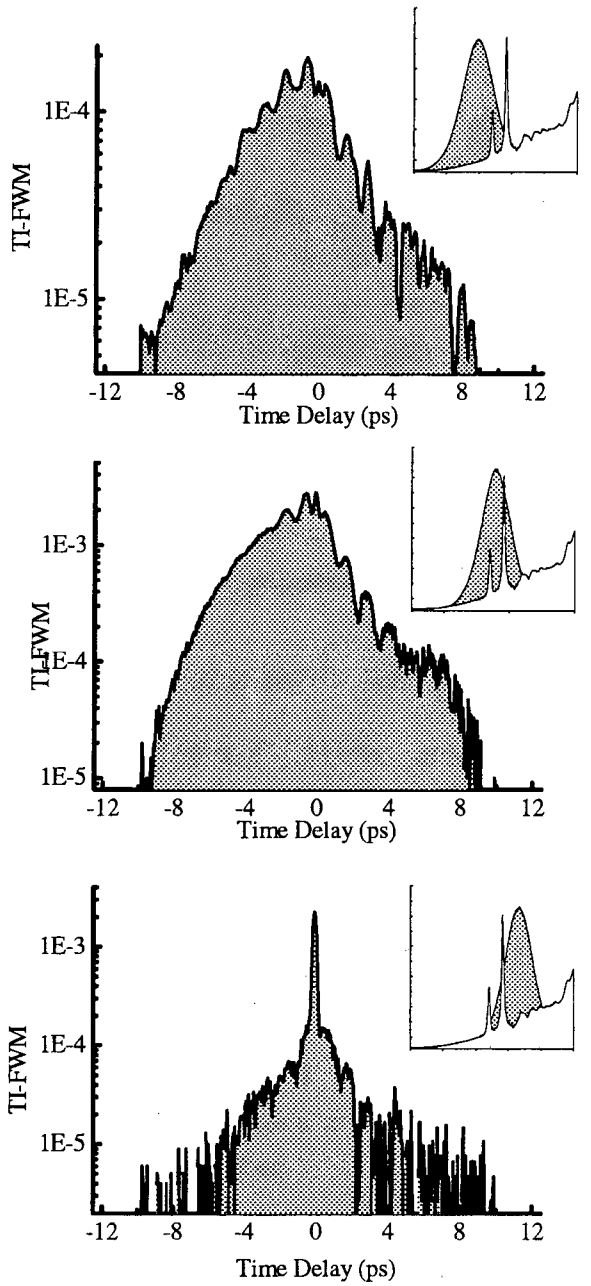

Figure 7.8: TI-FWM for different detunings

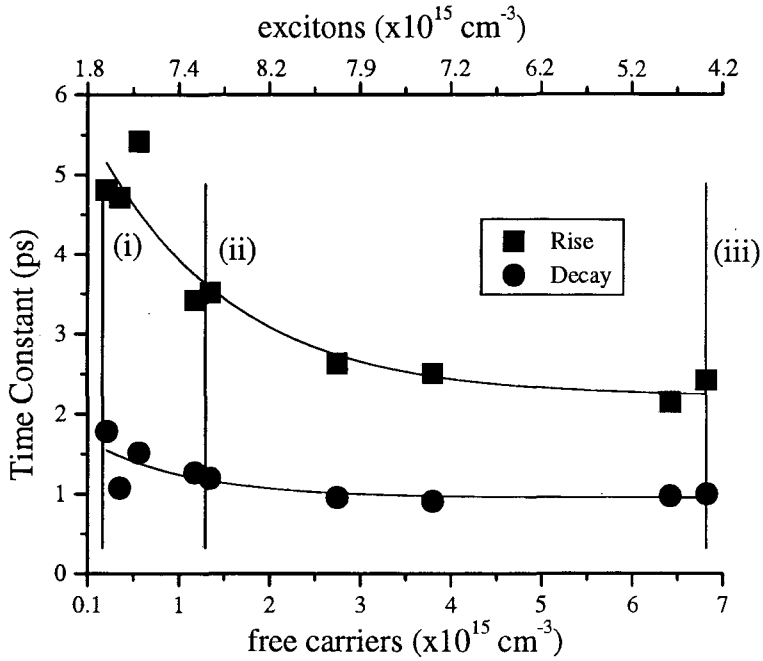

Figure 7.9: τ_r and τ_d vs. free carrier density

magnitude and rise time of S_{TI}^{-} are much diminished although the rise time is greater than $1/4\gamma_P$ indicating that we are not in the mean-field regime.

Here, we are clearly seeing the effects of free carriers on the 4-particle coherence. For the negative detuning, Fig.7.8(i), there are only $N_{eh} \approx 2 \times 10^{14}$ cm^{-3} free carriers excited, whereas for the case of positive detuning, there are $N_{eh} \approx 7 \times 10^{15}$ cm^{-3} free carriers excited. In Fig. 7.9 we plot the rise and decay times verse the free carrier density. The vertical lines show the 3 measurements from Fig. 7.8. On the top axis, the corresponding exciton density is shown. Note that the exciton density is not linear with respect to the x-axis, and that it changes by less than a factor of 3 while the free carrier density changes by more than a factor of 30. Clearly the rise and decay times are more strongly dependent on the free carrier density than on the exciton density. The detuning experiment is harder to interpret than the temperature experiment because the detuning will affect the strength

of the nonlinearities in addition to affecting the dephasing parameters. But, by adjusting the strength of the XXC nonlinearity and the 4-particle dephasing time, it is possible to reproduce the overall shape of Fig. 7.8(i) with the signal maximum at $\Delta t < 0$ using the model described by eqns. 6.22 and 6.23.

7.4 Conclusion

The properties of the 4-particle correlations have been explored at 10 Tesla. Above densities of $\approx 5 \times 10^{16}\text{cm}^{-3}$, there are many exciton-exciton interactions over the time scale of the experiment and mean-field conditions are established. Below this density, the 4-particle correlations dominate S_{TI}^{-}. At densities so low that the excitons are $\sim 9a_0$ apart, the excitons still interact strongly, resulting in a large S_{TI}^{-}. If we increase the temperature at low density, S_{TI}^{-} decreases over a temperature range where S_{TI}^{+} is barely affected suggesting that the coherence of the exciton-exciton correlations is much more sensitive to phonon interactions than the exciton coherence. The sensitivity of the exciton-exciton correlations is also evident in the response of the signal to incoherent free carriers. This is the first time that the coherence of the interactions between the fundamental quasiparticles in a system has been studied.

Chapter 8

Further Experiments

8.1 Introduction

There are three additional experiments that we have done in the course of this work that we have not yet discussed. The first of these experiments is a series of measurements done at high intensity where carrier-carrier scattering is important. Carrier-carrier scattering is the major source of dephasing at high intensities, and we would like to understand how the 1-D motion of the carriers in high magnetic fields affects the dephasing. The second is a series of measurements done with longer pulses that illustrates some of the features already seen with the 100fs pulses. Lastly, we have done experiments on thicker samples in which some propagation effects are seen. We have not investigated propagation effects in detail — our goal is to avoid them — but we would like to point out some of the effects seen in thicker samples.

8.2 High intensity experiments

All the interesting physics that we have discussed so far has been at low densities where strong X-X correlations are seen. For $N <\sim 10^{16}\text{cm}^{-3}$, the decay of the TI-FWM, determined by γ_P, does not change much with magnetic field, but S_{TI}^{-} is very pronounced. At high densities, on the other hand, we don't see the signature of X-X correlations but carrier-carrier scattering becomes important. Because the free carrier motion is strongly affected by the magnetic field, making a transition from 3-D to 1-D behavior, we would like to know how the carrier-carrier scattering is affected by the magnetic field.

Figure 8.1 shows a series of TI-FWM measurements with an excitation density of $N \approx 3 \times 10^{17}\text{cm}^{-3}$. An increase in the decay time, plotted in Fig. 8.2, is clearly seen between 0 Tesla and about 2 Tesla indicating that carrier-carrier scattering is becoming less effective at dephasing the excitons as the magnetic field is increased. Above 4 Tesla, S_{TI}^{-} is clearly visible with $\tau_r \approx \tau_d/2$.

The FWM-PS, Fig. 8.3, shows a decrease in linewidth corresponding to the increase in decay time of the TI-FWM. It is interesting to note that the FWM-PS continues to show changes in the linewidth up to 7 Tesla, even though the decay time doesn't change much after 2 Tesla.

The change in the free carrier motion from 3-D to 1-D is clearly affecting the scattering. The scattering is less efficient because in 1-D it is harder to satisfy both momentum and energy conservation so there are fewer scattering channels. Hence, the dephasing rate decreases.

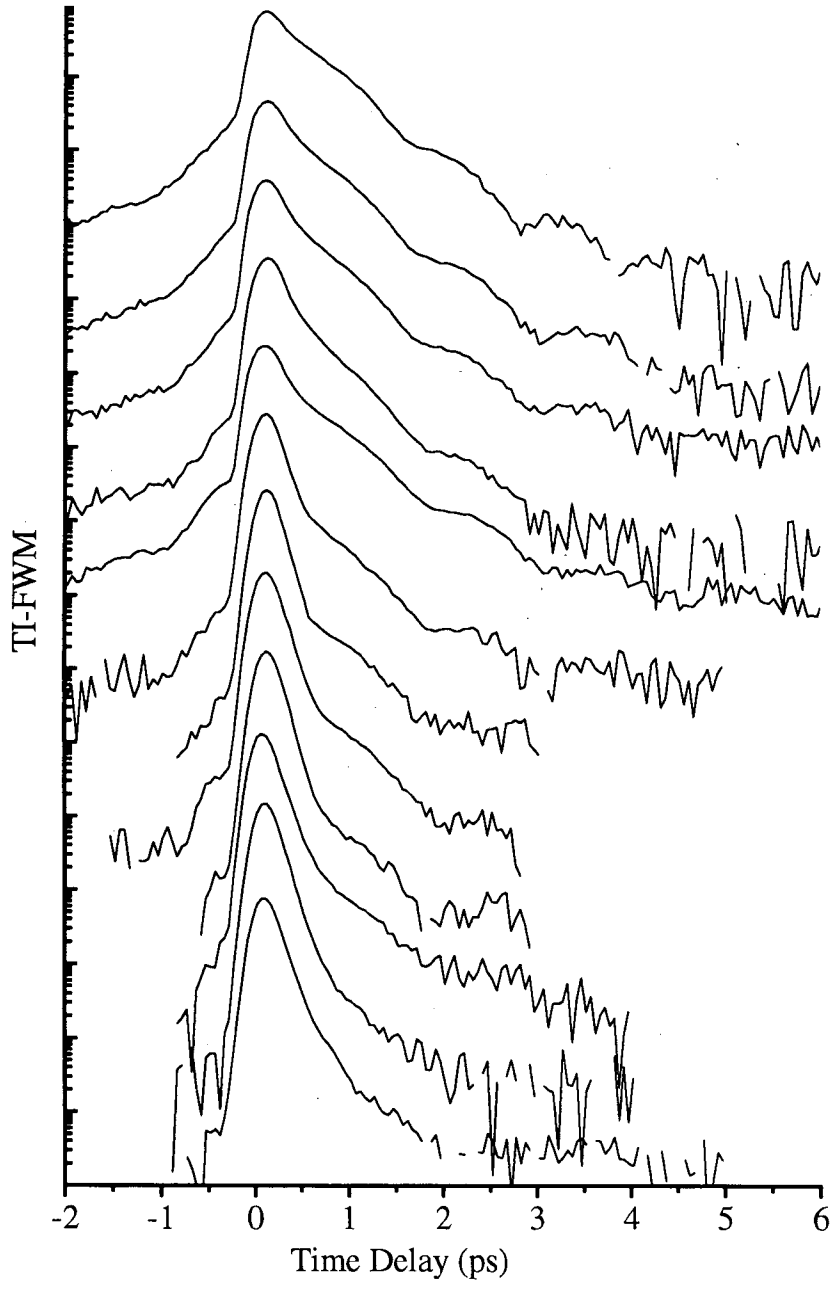

Figure 8.1: TI-FWM vs. B. From bottom to top: B=0, 0.5, 1.0, 1.5, 2.0, 2.5, 3.0, 3.5, 4.0, 4.5, 5.0 and 7.0 Tesla. $N \approx 3 \times 10^{17}\text{cm}^{-3}$.

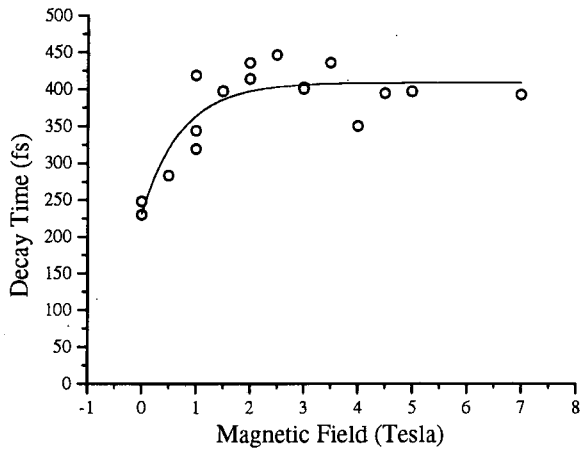

Figure 8.2: τ_d vs. B. τ_d is determined by a fit to a simple exponential decay for $0.7 < \Delta t < 3.7$ps. The solid line is a guide to the eye. Measurements of the TI-FWM at the same field strength indicate that the measurements are reproducible with an uncertainty in the decay time of about 25fs.

8.3 Long pulse measurements

We did a series of measurements with pulses of FWHM between 450fs and 680fs. By using a longer pulse with a narrower spectrum, fewer free carriers are excited. We expected that the exciton-exciton correlations would become more pronounced in this situation.

At B=0T, there is a pronounced difference in the signal. The continuum is close to the hh-X so exciting with a narrower pulse creates significantly fewer free carriers. The TI-FWM, Fig. 8.4, shows a more pronounced S_{TI}^{-} than the data shown in chapter 5. However τ_r is always roughly $0.5\tau_d$, indicating that mean-field theory is valid at B=0T. Table 8.1 gives τ_r and τ_d as well as the excitation densities for the lh-X, hh-X and free carriers (fc) for the curves of Fig. 8.4.

At B=10T, τ_r is again greater than τ_d, as seen in Fig. 8.5. As the laser is detuned to below the lh-X, both τ_r and τ_d increase, but τ_r does not increase in relation to τ_d. As the laser

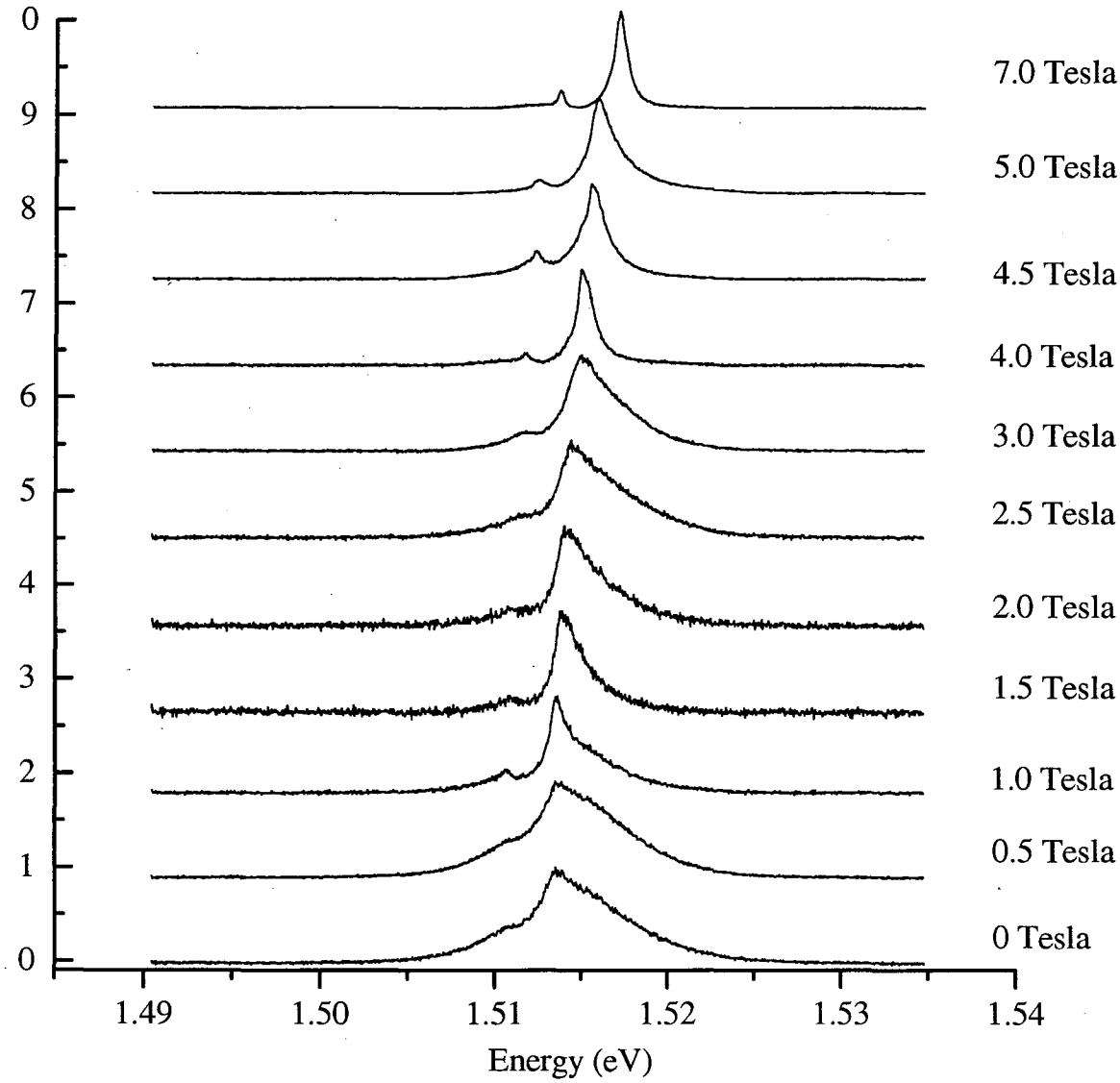

Figure 8.3: Normalized FWM-PS vs. B at $N \approx 3 \times 10^{17}\text{cm}^{-3}$.

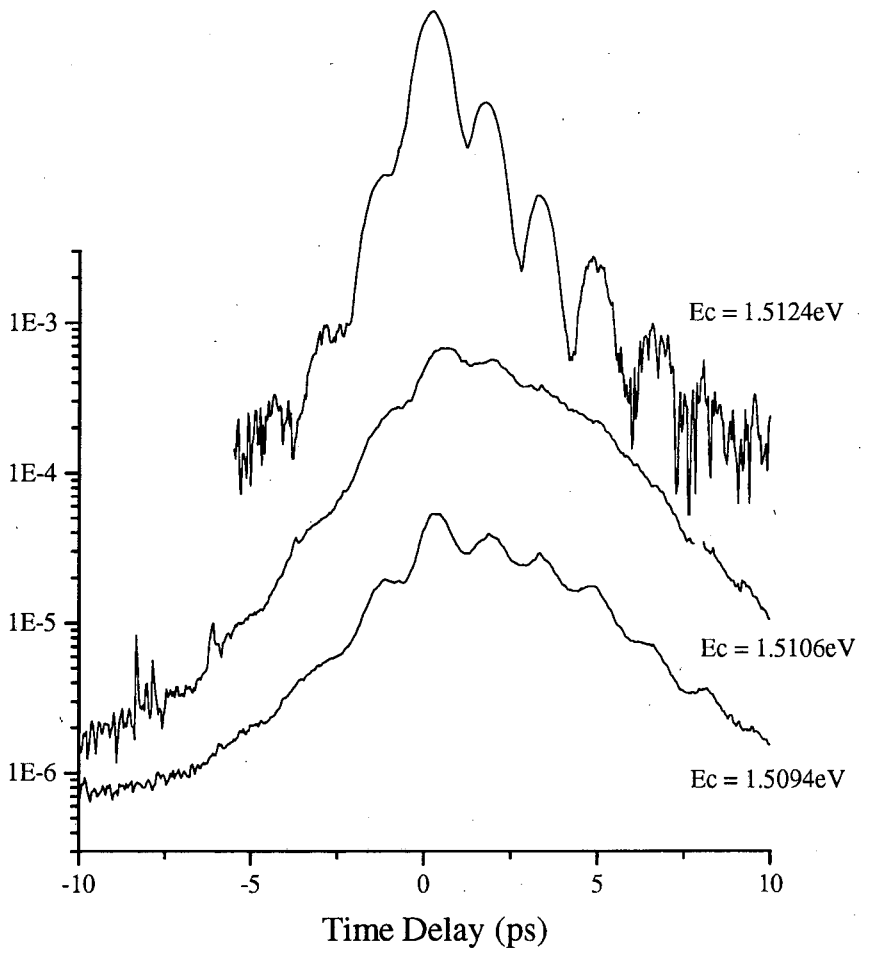

Figure 8.4: TI-FWM at B=0T for different detunings. Ec is the center frequency of the laser pulse. The FWHM of the laser pulse is $\sim$ 600fs. Refer to table 8.1 for the excitation densities and τ_r and τ_d.

Ec (eV)	lh-X (cm^{-3})	hh-X (cm^{-3})	fc (cm^{-3})	τ_r (ps)	τ_d (ps)
1.5124	5.2×10^{15}	2.7×10^{15}	6.3×10^{14}	0.63	1.03
1.5106	1.3×10^{16}	7.2×10^{15}	0	1.3	3.02
1.5094	7.4×10^{15}	3.5×10^{15}	0	1.68	3.34

Table 8.1: e-h pair densities and τ_r and τ_d for the curves in Fig. 8.4. Ec is the center frequency of the laser, and fc stands for free carriers.

Ec (eV)	lh-X (cm^{-3})	hh-X (cm^{-3})	fc (cm^{-3})	τ_r (ps)	τ_d (ps)
1.5214	3.7×10^{14}	1.3×10^{16}	8.2×10^{15}	1.76	0.726
1.5192	1.9×10^{15}	2.2×10^{16}	4.6×10^{15}	2.18	1.11
1.5176	6.0×10^{15}	1.2×10^{16}	3.7×10^{15}	1.98	1.26
1.5159	1.1×10^{16}	3.5×10^{15}	2.1×10^{15}	2.34	2.28
1.5141	6.2×10^{15}	8.6×10^{14}	8.2×10^{14}	4.40	3.23

Table 8.2: e-h pair densities and τ_r and τ_d for the curves in Figs. 8.5 and 8.6.

is detuned the maximum of the signal shifts to S_{TI}^{-} in the same manner as the data taken with the 100fs detuned pulses in the previous chapter. The FWM-PS at B=10T is shown in Fig. 8.6. The hh-X has more pronounced structure than in the other measurements although there was structure above the hh-X in the FWM-PS shown in chapter 5; this is at least partly due to the higher resolution spectrometer which was used for these measurements. The extra peaks in Fig. 8.6 are most likely due to the quantized center of mass motion as is the case with the FWM-PS in chapter 5. It is also possible that this is due to reabsorption in the sample although reabsorption effects seem unlikely for a 0.25μm sample. This possibility is suggested by comparing the FWM-PS with the linear absorption (dashed line in Fig. 8.6) because the peak of the absorption falls between two peaks in the FWM-PS. Table 8.2 gives τ_r and τ_d and the densities for the 10 Tesla measurements. While the measurements with the longer pulse emphasize some of the features seen in the measurements described in the previous chapters, they don't show any completely new features.

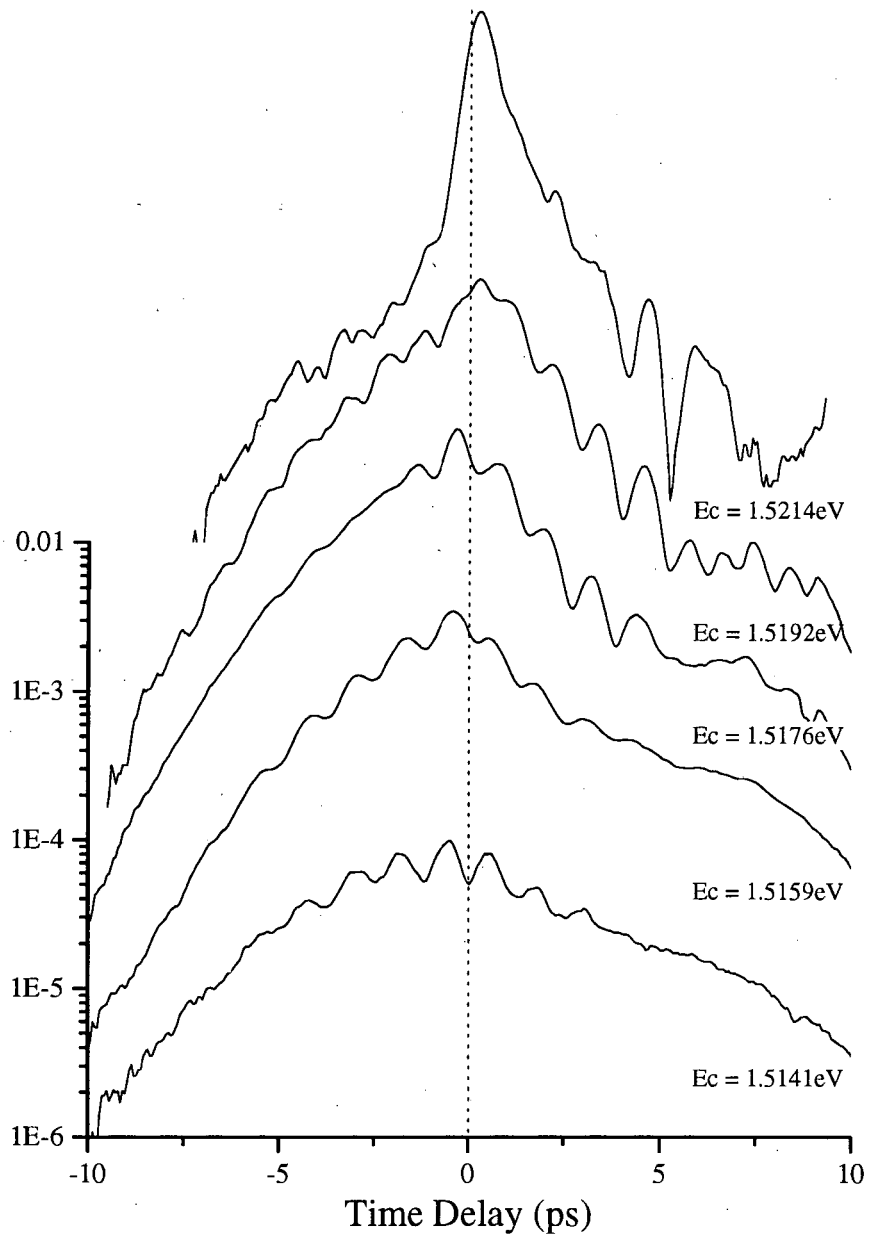

Figure 8.5: TI-FWM at B=10T for different detunings. Refer to table 8.2 for the excitation densities and τ_r and τ_d.

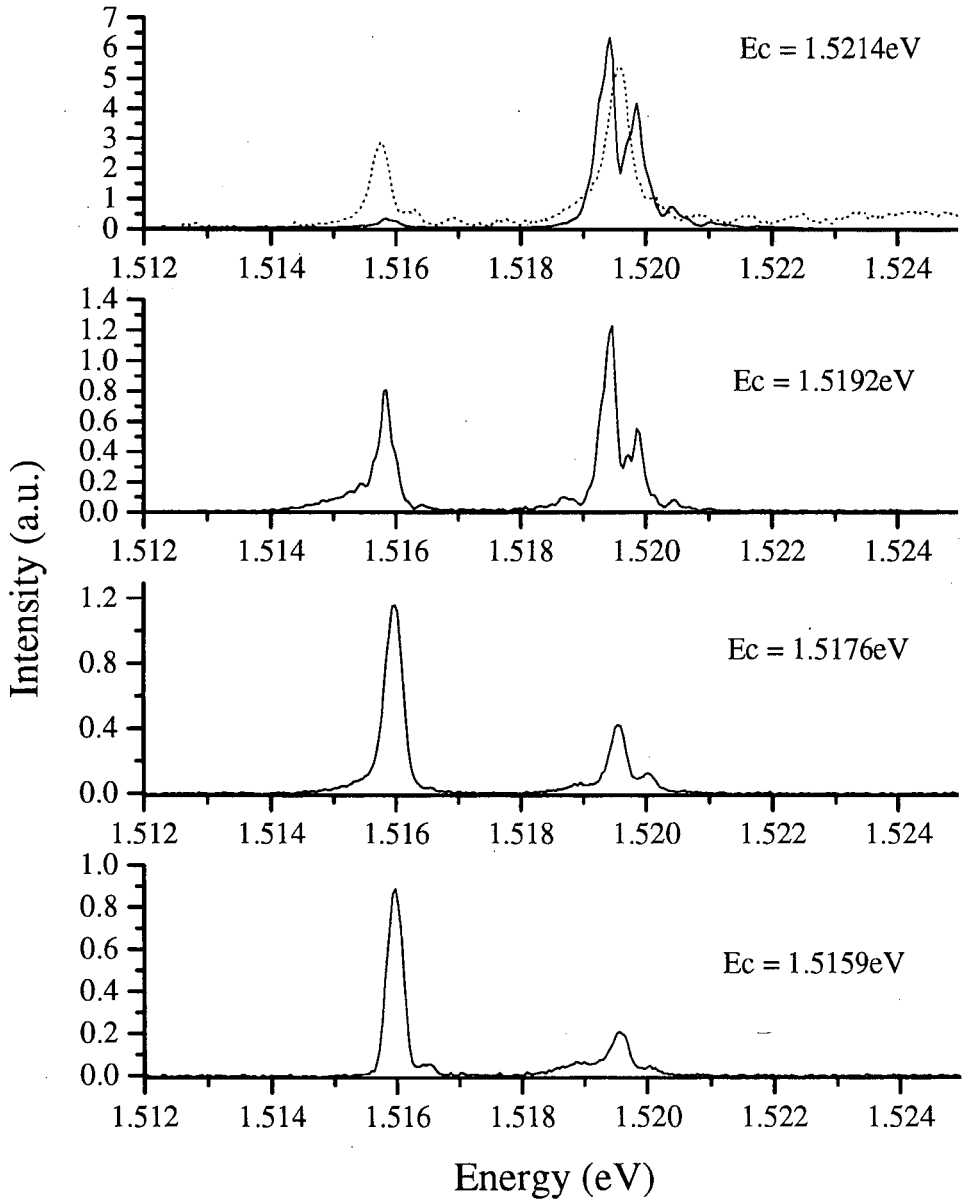

Figure 8.6: FWM-PS at B=10T. The dashed curve is the absorption spectrum. Refer to table 8.2 for the excitation densities and τ_r and τ_d.

8.4 FWM measurements on the 1 micron sample

By making measurements on thicker samples, we can check to see if propagation through the sample has an effect on the FWM experiments. If we look at the TI-FWM measurements on the 1 micron sample at high magnetic field, Figs. 8.7 and 8.8, they do not look significantly different from the measurements done on the 0.25 micron sample. As the magnetic field is increased S_{TI}^{-} increases, and, as the density decreases, S_{TI}^{-} increases. The linewidth of the 1 micron sample — $2\gamma_P \approx 1.2$meV at 0 Tesla — is larger than that of the 0.25 micron samples, and on this sample both τ_r and τ_d are faster. At 10 Tesla, $\tau_r = 1.64$ps and $\tau_d = 1.37$ps.

However, if we look at the FWM-PS, there are important differences in the emission of the different thickness samples. Figure 8.9 shows the FWM-PS at $\Delta t = 0$ and B=10T for the different samples. The 0.5 and 1 micron samples show a pronounced dip in the middle of the hh-X emission peak. This is due to reabsorption of the emitted FWM signal in the sample. Another striking effect that is seen in the thicker sample is the change in the FWM-PS as Δt is changed. This is shown in fig. 8.10. These complicated effects are not seen in the thinner sample and are due to propagation. At B=0T, the propagation effects are less evident.

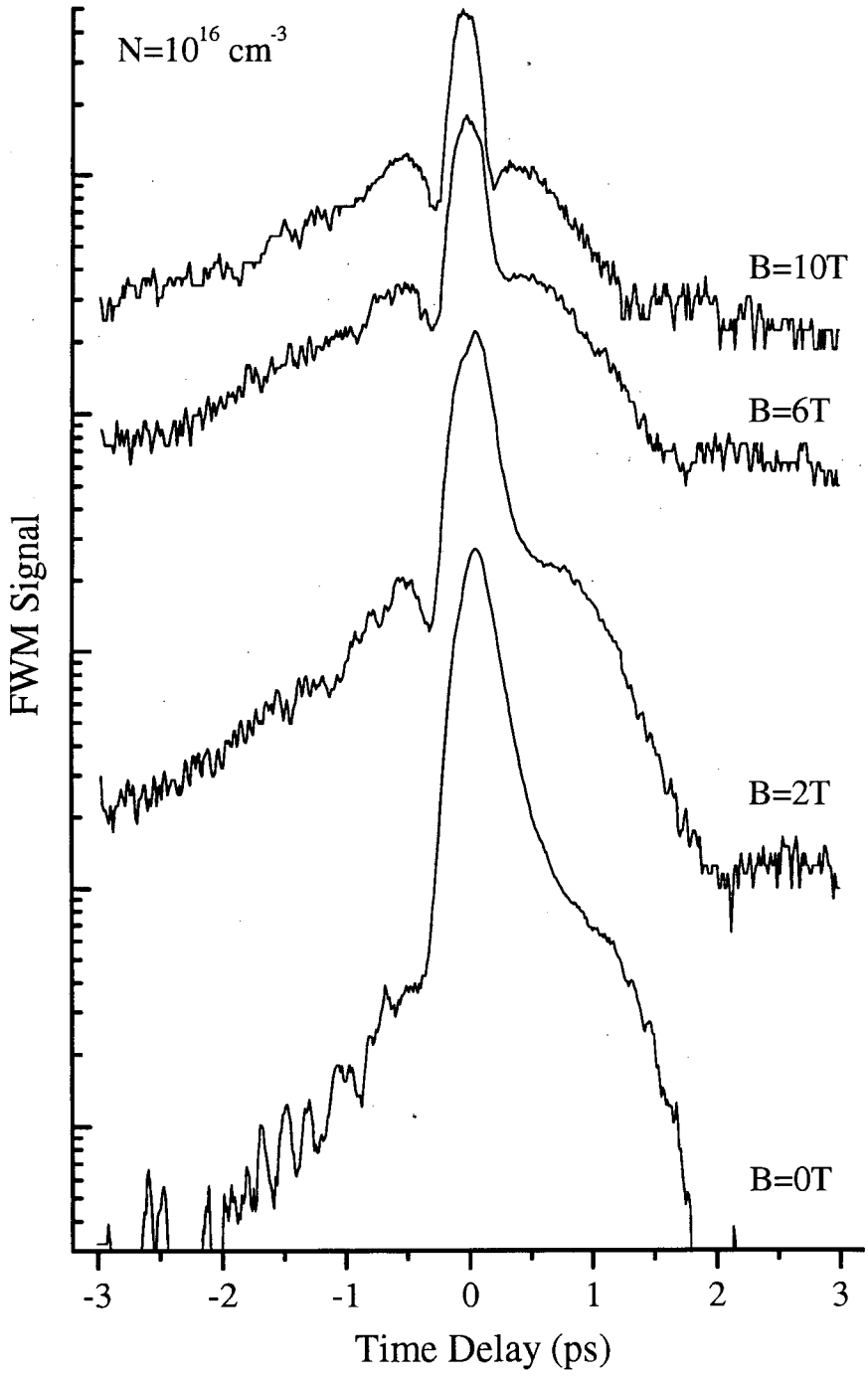

Figure 8.7: TI-FWM vs. B on the 1 micron sample. $I_{k_2} \approx 4I_{k_1}$.

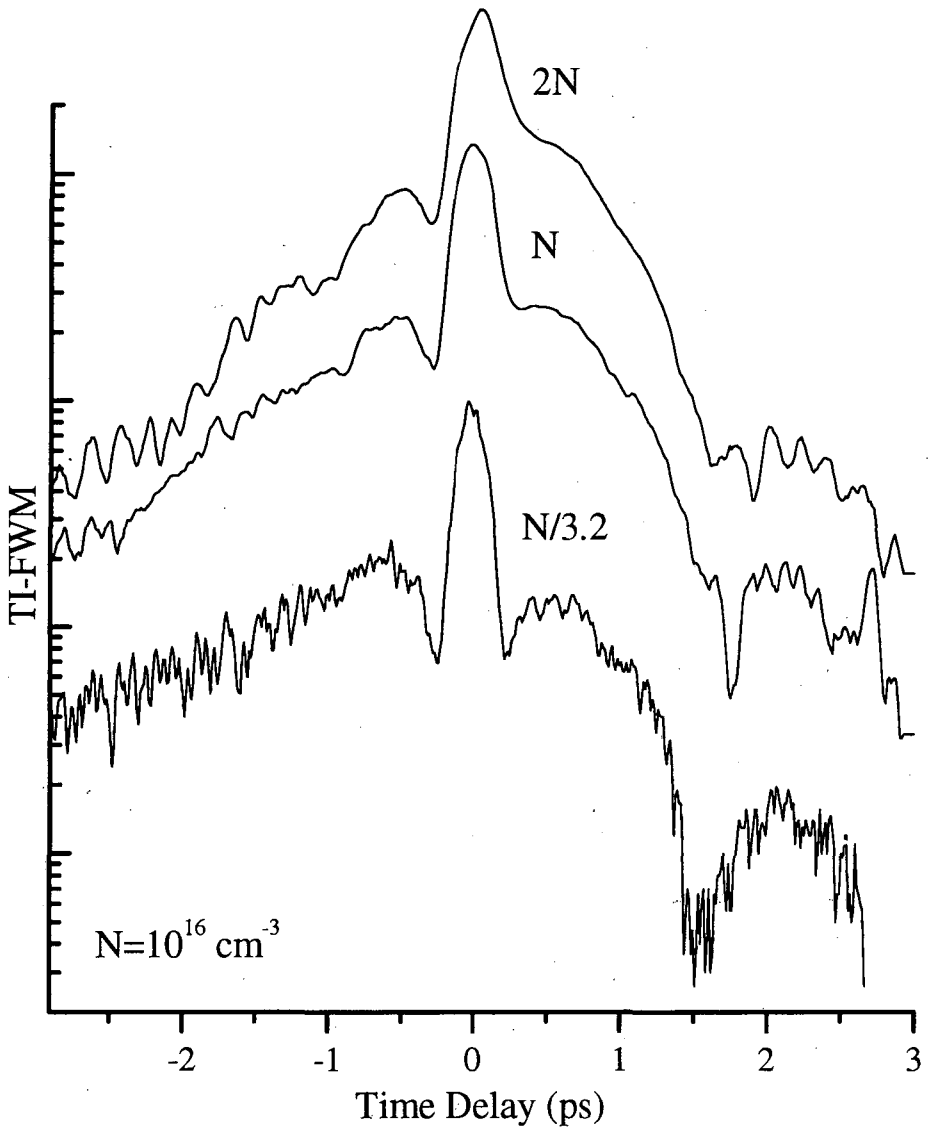

Figure 8.8: TI-FWM vs. density at B=6T on the 1 micron sample. $I_{k_2} \approx 4I_{k_1}$.

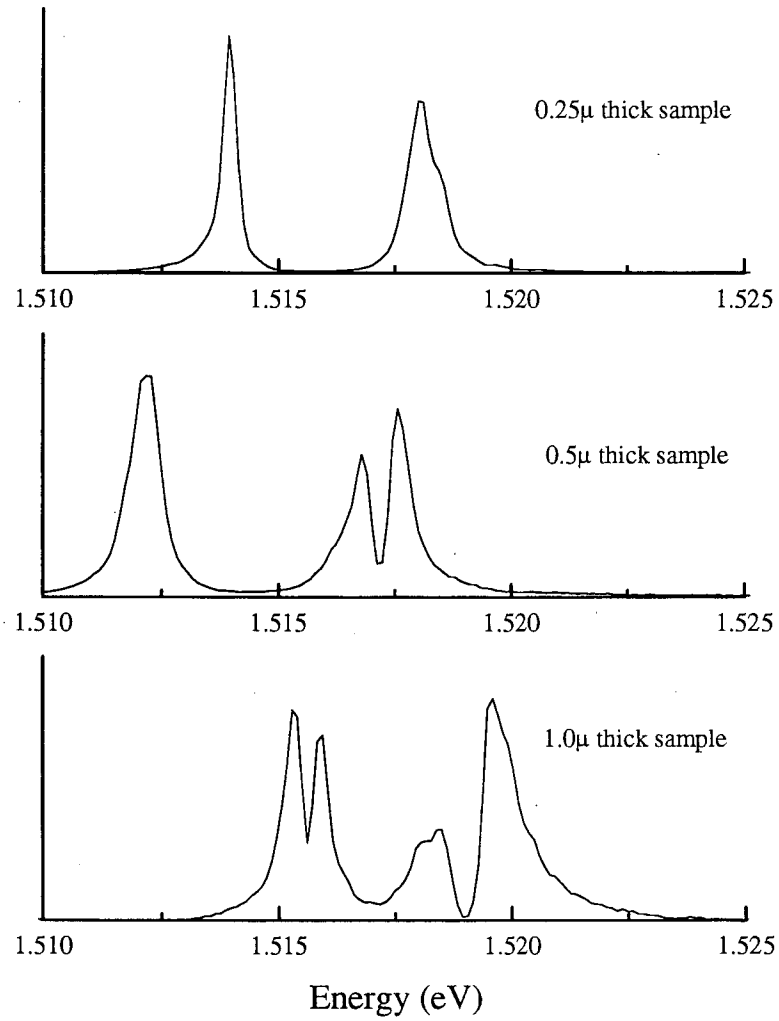

Figure 8.9: FWM-PS at $\Delta t = 0$ for different thickness samples. The stress is different in the different samples which results in shifts in the resonance energies of the different samples.

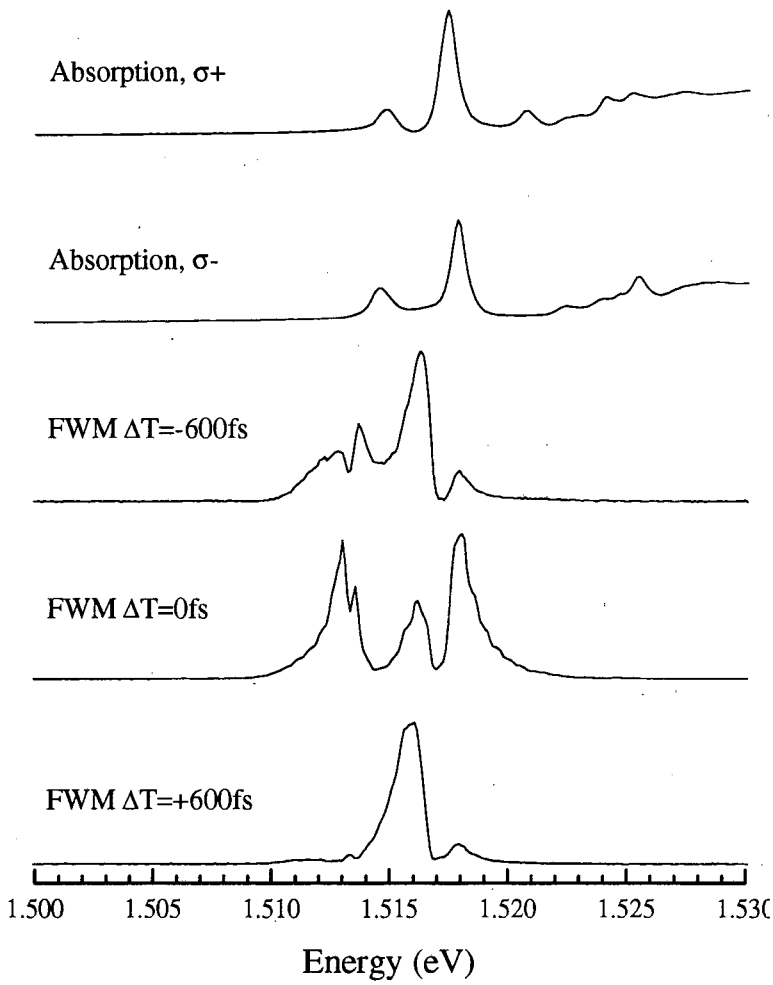

Figure 8.10: FWM-PS vs. Δt for the 1 micron sample at B=10T.

8.5 Conclusion

In this chapter, we have described three additional measurements on bulk GaAs in magnetic fields. Two of the measurements investigate issues other than exciton-exciton correlations that can be studied in this system: carrier-carrier scattering and propagation. The third measurement further investigates the exciton-exciton correlations, using longer excitation pulses. We have shown that dephasing due to carrier-carrier scattering is suppressed at high magnetic fields by the 1-D motion of the free carriers. Looking at thicker samples, we saw that propagation affects the FWM-PS in 0.5 and 1.0 micron thick samples.

Chapter 9

Conclusion

We have performed ultrafast two-pulse degenerate four-wave mixing on bulk GaAs in high magnetic fields. At zero magnetic field, the measured signal is consistent with calculations of the optical response within the time-dependent Hartree-Fock approximation — a mean-field theory at the two-particle level. But at high magnetic fields, we measure a signal that cannot be explained within the mean-field theory. A theory that takes into account exciton-exciton correlations within the biexciton scattering state continuum successfully describes our results.

Time-integrated four-wave mixing measurements show a large signal for a pulse sequence that would produce no signal in an ensemble of independent two-level systems. The mean-field theory predicts a signal smaller than the one we experimentally measure. Only by including the effect of exciton-exciton correlations on the four-wave mixing signal in the theory can we reproduce the shape of the experimentally measured time-integrated four-wave mixing.

Spectrally resolved four-wave mixing measurements support the theoretical expla-

nation. At high magnetic field, the exciton-exciton correlations result in a strong interaction between the light-hole exciton (lh-X) and the heavy-hole exciton (hh-X). This manifests itself as an increase in the lh-X signal relative to the hh-X signal, quantum beating between the lh-X and the hh-X, and an exchange of relative signal strength between the lh-X and hh-X as a function of the time delay between the two input pulses. These results are all beyond the predictions of the mean-field theory and are the result of exciton-exciton correlations.

Having identified the exciton-exciton correlations in our measurements, we then proceeded to explore the nature of these correlations by varying the excitation density, detuning, and temperature. This is the first time, to our knowledge, that the coherent properties of unbound exciton-exciton correlations have been studied. By varying the excitation density at high magnetic field, we see a transition from a regime at high density that can be explained within the mean-field theory to a regime at low density where the exciton-exciton correlations dominate the signal. Surprisingly, the exciton-exciton correlation signal is still strong at densities where the excitons are almost $10a_0$ apart.

The coherence of the exciton-exciton correlations can be studied by changing the temperature of the sample or by detuning the laser. Increasing the temperature increases the supply of incoherent thermal phonons which will lead to the dephasing of the excitons and the exciton-exciton correlations. Between 2K and 44K, the dephasing of the excitons does not change whereas the dephasing of the exciton-exciton correlations is much faster at 44K. Detuning the laser above and below the exciton resonances varies the relative number of free electron-hole pairs that are excited. The free electron hole pairs lose their coherence very rapidly, resulting in a population of incoherent e-h pairs which dephase the excitons and the exciton-exciton correlations. Both of these measurements indicate the sensitivity

of the coherence of the exciton-exciton correlations to scattering processes.

This research demonstrates the power of ultrafast spectroscopy to explore interesting questions in many-body physics and opens up some interesting avenues of exploration some of which we mention below. This work has focused on the configuration where bound biexcitons do not play an important role. One question we are currently exploring is whether bound biexcitons can be seen in four-wave mixing. The bound biexciton has never been seen in bulk GaAs and it is interesting to ask if it can be detected in high magnetic fields where the unbound biexcitons are strongly correlated.

An important issue that our results have raised is the magnetic field enhancement of the exciton-exciton correlations. The explanation that quadrupole-quadrupole interactions between the excitons at high magnetic field are responsible for the enhanced correlations is plausible and intuitively appealing, but awaits a conclusive demonstration either theoretically or experimentally. Our data shows a strong temperature dependence of the exciton-exciton correlation at surprisingly low temperatures. Caculations of the dephasing due to acoustic and LO phonons correctly predict that the coherence of the exciton-exciton correlations is more sensitive to phonon scattering than the exciton coherence, but predict an effect which is two orders of magnitude smaller than that seen experimentally. The effect of temperature awaits a conclusive explanation.

There are some additional features in the measurements that also have not yet been explained. The exact shape of the time-integrated four-wave mixing measurements is not in perfect agreement with the theory. In particular, the theory predicts stronger oscillations for negative time delay. And the spectrally resolved signals show some structure around the hh-X which we believe is due to quantized center of mass motion of the excitons. The

role of the center of mass motion of the excitons in the nonlinear optical response is itself an interesting question.

Another interesting question which we have not addressed is whether more excitons than just two are correlated. The enhancement of the exciton-exciton correlations at high magnetic field suggests that further correlations are enhanced as well. Signatures of higher-order correlations could be looked for in the four-wave mixing signal, and higher-wave mixing experiments should provide clear signatures for higher-order correlations as indicated by the Dynamics Controlled Truncation Scheme.

Other experimental techniques could also contribute to exploring some questions raised here. The transition from 3-D to 1-D Boltzmann scattering which affects the exciton dephasing rate at high densities should also be evident in pump-probe measurements designed to study carrier relaxation. Spectrally resolved pump-probe measurements could also be used to look at the exciton resonances carefully to detect any energy shifts associated with quadrupole-quadrupole interactions between the excitons.

It is clear that there are many interesting questions still to be explored with ultrafast spectroscopy. We hope that this work has contributed to the field and will stimulate further research.

Bibliography

[1] L. Allen and J. H. Eberly, *Optical resonance and two-level atoms*, Dover, New York, 1987.

[2] A. Armitage, T. A. Fisher, M. S. Skolnick, D. M. Whittaker, and P. Kinsler, *Exciton polaritons in semiconductor quantum microcavities in a high magnetic field*, Phys. Rev. B **55**, 16395 (1997).

[3] N. W. Ashcroft and N. D. Mermin, *Solid state physics*, Saunders College Publishing, Orlando, 1976.

[4] V. M. Axt, *Dynamische dichtematrixtheorie kohärente erzeugter korrelationen an der halbleiterbandkante*, Ph.D. thesis, Rheinisch-Westfälischen Technischen Hochschule Aachen, 1994.

[5] V. M. Axt, G. Bartels, and A. Stahl, *Intraband dynamics at the semiconductor band edge: Shortcomings of the Bloch equation method*, Phys. Rev. Lett. **76**, 2543 (1996).

[6] V. M. Axt and A. Stahl, *A dynamics-controlled truncation scheme for the hierarchy of density matrices in semiconductor optics*, Z. Phys. B **93**, 195 (1994).

[7] V. M. Axt, A. Stahl, E. J. Mayer, P. H. Bolivar, S. Nüsse, K. Ploog, and K. Köhler,

Four-wave-mixing theory beyond the semiconductor Bloch equations, Phys. Stat. Sol. (b) **188**, 447 (1995).

[8] H. J. Bakker and H. Kurz, *Polariton effects in four-wave mixing*, Phys. Rev. B **50**, 7805 (1994).

[9] S. Bar-Ad, I. Bar-Joseph, G. Finkelstein, and Y. Levinson, *Biexcitons in short-pulse optical experiments in strong magnetic fields in GaAs quantum wells*, Phys. Rev. B **50**, 18375 (1994).

[10] S. Bar-Ad, P. Kner, M. V. Marquezini, D. S. Chemla, and K. El Sayed, *Carrier dynamics in the quantum kinetic regime*, Phys. Rev. Lett. **77**, 3177 (1996).

[11] S. Bar-Ad, P. Kner, M. V. Marquezini, S. Mukamel, and D. S. Chemla, *Quantum confined Fano interference*, Phys. Rev. Lett. **78**, 1363 (1997).

[12] G. Bartels, G. C. Cho, T. Dekorsy, H. Kurz, and A. Stahl, *Coherent signature of differential transmission signals in semiconductors: Theory and experiment*, Phys. Rev. B **55**, 16404 (1997).

[13] G. Bastard, *Wave mechanics applied to semiconductor heterostructures*, Halsted Press, New York, 1988.

[14] D. Bennhardt, P. Thomas, R. Eccleston, E. J. Mayer, and J. Kuhl, *Polarization dependence of four-wave-mixing signals in quantum wells*, Phys. Rev. B **47**, 13485 (1993).

[15] R. Binder and S. W. Koch, *Nonequilibrium semiconductor dynamics*, Prog. Quant. Electr. **19**, 307 (1995).

[16] K. Bott, O. Heller, D. Bennhardt, S. T. Cundiff, P. Thomas, E. J. Mayer, G. O. Smith, R. Eccleston, J. Kuhl, and K. Ploog, *Influence of exciton-exciton interactions on the coherent optical response in GaAs quantum wells*, Phys. Rev. B **48**, 17418 (1993).

[17] O. Carmel and I. Bar-Joseph, *Four-wave-mixing studies of quantum-well excitons in a magnetic field*, Phys. Rev. B **47**, 7606 (1993).

[18] D. S. Chemla, J.-Y. Bigot, M.-A. Mycek, and S. Weiss, *Ultrafast phase dynamics of coherent emission from excitons in GaAs quantum wells*, Phys. Rev. B **50**, 8439 (1994).

[19] S. T. Cundiff, M. Koch, W. H. Knox, and J. Shah, *Optical coherence in semiconductors: Strong emission mediated by nondegenerate interactions*, Phys. Rev. Lett. **77**, 1107 (1996).

[20] K. W. DeLong, D. N. Fittinghoff, and R. Trebino, *Practical issues in ultrashort-laser-pulse measurement using frequency-resolved optical gating*, IEEE Journal of Quantum Electronics **32**, 1253 (1996).

[21] R. J. Elliott and R. Loudon, *Theory of the absorption edge in semiconductors in a high magnetic field*, J. Phys. Chem. Solids **15**, 196 (1960).

[22] G. W. Fehrenbach, W. Schäfer, J. Treusch, and R. G. Ulbrich, *Transient optical spetra of a dense exciton gas in a direct-gap semiconductor*, Phys. Rev. Lett. **49**, 1281 (1982).

[23] D. N. Fittinghoff, J. L. Bowie, J. N. Sweetser, R. T. Jennings, M. A. Krumbügel, K. W. DeLong, and R. Trebino, *Measurement of the intensity and phase of ultraweak, ultrashort laser pulses*, Optics Letters **21**, 884 (1996).

[24] S. Glutsch, U. Siegner, and D. S. Chemla, *Spatiotemporal dynamics of photon echoes from continuum states in semiconductors*, Phys. Rev. B **52**, 4941 (1995).

[25] S. Glutsch, U. Siegner, M.-A. Mycek, and D. S. Chemla, *Fano resonances due to coupled magnetoexciton and continuum states in bulk semiconductors*, Phys. Rev. B **50**, 17009 (1994).

[26] H. Haug and S. W. Koch, *Quantum theory of the optical and electronic properties of semiconductors*, World Scientific, Singapore, 1993.

[27] H. Haug and S. Schmitt-Rink, *Electron theory of the optical properties of laser-excited semiconductors*, Prog. Quant. Electr. **9**, 3 (1984).

[28] J. J. Hopfield and D. G. Thomas, *Photon momentum effects in the magneto-optics of excitons*, Phys. Rev. Lett. **4**, 357 (1960).

[29] Y. Z. Hu, R. Binder, S. W. Koch, S. T. Cundiff, H. Wang, and D. G. Steel, *Excitation and polarization effects in semiconductor four-wave-mixing spectroscopy*, Phys. Rev. B **49**, 14382 (1994).

[30] W. Huhn and A. Stahl, *Self-consistent field theory applied to the semiconductor band edge*, Phys. Stat. Sol. (b) **124**, 167 (1984).

[31] F. Jahnke, M. Koch, T. Meier, J. Feldmann, W. Schäfer, P. Thomas, S. W. Koch, E. O. Göbel, and H. Nickel, *Simultaneous influence of disorder and Coulomb interaction on photon echoes in semiconductors*, Phys. Rev. B **50**, 8114 (1994).

[32] M. Jiang, H. Wang, R. Merlin, D. G. Steel, and M. Cardona, *Nonlinear optical spectroscopy in GaAs: Magnetic freezeout of excitons*, Phys. Rev. B **48**, 15476 (1993).

[33] L. V. Keldysh, *Proceedings of the 19th international conference on physics of semiconductors*, p. 1303, Moscow, 1968.

[34] D.-S. Kim, J. Shah, T. C. Damen, W. Schäfer, F. Jahnke, S. Schmitt-Rink, and K. Köhler, *Unusually slow temporal evolution of femtosecond four-wave-mixing signals in intrinsic GaAs quantum wells: Direct evidence for the dominance of interaction effects*, Phys. Rev. Lett. **69**, 2725 (1992).

[35] O: Kinrot and Y. Prior, *Four-wave mixing in optically dense media*, Phys. Rev. A **50**, R1999 (1994).

[36] P. Kner, S. Bar-Ad, M. V. Marquezini, D. S. Chemla, and W. Schäfer, *Exciton-exciton correlations in high magnetic fields*, Phys. Stat. Sol. (a) **164**, 579 (1997).

[37] P. Kner, S. Bar-Ad, M. V. Marquezini, D. S. Chemla, and W. Schäfer, *Magnetically enhanced exciton-exciton correlations in semiconductors*, Phys. Rev. Lett. **78**, 1319 (1997).

[38] P. Kner, S. Bar-Ad, M. V. Marquezini, S. Mukamel, and D. S. Chemla, *Quantum confined Fano interference*, Phys. Stat. Sol. (a) **164**, 319 (1997).

[39] W. H. Knox, D. S. Chemla, G. Livescu, J. E. Cunningham, and J. E. Henry, *Femtosecond carrier thermalization in dense fermi seas*, Phys. Rev. Lett. **61**, 1290 (1988).

[40] M. Koch, J. Feldmann, G. von Plessen, and E. O. Göbel, *Quantum beats versus polarization interference: an experimental distinction*, Phys. Rev. Lett. **69**, 3631 (1992).

[41] A. V. Korolev and M. A. Liberman, *Term splitting and binding energy of the hydrogen molecule in an ultrahigh magnetic field*, Sov. Phys. JETP **73**, 223 (1991).

[42] A. V. Korolev and M. A. Liberman, *Binding energy and triplet-singlet splitting for the hydrogen molecule in untrahigh magnetic fields*, Phys. Rev. A **45**, 1762 (1992).

[43] Yu. P. Kravchenko and M. A. Liberman, *Hydrogen molecule in a strong parallel magnetic field*, Phys. Rev. A **57**, 3403 (1998).

[44] Yu. P. Kravchenko, M. A. Liberman, and B. Johansson, *Exact solution for a hydrogen atom in a magnetic field of arbitrary strength*, Phys. Rev. A **54**, 287 (1996).

[45] K. Leo, M. Wegener, J. Shah, D. S. Chemla, E. O. Göbel, T. C. Damen, S. Schmitt-Rink, and W. Schäfer, *Effects of coherent polarization interactions on time-resolved degenerate four-wave mixing*, Phys. Rev. Lett. **65**, 1340 (1990).

[46] L. Lepetit, G. Cheriaux, and M. Joffre, *Linear techniques of phase measurement by femtosecond spectral interferometry for applications in spectroscopy*, J. Opt. Soc. Am. B **12**, 2467 (1995).

[47] J. J. LePore, *An improved technique for selective etching of GaAs and* $Ga_{1-x}Al_xAs$, J. Appl. Phys. **51**, 6441 (1981).

[48] M. Lindberg, R. Binder, and S. W. Koch, *Theory of the semiconductor photon echo*, Phys. Rev. A **45**, 1865 (1992).

[49] M. Lindberg and S. W. Koch, *Effective Bloch equations for semiconductors*, Phys. Rev. B **38**, 3342 (1988).

[50] R. Lövenich, W. Schäfer, P. Kner, and D. S. Chemla, *Theory of coherently driven biexcitons in strong magnetic fields*, Phys. Stat. Sol. (a) **164**, 347 (1997).

[51] V. G. Lyssenko, J. Erland, I. Balslev, K.-H. Pantke, B.S. Raxbirin, and J. M. Hvam, *Nature of nonlinear four-wave-mixing beats in semiconductors*, Phys. Rev. B **48**, 5720 (1993).

[52] M. Z. Maialle and L. J. Sham, *Interacting electron theory of coherent nonlinear response*, Phys. Rev. Lett. **73**, 3310 (1994).

[53] M. V. Marquezini, P. Kner, S. Bar-Ad, J. Tignon, and D. S. Chemla, *Density dependence of the spectral dielectric function across a Fano resonance*, Phys. Rev. B **57**, 3745 (1998).

[54] E. J. Mayer, G. O. Smith, V. Heuckeroth, J. Kuhl, K. Bott, A. Schulze, T. Meier, S. W. Koch, P. Thomas, R. Hey, and K. Ploog, *Polarization dependence of beating phenomena at the energetically lowest exciton transition in GaAs quantum wells*, Phys. Rev. B **51**, 10909 (1995).

[55] T. Meier, A. Schulze, P. Thomas, and H. Vaupel, *Signatures of Fano resonances in four-wave-mixing experiments*, Phys. Rev. B **51**, 13977 (1995).

[56] S. Mukamel, *Principles of nonlinear optical spectroscopy*, Oxford University Press, New York, 1995.

[57] U. Neukirch, K. Wundke, J. Gutowski, and D. Hommel, *Propagation of femtosecond pulses in thin ZnSe layers*, Phys. Stat. Sol. (b) **196**, 473 (1996).

[58] F. H. Pollak and M. Cardona, *Piezo-electroreflectance in Ge, GaAs, and Si*, Phys. Rev. **172**, 816 (1968).

[59] T. Rappen, G. Mohs, and M. Wegener, *Dephasing of three- and two-dimensional magnetoexcitons in $In_xGa_{1-x}As$*, Appl. Phys. Lett. **63**, 1222 (1993).

[60] V. V. Rossin, P. C. M. Christianen, and V. V. Travnikov, *Effect of hot electrons on the magnetic field enhancement of exciton luminescence in GaAs*, Sol. St. Comm. **87**, 623 (1993).

[61] W. Schäfer, *Optics of semiconductor nanostructures*, p. 21, Akademie-Verlag, Berlin, 1993.

[62] W. Schäfer, to be published, 1998.

[63] W. Schäfer, private communication, September 1998.

[64] W. Schäfer, D. S. Kim, J. Shah, T. C. Damen, J. E. Cunningham, K. W. Goossen, L. N. Pfeiffer, and K. Köler, *Femtosecond coherent fields induced by many-particle correlations in transient four-wave mixing*, Phys. Rev. B **53**, 16429 (1996).

[65] S. Schmitt-Rink and D. S. Chemla, *Collective excitations and the dynamical stark effect in a coherently driven exciton system*, Phys. Rev. Lett. **57**, 2752 (1986).

[66] S. Schmitt-Rink, D. S. Chemla, and H. Haug, *Nonequilibrium theory of the optical stark effect and spectral hole burning in semiconductors*, Phys. Rev. B **37**, 941 (1988).

[67] J. R. Schrieffer, *Theory of superconductivity*, The Benjamin/Cummings Publishing Company, Inc., Reading, Massachusetts, 1964.

[68] L. Schultheis, J. Kuhl, A. Honold, and C. W. Tu, *Picosecond phase coherence and orientational relaxation of excitons in GaAs*, Phys. Rev. Lett. **57**, 1797 (1986).

[69] L. Schultheis, J. Kuhl, A. Honold, and C. W. Tu, *Ultrafast phase relaxation of excitons via exciton-exciton and exciton-electron collisions*, Phys. Rev. Lett. **57**, 1635 (1986).

[70] A. Schulze, A. Knorr, and S. W. Koch, *Pulse propagation and many-body effects in semiconductor four-wave mixing*, Phys. Rev. B **51**, 10601 (1995).

[71] U. Siegner, M.-A. Mycek, S. Glutsch, and D. S. Chemla, *Quantum interference in the system of Lorentzian and Fano magnetoexciton resonances in GaAs*, Phys. Rev. B **51**, 4953 (1995).

[72] U. Siegner, M.-A. Mycek, S. Glutsch, and D. S. Chemla, *Ultrafast coherent dynamics of Fano resonances in semiconductors*, Phys. Rev. Lett. **74**, 470 (1995).

[73] C. Stafford, S. Schmitt-Rink, and W. Schaefer, *Nonlinear optical response of two-dimensional magnetoexcitons*, Phys. Rev. B **41**, 10000 (1990).

[74] J. B. Stark, W. H. Knox, and D. S. Chemla, *Femtosecond dynamics of excitons under extreme magnetic confinement*, Phys. Rev. Lett. **65**, 3033 (1990).

[75] R. Trebino and D. J. Kane, *Using phase retrieval to measure the intensity and phase of ultrashort pulses: frequency-resolved optical gating*, J. Opt. Soc. Am. A **10**, 1101 (1993).

[76] A. Tredicucci, Y. Chen, F. Bassani, J. Massies, C. Deparis, and G. Neu, *Center-of-mass quantization of excitons and polariton interferences in GaAs thin layers*, Phys. Rev. B **47**, 10348 (1993).

[77] K. Victor, *Vielteilchendynamik optisch angeregter halbleiter*, Ph.D. thesis, Rheinisch-Westfälischen Technischen Hochschule Aachen, 1996.

[78] K. Victor, V. M. Axt, and A. Stahl, *Hierarchy of density matrices in coherent semicondcutor optics*, Phys. Rev. B **51**, 14164 (1995).

[79] H. Wang, K. Ferrio, and D. G. Steel, *Transient nonlinear optical response from excitation induced dephasing in GaAs*, Phys. Rev. Lett. **71**, 1261 (1993).

[80] H. Wang, K. B. Ferrio, and D. G. Steel, *Transient four-wave mixing line shapes: Effects of excitation-induced dephasing*, Phys. Rev. A **49**, R1551 (1994).

[81] M. Wegener, D. S. Chemla, S. Schmitt-Rink, and W. Schäfer, *Line shape of time-resolved four-wave mixing*, Phys. Rev. A **42**, 5675 (1990).

[82] M. U. Wehner, J. Hetzler, and M. Wegener, *Interferometric four-wave-mixing spectroscopy on bulk GaAs*, Phys. Rev. B **55**, 4031 (1997).

[83] S. Weiss, M.-A. Mycek, J.-Y. Bigot, S. Schmitt-Rink, and D. S. Chemla, *Collective effects in excitonic free induction decay: do semiconductors and atoms emit coherent light in different ways?*, Phys. Rev. Lett. **69**, 2685 (1992).

Appendix A

A new formulation of the theory

As this work was being finished, we were preparing a long paper with a formulation of the theory different from that presented in chapter 6. The theory is due to Reinhold Lövenich and Wilfried Schäfer. Here we present this formulation of the theory with a minimal amount of commentary.

Our starting point is the Hamiltonian of electrons and holes in the lowest Landau-level, coupled by the dipole-matrix element $\boldsymbol{\mu}_{\mathbf{k}}^{eh}$ to the external laser fields $\mathbf{E}$.

$$
\begin{aligned}
H = & \sum_{\mathbf{k}e} \varepsilon_{\mathbf{k}}^{e}\, \hat{e}_{\mathbf{k}}^{\dagger} \hat{e}_{\mathbf{k}} + \sum_{\mathbf{k}h} \varepsilon_{\mathbf{k}}^{h}\, \hat{h}_{\mathbf{k}}^{\dagger} \hat{h}_{\mathbf{k}} \\
+ & \sum_{\mathbf{k}eh} \left(\boldsymbol{\mu}_{\mathbf{k}}^{eh}\, \mathbf{E}\, \hat{e}_{\mathbf{k}}^{\dagger} \hat{h}_{\mathbf{k}}^{\dagger} + \boldsymbol{\mu}_{\mathbf{k}}^{he}\, \mathbf{E}\, \hat{h}_{\mathbf{k}} \hat{e}_{\mathbf{k}} \right) \\
+ & \frac{1}{2} \sum_{\mathbf{k}\mathbf{k}'\mathbf{q}} \Bigg\{ v_{\mathbf{q}}^{k_y - k'_y + q_y} \Big[\sum_{ee'} \hat{e}_{\mathbf{k}+\mathbf{q}}^{\dagger} \hat{e}_{\mathbf{k}'-\mathbf{q}}^{\dagger} \hat{e}_{\mathbf{k}'} \hat{e}_{\mathbf{k}} \\
+ & \sum_{hh'} \hat{h}_{\mathbf{k}+\mathbf{q}}^{\dagger} \hat{h}_{\mathbf{k}'-\mathbf{q}}^{\dagger} \hat{h}_{\mathbf{k}'} \hat{h}_{\mathbf{k}} \Big] \\
- & v_{\mathbf{q}}^{k_y - k'_y} \sum_{eh} \left[\hat{e}_{\mathbf{k}+\mathbf{q}}^{\dagger} \hat{h}_{\mathbf{k}'-\mathbf{q}}^{\dagger} \hat{h}_{\mathbf{k}'} \hat{e}_{\mathbf{k}} + \hat{h}_{\mathbf{k}+\mathbf{q}}^{\dagger} \hat{e}_{\mathbf{k}'-\mathbf{q}}^{\dagger} \hat{e}_{\mathbf{k}'} \hat{h}_{\mathbf{k}} \right] \Bigg\}
\end{aligned}
\tag{A.1}
$$

The single particle energies are given by

$$\varepsilon_{\mathbf{k}}^{e,h} = \varepsilon_0^{e,h} + \frac{\hbar^2}{2m_{e,h}l^2} + \frac{\hbar^2 k_z^2}{2m_{e,h}} \tag{A.2}$$

where l is the magnetic length, $l = \sqrt{\hbar/eB}$ and k_z is the momentum along the direction $\parallel \vec{B}$. For electrons and holes in the lowest Landau level, the Coulomb interaction in the Landau-gauge is given by

$$v_{\mathbf{q}}^{k_y} = \frac{e^2}{2\pi\varepsilon_0 L^2}\int_{-\infty}^{\infty} \mathrm{d}q_x \, \frac{e^{-l^2(q_x^2+q_y^2)/2}}{q_x^2+\mathbf{q}^2}\, \mathrm{e}^{il^2 k_y q_x}\,, \tag{A.3}$$

and $\hat{e}_{\mathbf{k}}^\dagger$, $\hat{h}_{\mathbf{k}}^\dagger$ are the Fermi operators for electrons and holes, with two-dimensionl $\mathbf{k}$-vectors in the k_y-k_z-plane. The optical properties are determined by the polarization $\vec{P} = \sum_{ehk} \vec{\mu}_{eh} P_k^{eh}$, where $P_{\mathbf{k}}^{eh} = \langle \hat{e}_{\mathbf{k}}^\dagger \hat{h}_{-\mathbf{k}}^\dagger \rangle$, is the transition amplitude between an electron in band e and a hole in band h with respective wavevectors k and $-k$. $P_{\mathbf{k}}^{eh}$ obeys the equation

$$\begin{aligned} &\left(-i\hbar\frac{\partial}{\partial t} - \varepsilon_{\mathbf{k}}^e - \varepsilon_{\mathbf{k}}^h - i\hbar\gamma_P\right) P_{\mathbf{k}}^{eh} + \sum_{\mathbf{q}} v_{\mathbf{q}}^0 P_{\mathbf{k}+\mathbf{q}}^{eh} \\ &= \sum_{h'} \boldsymbol{\mu}_{\mathbf{k}}^{h'e}\mathbf{E}\left(\delta_{h,h'} - f_{\mathbf{k}}^{hh'}\right) - \sum_{e'} \boldsymbol{\mu}_{\mathbf{k}}^{he'}\mathbf{E}\, f_{\mathbf{k}}^{e'} + \frac{\partial}{\partial t} P_{\mathbf{k}}^{eh}\Big|_{int} \end{aligned} \tag{A.4}$$

where the interaction contribution is given by

$$\begin{aligned} \frac{\partial}{\partial t} P_{\mathbf{k}}^{eh}\Big|_{int} &= \sum_{\mathbf{k}'\mathbf{q}} v_{\mathbf{q}}^{k_y - k_y'} \Bigg\{ \sum_{e'} \Big[\langle \hat{e}_{\mathbf{k}+\mathbf{q}}^\dagger \hat{h}_{-\mathbf{k}}^\dagger \hat{e}_{\mathbf{k}'}^\dagger \hat{e}_{\mathbf{k}'+\mathbf{q}} \rangle \\ &- \langle \hat{e}_{\mathbf{k}}^\dagger \hat{h}_{-\mathbf{k}-\mathbf{q}}^\dagger \hat{e}_{\mathbf{k}'+\mathbf{q}}^\dagger \hat{e}_{\mathbf{k}'} \rangle \Big] + \sum_{h'} \Big[\langle \hat{e}_{\mathbf{k}}^\dagger \hat{h}_{-\mathbf{k}-\mathbf{q}}^\dagger \hat{h}_{-\mathbf{k}'}^\dagger \hat{h}_{-\mathbf{k}'-\mathbf{q}} \rangle \\ &- \langle \hat{e}_{\mathbf{k}+\mathbf{q}}^\dagger \hat{h}_{-\mathbf{k}}^\dagger \hat{h}_{-\mathbf{k}'-\mathbf{q}}^\dagger \hat{h}_{-\mathbf{k}'} \rangle \Big] \Bigg\} \end{aligned} \tag{A.5}$$

Within the $\chi^{(3)}$-truncation scheme we make use of particle-number conservation, which allows the introduction, in Eq. (A.5), of 6-point instead of 4-point correlation functions according to the relation,

$$\langle \hat{e}_{\mathbf{k}_1}^\dagger \hat{h}_{\mathbf{k}_2}^\dagger \hat{e}_{\mathbf{k}_3} \hat{e}_{\mathbf{k}_4} \rangle = \sum_{\mathbf{k},h'} \langle \hat{e}_{\mathbf{k}_1}^\dagger \hat{h}_{\mathbf{k}_2}^\dagger \hat{e}_{\mathbf{k}_3} \hat{h'}_{\mathbf{k}}^\dagger \hat{h'}_{\mathbf{k}} \hat{e}_{\mathbf{k}_4} \rangle$$

$$- \sum_{\mathbf{k},e'} \langle \hat{e}^\dagger_{\mathbf{k}_1} \hat{h}^\dagger_{\mathbf{k}_2} \hat{e}_{\mathbf{k}_3} \hat{e'}^\dagger_{\mathbf{k}} \hat{e'}_{\mathbf{k}} \hat{e}_{\mathbf{k}_4} \rangle \,. \tag{A.6}$$

The second contribution on the right hand side is at least of 5th order in the excitation field and neglected at the $\chi^{(3)}$-level. The resulting 6-point functions are factorized into all possible products of 2-point and 4-point functions. This procedure allows us to split the interaction contribution, Eq. (A.5) into the Hartree-Fock contribution and a correlation contribution. The Hartree-Fock contribution is,

$$\begin{aligned} \frac{\partial}{\partial t} P^{eh}_{\mathbf{k}} \bigg|_{HF} &= \sum_{\mathbf{q},e'h'} v^0_{\mathbf{k}-\mathbf{q}} \Big[P^{eh'}_{\mathbf{q}} f^{h'h}_{\mathbf{k}} \, \delta_{e,e'} + P^{e'h}_{\mathbf{q}} f^{ee'}_{\mathbf{k}} \, \delta_{h,h'} \\ &- P^{e'h}_{\mathbf{k}} f^{ee'}_{\mathbf{q}} \, \delta_{h,h'} - P^{eh'}_{\mathbf{k}} f^{h'h}_{\mathbf{q}} \, \delta_{e,e'} \Big] \,. \end{aligned} \tag{A.7}$$

The one-particle distribution function is the sum of a coherent and an incoherent contribution

$$f^{ee'}_{\mathbf{k}} = \sum_{h'} P^{eh'}_{\mathbf{k}} P^{eh'*}_{\mathbf{k}} + \sum_{\mathbf{q},h'} N^{eh'e'h'}_{\mathbf{k},\mathbf{q},\mathbf{k},\mathbf{q}} \tag{A.8}$$

where we introduce the pair-density correlation function

$$N^{ehe'h'}_{\mathbf{k}_1,\mathbf{k}_2,\mathbf{k}_3,\mathbf{k}_4} = \langle \hat{e}^\dagger_{\mathbf{k}_1} \hat{h}^\dagger_{\mathbf{k}_2} \hat{e}'_{\mathbf{k}_3} \hat{h}'_{\mathbf{k}_4} \rangle - \langle \hat{e}^\dagger_{\mathbf{k}_1} \hat{h}^\dagger_{\mathbf{k}_2} \rangle \langle \hat{e}'_{\mathbf{k}_3} \hat{h}'_{\mathbf{k}_4} \rangle \tag{A.9}$$

which determines the incoherent part of the one-particle distribution function. The correlation contribution to Eq. (A.5) consists of two parts. One is incoherent and determined by the pair-density correlation function $N^{ehe'h'}_{\mathbf{k}_1,\mathbf{k}_2,\mathbf{k}_3,\mathbf{k}_4}$, and the second one is due to the biexcitonic correlation function

$$\begin{aligned} B^{ehe'h'}_{\mathbf{k}_1,\mathbf{k}_2,\mathbf{k}_3,\mathbf{k}_4} &= \langle \hat{e}^\dagger_{\mathbf{k}_1} \hat{h}^\dagger_{\mathbf{k}_2} \hat{e}'^\dagger_{\mathbf{k}_3} \hat{h}'^\dagger_{\mathbf{k}_4} \rangle \\ &- \langle \hat{e}^\dagger_{\mathbf{k}_1} \hat{h}^\dagger_{\mathbf{k}_2} \rangle \langle \hat{e}'^\dagger_{\mathbf{k}_3} \hat{h}'^\dagger_{\mathbf{k}_4} \rangle + \langle \hat{e}^\dagger_{\mathbf{k}_1} \hat{h}'^\dagger_{\mathbf{k}_4} \rangle \langle \hat{e}'^\dagger_{\mathbf{k}_3} \hat{h}^\dagger_{\mathbf{k}_2} \rangle \,. \end{aligned} \tag{A.10}$$

When all these elements are collected, the correlation contribution to Eq. (A.5) takes the

form,

$$
\begin{aligned}
\frac{\partial}{\partial t} P^{eh}_{\mathbf{k}}\Big|_{corr} &= \sum_{\mathbf{k}'\mathbf{q},e'h'} v_{\mathbf{q}}^{k_y-k'_y} \Big\{ \Big[P^{e'h'*}_{\mathbf{k}'} - P^{e'h'*}_{\mathbf{k}'+\mathbf{q}} \Big] \\
\times & \Big[B^{ehe'h'}_{\mathbf{k}+\mathbf{q},\mathbf{k},\mathbf{k}'+\mathbf{q},\mathbf{k}'} + B^{ehe'h'}_{\mathbf{k},\mathbf{k}+\mathbf{q},\mathbf{k}',\mathbf{k}'+\mathbf{q}} \Big] \\
+ & P^{e'h}_{\mathbf{k}} N^{e'h'eh'}_{\mathbf{k},\mathbf{k}',\mathbf{k}+\mathbf{q},\mathbf{k}'+\mathbf{q}} - P^{e'h}_{\mathbf{k}+\mathbf{q}} N^{e'h'eh'}_{\mathbf{k}+\mathbf{q},\mathbf{k}'+\mathbf{q},\mathbf{k},\mathbf{k}'} \\
+ & P^{eh'}_{\mathbf{k}} N^{e'h'e'h}_{\mathbf{k}'+\mathbf{q},\mathbf{k},\mathbf{k}',\mathbf{k}+\mathbf{q}} - P^{eh'}_{\mathbf{k}+\mathbf{q}} N^{e'h'e'h}_{\mathbf{k}'+\mathbf{q},\mathbf{k}+\mathbf{q},\mathbf{k}',\mathbf{k}} \\
+ & \Big[P^{e'h'}_{\mathbf{k}'} - P^{e'h'}_{\mathbf{k}'+\mathbf{q}} \Big] \Big[N^{ehe'h'}_{\mathbf{k}'+\mathbf{q},\mathbf{k}',\mathbf{k}+\mathbf{q},\mathbf{k}} + N^{ehe'h'}_{\mathbf{k}',\mathbf{k}'+\mathbf{q},\mathbf{k},\mathbf{k}+\mathbf{q}} \Big] \Big\} .
\end{aligned}
\tag{A.11}
$$

The equation of motion of the pair-density correlation function has the form,

$$
\begin{aligned}
& \Big(-i\hbar \frac{\partial}{\partial t} - \varepsilon^{e}_{\mathbf{k}_1} - \varepsilon^{h}_{\mathbf{k}_2} + \varepsilon^{e'}_{\mathbf{k}_3} + \varepsilon^{h'}_{\mathbf{k}_4} \Big) N^{ehe'h'}_{\mathbf{k}_1,\mathbf{k}_2,\mathbf{k}_3,\mathbf{k}_4} \\
- & \sum_{\mathbf{q}} v^{0}_{\mathbf{q}} \Big(N^{ehe'h'}_{\mathbf{k}_1+\mathbf{q},\mathbf{k}_2+\mathbf{q},\mathbf{k}_3,\mathbf{k}_4} - N^{ehe'h'}_{\mathbf{k}_1,\mathbf{k}_2,\mathbf{k}_3+\mathbf{q},\mathbf{k}_4+\mathbf{q}} \Big) \\
= & \frac{\partial}{\partial t} N^{ehe'h'}_{\mathbf{k}_1,\mathbf{k}_2,\mathbf{k}_3,\mathbf{k}_4}\Big|_{\text{source}} + \frac{\partial}{\partial t} N^{ehe'h'}_{\mathbf{k}_1,\mathbf{k}_2,\mathbf{k}_3,\mathbf{k}_4}\Big|_{\text{scatt}} .
\end{aligned}
\tag{A.12}
$$

In its simplest version the source term is proportional to $\gamma_P \, P^{eh*}_{\mathbf{k}_1} P^{e'h'}_{\mathbf{k}_3} \, \delta_{\mathbf{k}_1,\mathbf{k}_2} \, \delta_{\mathbf{k}_3,\mathbf{k}_4}$, i. e. the decay of the coherent polarization. The scattering contribution drives the pair-density correlation function towards its quasi-equilibrium value. In principle a $\chi^{(3)}$-truncation theory cannot account for these processes. Since this is an incoherent contribution to the dynamics, the CCTS is not well suited anyway, and one should refer to other methods of manyparticle theory.

The equation of motion of the biexciton correlation function is

$$
\begin{aligned}
\Big(-i\hbar \frac{\partial}{\partial t} & - \varepsilon^{e}_{\mathbf{k}+\mathbf{q}} - \varepsilon^{h'}_{\mathbf{k}'+\mathbf{q}} - \varepsilon^{e'}_{\mathbf{k}'} - \varepsilon^{h}_{\mathbf{k}} - i\gamma_B \Big) B^{ehe'h'}_{\mathbf{k}+\mathbf{q},\mathbf{k}'+\mathbf{q},\mathbf{k}',\mathbf{k}} \\
- \sum_{\mathbf{q}'} & \Big[\; v_{\mathbf{q}'}^{k_y-k'_y+q'_y-q_y} B^{ehe'h'}_{\mathbf{k}+\mathbf{q}+\mathbf{q}',\mathbf{k}'+\mathbf{q},\mathbf{k}'-\mathbf{q}',\mathbf{k}} \\
& + \; v_{\mathbf{q}'}^{k'_y-k_y+q'_y-q_y} B^{ehe'h'}_{\mathbf{k}+\mathbf{q},\mathbf{k}'+\mathbf{q}+\mathbf{q}',\mathbf{k}',\mathbf{k}-\mathbf{q}'}
\end{aligned}
$$

$$
\begin{aligned}
&- \; v_{\mathbf{q}'}^{k_y-k_y'} B^{ehe'h'}_{\mathbf{k+q+q'},\mathbf{k'+q+q'},\mathbf{k'},\mathbf{k}} \\
&- \; v_{\mathbf{q}'}^{k_y'-k_y} B^{ehe'h'}_{\mathbf{k+q},\mathbf{k'+q},\mathbf{k'+q'},\mathbf{k+q'}} \\
&- \; v_{\mathbf{q}'}^{q_y} B^{ehe'h'}_{\mathbf{k+q+q'},\mathbf{k'+q},\mathbf{k'},\mathbf{k+q'}} \\
&- \; v_{\mathbf{q}'}^{-q_y} B^{ehe'h'}_{\mathbf{k+q},\mathbf{k'+q+q'},\mathbf{k'+q'},\mathbf{k}}\Big] \qquad \text{(A.13)} \\
&= \; -v_{\mathbf{q}}^{k_y-k_y'}(P^{eh}_{\mathbf{k}} - P^{eh}_{\mathbf{k+q}})(P^{e'h'}_{\mathbf{k'+q}} - P^{e'h'}_{\mathbf{k'}}) \\
&+ \; v_{\mathbf{k-k'}}^{q_y}(P^{eh'}_{\mathbf{k'+q}} - P^{eh'}_{\mathbf{k+q}})(P^{e'h}_{\mathbf{k}} - P^{e'h}_{\mathbf{k'}}) + \mathcal{O}(E^6)\,.
\end{aligned}
$$

At low excitation intensities and for times small compared to the dephasing times, the coherent limit captures the essential physics of the nonlinear emission. In this case the pair-density correlation function, $N^{ehe'h'}_{\mathbf{k_1},\mathbf{k_2},\mathbf{k_3},\mathbf{k_4}}$, vanishes and only the biexcitonic correlation function contributes. This function fulfills the fundamental anticommutation relations of Fermi particles, which are taken into account in an expansion of the form

$$
\begin{aligned}
B^{ehe'h'}_{\mathbf{k+q},\mathbf{k},\mathbf{k'},\mathbf{k'+q}} = \sum_{nm} \Big[& \\
& B^{ehe'h'}_{nm}(\mathbf{q})\, \varphi^{eh}_n(\mathbf{k}+\hat{\beta}\mathbf{q}, q_y)\; \varphi^{e'h'}_m(\mathbf{k'}+\hat{\alpha}\mathbf{q}, -q_y) \\
\pm \; & B^{eh'e'h}_{nm}(\mathbf{k}-\mathbf{k'})\, \varphi^{eh'}_n(\hat{\beta}\mathbf{k}+\hat{\alpha}\mathbf{k'}+\mathbf{q}, k_y-k_y') \\
& \times \varphi^{e'h}_m(\hat{\beta}\mathbf{k'}+\hat{\alpha}\mathbf{k}, k_y'-k_y)\Big]\,, \qquad \text{(A.14)}
\end{aligned}
$$

where we assume the most general case of anisotropic masses in the y and z directions. In that case $\hat{\alpha}$ and $\hat{\beta}$ are diagonal matrices with $\alpha_{ii} = m_{ei}/M_i$, $\beta_{ii} = m_{hi}/M_i$ and $M_i = m_{ei} + m_{hi}$. Finally we take the physical limit $m_{ey} = m_{hy} \to \infty$. The expansion in terms of these eigenfunctions is performed in two steps. In the first step after insertion of Eq. (A.14) in Eq. (A.13), we multiply by the phase factor $\exp[il^2 q_x(k_y - k_y')]$ which appears in Eq. (A.11) from the Coulomb potential in the Landau gauge, Eq. (A.3), and we perform

the k_y and k'_y summations. This allows us to express the wavefunctions in Eq. (A.14) in the form,

$$\varphi_n^{eh}(k+\alpha q,p) = \sum_{k_y} \exp[il^2 q_x(k_y+\alpha_{yy}q_y)]\,\varphi_n^{eh}(\mathbf{k}+\hat{\alpha}\mathbf{q},q_y) \tag{A.15}$$

which are solutions of

$$\begin{aligned}\frac{\hbar^2k^2}{2\mu^{eh}}\,\varphi_n^{eh}(k+\alpha q,p) \quad &- \quad \sum_{k'} V^{(1)}(p,k-k')\,\varphi_n^{eh}(k'+\alpha q,p)\\ &= \quad \varepsilon_n^{eh}(pq)\,\varphi_n^{eh}(k+\alpha q,p)\,,\end{aligned} \tag{A.16}$$

with

$$V^{(1)}(p,k-k') = \frac{e^2}{\varepsilon_0 L^3}\int_0^\infty dp'\,p'\,\frac{\exp(-\frac{1}{2}l^2p^2)}{p'^2+(k-k')^2}\,J_0(l^2pp')\,. \tag{A.17}$$

In the second step we project (A.13) onto the basis set of these eigenstates, this results in the following equation of motion for the polarization

$$\begin{aligned}&\Big(-i\hbar\frac{\partial}{\partial t}-\varepsilon_n^{eh}(0,0)\Big)P_n^{eh} = \boldsymbol{\mu}^{eh}\mathbf{E}\,\tilde{\varphi}_n^{eh}(0)\\ &- \sum_{ml}\sum_{e'h'}\Big[(\boldsymbol{\mu}^{e'h}\mathbf{E}\,b_{nml}^{eh'e'h'}+\boldsymbol{\mu}^{eh'}\mathbf{E}\,b_{nml}^{e'he'h'})P_m^{e'h}\;P_l^{e'h'*}\Big]\\ &+ \sum_{mn'm'}\sum_{e'h'}V_{nm,n'm'}^{st}\;P_m^{e'h'*}\;P_{n'}^{eh'}\;P_{m'}^{e'h}\\ &+ \sum_{mn'm'}\sum_{e'h'}\sum_{\mathbf{q}}P_m^{e'h'*}\Big[V_{nm,n'm'}^{c}(\mathbf{q})\,B_{n'm'}^{ehe'h'}(\mathbf{q})\\ &\quad\mp V_{nm,n'm'}^{xc}(\mathbf{q})\,B_{n'm'}^{eh'e'h}(\mathbf{q})\Big]\,,\end{aligned} \tag{A.18}$$

where $\mathbf{q}$ now labels the two dimensional vector $(q_{||},q_z)$. In Eq. (A.18) the b_{nml} are the Pauli blocking matrix elements, V^{st} is the static Coulomb interaction, V^c the RPA Coulomb interaction and V^{xc} is the corresponding exchange contribution. The definitions of the various matrix elements as well as those appearing Eq. (A.13) are summarized below. The final form of the equation of motion of the biexcitonic correlation function is

$$\Big(-i\hbar\frac{\partial}{\partial t}-\varepsilon_n^{eh}(\mathbf{q})-\varepsilon_m^{e'h'}(\mathbf{q})\Big)B_{nm}^{ehe'h'}(\mathbf{q})$$

$$
\begin{aligned}
&- \sum_{n'm'} \sum_{\mathbf{q}'} H_{nm,n'm'}(\mathbf{q},\mathbf{q}')\, B^{ehe'h'}_{n'm'}(\mathbf{q}') \\
&= -\sum_{\bar{n}\bar{m}\bar{\mathbf{q}}} \sum_{n'm'} \left(1-S\right)^{-1}_{nm\mathbf{q},\bar{n}\bar{m}\bar{\mathbf{q}}} \\
&\cdot \left\{ V^{c}_{n'm',\bar{n}\bar{m}}(\bar{\mathbf{q}}) P^{eh}_{n'} P^{e'h'}_{m'} - V^{xc}_{n'm',\bar{n}\bar{m}}(\bar{\mathbf{q}}) P^{eh'}_{n'} P^{eh'}_{m'} \right\}.
\end{aligned}
\tag{A.19}
$$

It is worth noting that the real-space representation of Eq. (A.19), written for infinite hole masses and with only the $1S$-exciton contributions retained, is nothing but the Heitler–London expansion.

Since the solution of Eq. (A.18) and Eq. (A.19) is very time consuming, up to now only partial solutions of the problem have been performed, usually in second order Born approximation. The energies depend only weakly on $q_{||}$. Therefore it is possible to simulate this dependency by a coarse grid, as long as the delay Δt is not too small. For Δt close to zero, interference effects in the continuum associated with $q_{||}$ become important, and, even in second order Born approximation, it is not trivial to achieve convergence with respect to $q_{||}$.

If contributions beyond this are taken into account, the TI-FWM is expected to increase S^{-}_{TI}, since S^{-}_{TI} originates from the 4-particle correlations. The interference of the different $q_{||}$ contributions also damps out the structure for $\Delta t < 0$. This means that the second order Born approximation is well justified; it only underestimates the contribution for $\Delta t < 0$.

These oscillations are smoothed out if the $q_{||}$ dependency is taken into account more carefully, as shown in Figure A.1. This should be even more pronounced, if contributions beyond second order Born approximation are accounted for. The coupling to the continuum

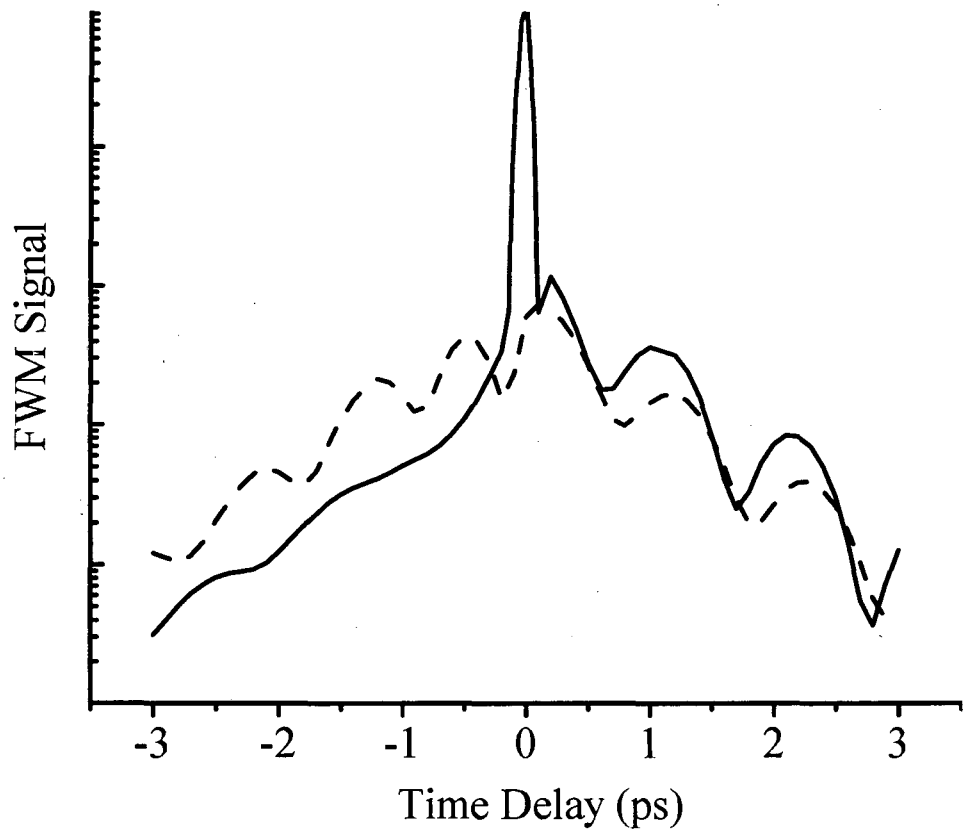

Figure A.1: TI-FWM for bulk GaAs in a high magnetic field calculated taking the $q_{||}$ dependence of the biexcitonic correlation function into account (solid line). The calculation without the $q_{||}$ dependence (dashed line) is shown for comparison. Including the $q_{||}$ dependence smooths the oscillations for $\Delta t < 0$ and reproduces the coherent peak.

associated with $q_{||}$ correctly reproduces the peak at $\Delta t = 0$ seen in the experimental data.

A.1 Matrix elements

For better readability we represent $\mathbf{q}$ as (p, q). The Pauli blocking matrix element is given by:

$$b_{nml}^{eh'e'h'} = \sum_k \varphi_n^{eh}(k,0)\, \varphi_m^{eh'}(k,0)\, \varphi_l^{e'h'}(k,0)\,. \tag{A.20}$$

The static Coulomb interaction in the equation of motion for the polarization reads as:

$$V^{st}_{nm,n'm'} = \sum_{k,q} V^{(1)}(0,k-q)\,\varphi^{eh'}_{n'}(k)\,\varphi^{e'h}_{m'}(q)$$
$$\times \quad (\varphi^{eh*}_{n}(k) - \varphi^{eh*}_{n}(q))(\varphi^{e'h'*}_{m}(q) - \varphi^{e'h'*}_{m}(k))\,. \tag{A.21}$$

The two other Coulomb matrix elements in the mentioned equation, the RPA like V^c and exchange type V^{xc} are defined as

$$V^{c}_{nm,n'm'}(q,p) = v^0(q,p)\,M^{eh}_{nn'}(q,p)\,M^{e'h'}_{mm'}(q,p)$$

$$\tag{A.22}$$

$$V^{xc}_{nm,n'm'}(q,p) = \sum_{kk'} v^0(q,p)\varphi^{eh*}_{n}(k+\alpha q,0)$$
$$\varphi^{e'h'*}_{m}(k+\beta q,0)(\varphi^{eh'}_{n'}(k) - \varphi^{eh'}_{n'}(k'))$$
$$\times \quad (\varphi^{eh'}_{m'}(k'+q) - \varphi^{eh'}_{m'}(k+q))\,, \tag{A.23}$$

where we made use of the Coulomb interaction

$$v^{p'}(q,p) = \frac{e^2}{2\pi\varepsilon_0 L^2}\,p\,\frac{\exp(\frac{1}{2}l^2p^2)}{p^2+q^2}\,J_0(l^2pp')\,, \tag{A.24}$$

and the overlap matrix elements

$$M^{eh}_{nn'}(q,p) \;=\; \sum_{k} \varphi^{eh*}_{n}(k,0)$$
$$\times \quad (\varphi^{eh}_{n'}(k+\alpha q,p) - \varphi^{eh}_{n'}(k-\beta q,p))\,. \tag{A.25}$$

The overlap matrix is defined by:

$$S_{nm\mathbf{q},n'm'\mathbf{q}'} = \sum_{kk'} \varphi^{eh*}_{n}(k+\alpha q,p)\,\varphi^{e'h'*}_{m}(k'+\beta q,p)$$
$$\varphi^{eh'}_{n'}(\beta k+\alpha k'+q',p')\,\varphi^{e'h}_{m'}(\beta k'+\alpha k,p')\,. \tag{A.26}$$

The interaction matrix H in eq. (A.19) is obtained by applying $(1-S)^{-1}$ to a matrix $\tilde{H}$:

$$\begin{aligned} H_{nm,n'm'}(\mathbf{q},\mathbf{q}') &= \sum_{\bar{n}\bar{m}}\sum_{\bar{\mathbf{q}}}(1-S)^{-1}_{nm,\bar{n}\bar{m}}(\mathbf{q},\bar{\mathbf{q}}) \\ &\times \tilde{H}_{\bar{n}\bar{m},n'm'}(\bar{\mathbf{q}},\mathbf{q}')\,. \end{aligned} \tag{A.27}$$

This is finally given by

$$\begin{aligned} \tilde{H}_{nm,n'm'}(\mathbf{q},\mathbf{q}') &= v^0(q-q',p-p') \\ &\times \Big[\bar{M}^{eh}_{nn'}(\beta(q-q'),p,p')\bar{M}^{eh}_{mm'}(\alpha(q-q'),p,p') \\ &+ \bar{M}^{eh}_{nn'}(\alpha(q-q'),p,p')\bar{M}^{eh}_{mm'}(\beta(q-q'),p,p')\Big] \\ &- v^{p'}(q-q',p-p') \\ &\times \Big[\bar{M}^{eh}_{nn'}(\beta(q-q'),p,p')\bar{M}^{eh}_{mm'}(\beta(q'-q),p,p') \\ &+ \bar{M}^{eh}_{nn'}(\alpha(q'-q),p,p')\bar{M}^{eh}_{mm'}(\alpha(q-q'),p,p')\Big]\,. \end{aligned} \tag{A.28}$$

where $\bar{M}$ is given by

$$\bar{M}^{eh}_{nn'}(q,p,p') = \sum_k \varphi^{eh}_n(k,p)\,\varphi^{eh}_{n'}(k+q,p') \tag{A.29}$$

Ernest Orlando Lawrence Berkeley National Laboratory
One Cyclotron Road | Berkeley, California 94720

Prepared for the U.S. Department of Energy under Contract No. DE-AC03-76SF00098